Master's thesis

NTNU
Norwegian University of Science and Technology
Faculty of Natural Sciences
Department of Materials Science and Engineering

Ivar Loland Råheim

Computational Materials Design of Materials for CO_2 Conversion using Sunlight

Master's thesis in Chemical Engineering and Biotechnology
Supervisor: Professor Sverre M. Selbach
Co-supervisor: Post doc. Dr. Benjamin A. D. Williamson
June 2021

NTNU
Norwegian University of
Science and Technology

Ivar Loland Råheim

Computational Materials Design of Materials for CO_2 Conversion using Sunlight

Master's thesis in Chemical Engineering and Biotechnology
Supervisor: Professor Sverre M. Selbach
Co-supervisor: Post doc. Dr. Benjamin A. D. Williamson
June 2021

Norwegian University of Science and Technology
Faculty of Natural Sciences
Department of Materials Science and Engineering

NTNU
Norwegian University of
Science and Technology

Preface

As a part of the course TMT4900 - Materials Chemistry and Energy Technology, Master's Thesis, this report covers the work and results accomplished by Ivar Loland Råheim from January to June 2021. Professor Sverre Magnus Selbach was supervisor for the project, while Ben Williamson was co-supervisor. The project was carried out at the Department of Materials Science and Engineering (IMA) at NTNU in Trondheim as a direct continuation of my own previous specialization project with the same name [1].

Acknowledgements

Before starting I would like to thank my supervisor Professor Sverre M. Selbach for guidance and helpful remarks during the project. A special thanks also goes out to my co-supervisor Post doc. Dr. Benjamin A. D. Williamson for always being available and always providing great and witty feedback. Additionally, I want to thank the Ferroics FACET group along with the department Simulations group for providing a platform in which to show and discuss interesting results and potential issues. Furthermore, I want to thank my friends Amalie, Håvard, Karen and May Helen for always providing food to the table, my friend Stine for quizzes and proofreading, and my always supportive family. Last but not least, I also have to thank my friend Kristoffer for teaching me everything I have learned for the past five years.

Abstract

A high-throughput computational materials search for a material suitable for photocatalytic CO_2-conversion has been completed through an ab-initio study using density functional theory (DFT). The materials that have been investigated includes computer-generated ternary tellurides on the form $ABTe_2$, with A=Li, Na, K, Rb and Cs, and B=Al, Ga and In, in different configurations. The project was carried out in a screening process where requirements important for good photocatalytic performance had to be met in order for the compounds to be further evaluated. The semi-local GGA functional PBEsol was used throughout the project for electronic structure and optical calculations, with included spin orbit coupling contributions. The project started out with 28 materials that already had been determined to be thermodynamically stable. Out of these, ten had sufficiently large band gaps and low effective masses to pass the screening criteria. All of these materials were then predicted to be dynamically stable through phonon dispersion calculations. Three of the compounds were later screened out due to low direct absorption of photons with energies close to the direct band gap value. This left us with the indirect absorbers $Pna2_1$ $LiGaTe_2$, $I\bar{4}2d$ $LiGaTe_2$ and $C2/c$ $CsGaTe_2$. The direct candidates that were left are: $Pna2_1$ $LiAlTe_2$, $Pna2_1$ $LiInTe_2$, $I\bar{4}2d$ $LiInTe_2$ and $C2/c$ $CsInTe_2$. The A cation was determined to mainly influence the lattice parameters, while the B cation had the largest impact on the electronic structure. The preferred system seems to be B cations in corner-sharing $[BTe_4]$-tetrahedra, where both good orbital overlap between B s states and Te p states lead to well dispersed bands without too narrow band gaps. This tetrahedral configuration is found in both the chalcopyritic $I\bar{4}2d$ space group and the orthorhombic $Pna2_1$.

Sammendrag

Et stor-skala materialsøk for en halvleder passende for fotokatalytisk CO_2-konvertering har blitt gjennomført gjennom et ab-initio beregningsstudie ved hjelp av tetthetsfunksjonalteori (DFT). Materialene som har blitt undersøkt består utelukkende av datagenererte ternære tellurider på formen $ABTe_2$, med A=Li, Na, K, Rb og Cs, og B=Al, Ga og In i forskjellige konfigurasjoner. Prosjektet ble gjennomført som en screeningprosess hvor de forskjellige kandidatene ikke lenger ville bli evaluert dersom de ikke oppfølger forskjellige kriterier nødvendige for god fotokatalytisk ytelse. Den semi-lokale GGA funksjonalen PBEsol ble brukt for gjennomføringen av beregninger av elektronisk struktur og optiske egenskaper. Bidrag fra spinn-bane kobling ble også tatt hensyn til i kalkulasjonene. Prosjektet startet med 28 materialer som allerede hadde blitt evaluert til å være termodynamisk stabile. Blant disse hadde ti kandidater store nok båndgap og lave nok effektive masser for ladningsbærerne til å passere screeningkriteriene. Alle de gjenværende materialene ble så antatt til å være dynamisk stabile basert på fononspredningskalkulasjoner. Tre av kandidatene ble senere screenet ut grunnet lav fotonabsorpsjon for fotoner med energi nære det direkte båndgapnivået. Dermed gjenstår de indirekte absorberende kandidatene $Pna2_1$ $LiGaTe_2$, $I\bar{4}2d$ $LiGaTe_2$ og $C2/c$ $CsGaTe_2$. Kandidatene med et direkte båndgap som gjenstår er $Pna2_1$ $LiAlTe_2$, $Pna2_1$ $LiInTe_2$, $I\bar{4}2d$ $LiInTe_2$ og $C2/c$ $CsInTe_2$. Forbindelsenes A-kation ble analysert til å først og fremst påvirke gitterparametrene, mens B-kationet hadde en stor innvirkning på elektronstrukturen. De mest foretrukne strukturene danner hjørnedelende $[BTe_4]$-tetraeder, hvor både god orbital overlapp mellom s-orbitalene til B-kationet og p-orbitalene til Te leder til god båndspredning, uten at båndgapet blir for smalt. Denne foretrukne tetraederkonfigurasjonen oppstår i strukturene med romgrupper $I\bar{4}2d$ og $Pna2_1$.

List of Abbreviations

BZ	-	Brillouin Zone
CB	-	Conduction band
CBM	-	Conduction band minimum
CCS	-	Carbon capture and storage
DFT	-	Density Functional Theory
DOS	-	Density of states
GGA	-	General gradient approximation
LDA	-	Local density approximation
MP	-	Materials Project
NHE	-	Normal Hydrogen Electrode
PAW	-	Projector Augmented Wave
PBEsol	-	Perdew-Buke-Ernzerhof revised for solids
SOC	-	Spin-orbit coupling
VASP	-	Vienna Ab-initio Simulation Package
VB	-	Valence band
VBM	-	Valence band maximum

Contents

List of Tables

List of Figures

1 Introduction

Sustainability has been a common global goal for the past 30 years or so. Limiting the global warming to 2 °C, as promised in the Paris Agreement requires the extraction and safe storage of several gigatonnes of CO_2 each year. Carbon neutrality also necessitates a shift from fossil fuels to renewable energy sources, such as wind, water and solar power. If the technologies for sufficient harvesting and supplying solar energy were readily available, it could theoretically fulfill the energy demands of the entire world. Despite this huge potential and increased global awareness, the contribution of solar energy to the global energy supply is still negligible [2]. Further research is needed in order to develop technologies both for removing CO_2 from the atmosphere as well as producing renewable energy at larger industrial scales. Carbon capture and storage (CCS) is a technology that involves many different technologies that try to separate CO_2 from the air and store it underground in a supercritical state. Though research is making progress, none of the methods have proved to be economically viable, and depend on considerable energy input.

The photocatalytic reduction of CO_2 into solar fuels is a different way of converting excess CO_2 that uses solar power directly as its energy input. Solar fuels is in this context higher energy C1/C2 compounds such as CH_4, HCOOH, HCHO, CH_3OH or C_2H_5OH. These molecules store energy in the form of chemical bonds, mainly the C —— H-bonds. They have the advantage of being storable, transportable and usable upon demand and can additionally be used for chemical synthesis. The technology is on the macroscale easily compared to the photosynthesis happening continuously in nature and in plants all over the world. The biggest difference is that, instead of producing cellulose, the photocatalyst recycles combusted CO_2 into solar fuels, which again can replace fossil fuels. The problem, however, is that the perfect material for such applications has not yet been discovered. Most research has focused on TiO_2 which has been reported to work as a solar-powered CO_2-converter. However, the product yield in such devices is still too low for actual industrial implementation [3]. One of the problems for TiO_2 is its wide band gap, meaning that it is only able to absorb light in the UV-range.

Density Functional Theory (DFT) is a computational modeling method used to accurately predict relevant material properties, such as composition, structure and stability as well as mechanical, electronic and optical response. Recent advances in available computing power have permitted large-scale and predictive first-principles simulations of materials properties through open-source computational databases, such as Materials Project (MP) [4].

In this project a thoroughly computational analysis of theoretical ternary $ABTe_2$-compounds will be followed through, where A = Li, Na, K, Cs, Rb, and B = Al, Ga, In. The goal is to discover a potential candidate working as the photocathode for the photocatalytic reduction of CO_2. The computational method consists of DFT calculations on said compounds. This is done in order to evaluate the theoretical possibility of synthesizing the compounds in the lab as well as analyzing their photocatalytic performance. The project will follow a computational based screening strategy where different photocatalytic properties are calculated and the materials that fulfill the screening conditions are taken to the next set of calculations. Initial considerations that has to be taken into account are thermodynamic stability, electronic structure and optical properties. Analyzing these characteristics by computational modeling is precise, cost- and time-efficient.

2 Electronic structure calculations

2.1 Quantum mechanics

In order to understand the macroscopic properties of a material it is necessary to understand what the system looks like at a microscopic or even atomic level. The behaviour of electrons and particles can not be described by classical physics, so in order to mathematically describe their energy and motion, a new branch of physics had to be born. In the quantum world, systems are expressed with quantized energy levels, with a wave-particle duality, in reciprocal space, and with allowed and forbidden transitions. The Schrödinger equation is an attempt to describe such systems. It mathematically describes the ground state energy levels for a time-independent and non-relativistic system as:

$$\hat{H}\psi = E\psi \tag{2.1}$$

Here $\hat{H}$ is the Hamilton operator and Ψ is the set of eigenstates - the solutions - of the Hamilton operator. Each of these solutions, ψ_n, has an associated eigenvalue, E_n, that satisfies the eigenvalue equation. The Hamiltonian contains both kinetic and potential energy terms for each electron and nuclei of the system. Even though the equation looks simple enough, it becomes practically unsolvable by the complex nature of the Hamilton operator. Therefore, several approximations based on the system itself is vital. If we use a crystalline material as an example, we know that it consists of both atomic nuclei and electrons with different momentums, and electronic potentials providing interactions between each other. Fortunately, the Born-Oppenheimer approximation states that the motion of atomic nuclei and electrons can be treated separately and that the kinetic terms for nuclei can be neglected because they have a much higher mass than the electrons. This leads to a more complete description of the Schrõdinger equation:

$$\left[-\frac{\hbar^2}{2m}\sum_{i=1}^{N}\nabla_i^2 + \sum_{i=1}^{N}V(\boldsymbol{r}_i) + \sum_{i=1}^{N}\sum_{j<i}U(\boldsymbol{r}_i,\boldsymbol{r}_j)\right]\psi = E\psi \tag{2.2}$$

The three terms on the left side of the equation defines the kinetic energy of electrons, the interaction between each electron and the collection of atomic nuclei, and the interaction energy between each electron, in this respective order. For this Hamiltonian, ψ is the electronic wave function depending on each spatial coordinate for all N electrons. ψ is approximated to a product of each individual electron wave function, $\psi = \psi_1(\mathbf{r})\psi_2(\mathbf{r}),...,\psi_N(\mathbf{r})$. Thus, the equation can be solved for N individual wavefunctions rather than 3N wavefunctions. Still, for most calculations, N is a very large number and solving equation 2.2 would be a costly procedure. We know that a periodic potential exists throughout the crystal because of the periodically organized ions that make up the lattice. The Bloch theorem states that for systems in a periodic potential, the solutions of the Schrödinger equation takes the form of a plane wave modulated by a periodic function. Mathematically this can be described as:

$$\phi_k(\mathbf{r}) = e^{i\mathbf{k}\cdot\mathbf{r}}u_k(\mathbf{r}) \tag{2.3}$$

where $\mathbf{k}$ is the reciprocal space wave vector and $\mathbf{r}$ is the position of the ion in the real space unit cell. The plane wave, ϕ_k is often referred to as a Bloch state. The periodicity of the bloch function means that the bulk properties of the crystal can be fully described by the area where every k-vector gives a unique bloch state. This area is referred to as the first Brillouin Zone and is defined for $-\frac{a}{\pi} < \mathbf{k} < \frac{a}{\pi}$, where a is the Bravais lattice vector.

We have now gathered quite a lot of information on both the Hamilton-operator and the possible solutions of the Schrödinger equation. To further solve the equation, Density Functional Theory (DFT) will be applied.

2.2 Density functional theory

Density functional theory is a computational quantum mechanic modelling tool used to investigate the electronic structure of many-bodied systems. The following and brief explanation of the ground principles behind it is inspired by the book "Density Functional Theory - A Practical Introduction"[5].

DFT is a method used to calculate ground state energies by solving the time independent and nonrelativistic Schrödinger equation 2.1. What is special with DFT is that it describes the energy as a function of the electron density rather than the wavefunctions. The method is valid because of two fundamental mathematical theorems proved by Kohn and Hohenberg, along with a set of equations derived by Kohn and Sham.

2.2.1 Hohenberg-Kohn theorems

The first of the Hohenberg-Kohn theorems tells us that: *The ground-state energy from Schrödinger's equation is a unique functional of the electron density.* This can be described mathematically by:

$$E = E[n(\mathbf{r})] \tag{2.4}$$

Where E equals the same ground state energy as in equation 2.2 and $n(\mathbf{r})$ is the electron density. This is again related to the individual wave function, ψ_i with

$$n(\mathbf{r}) = 2\sum_i \psi_i^*(\mathbf{r})\psi(\mathbf{r}) \tag{2.5}$$

Further on, the second theorem states that: *The electron density that minimizes the energy of the overall functional is the true electron density corresponding to the full solution of the Schrödinger equation.* Together, these two theorems assert that the ground-state electron density uniquely affects all properties, including its energy and wave function of the ground state. Solving the Schrödinger equation is thereby reduced to a problem of three spatial variables of the energy densities rather than the 3N variables of the wavefunction. Unfortunately, neither of the theorems reveal the true form of the energy functional.

2.2.2 Kohn-Sham equation

Kohn and Sham realized that finding the correct electron density could be expressed in a way that only involved a set of equations where each equation only involves a single electron. They rewrote the time-independent Schrödinger equation in terms of an individual wavefunction, ψ_i:

$$\left[-\frac{\hbar^2}{2m}\nabla^2 + V(\mathbf{r}) + V_H(\mathbf{r}) + V_{XC}(\mathbf{r})\right]\psi_i(\mathbf{r}) = \epsilon_i\psi_i(\mathbf{r}) \tag{2.6}$$

The two last terms have now replaced the unknown electron-electron interaction term from equation 2.2. V_H is called the Hartree potential and is defined by:

$$V_H(\mathbf{r}) = e^2 \int \frac{n(\mathbf{r}')}{|r - r'|} d^3 r' \tag{2.7}$$

V_H defines the repulsion between an electron and the total electron density. However, as the electron is a part of the electron density itself, this causes an unphysical self-interaction contribution. This is corrected for in the last and unknown term in equation 2.6, V_{XC}, namely the exchange-correlation potential.

2.2.3 The Exchange-Correlation Functional

Defining the exchange-correlation is no easy task. There is only one case where it can be derived exactly. That is when the electron density is constant in all points of space: the electron gas. The local density approximation (LDA) takes advantage of this and defines V_{XC} as

$$V_{XC}(\mathbf{r}) = V_{XC}^{electron\ gas}[n(\mathbf{r})] \tag{2.8}$$

LDA can be a useful approximation because it is easily applied to many systems, but it is not really accurate. Today it is more common to use the general gradient approximation (GGA), where the gradient of the electron density is taken into account. There exists a bunch of different GGA functionals, all having their pros and cons. PBEsol is commonly used for structural relaxation for solids and accurately predicts lattice parameters, formation energies and phonons[6]. However it is known that in LDA and GGA-type of functionals, the orbitals are sometimes too delocalized and hence contribute to the narrowing of the band gap. PBEsol is, as an example, expected to underestimate the band gap by ~40% compared to the real one [7]. These anomalies are caused by the discontinuity of the functional derivative of the exchange correlation [8]. Hartree-Fock type of functionals, on the other hand, are known to localize electrons too much, causing an overestimation of the band gap. A hybrid functional is a mix between local or semi-local functionals and Hartree-Fock functionals where the delocalisation and localisation cancel out and gives a good estimation of the band gap. Despite its greater functionality, a hybrid functional will not be used in this project due to its higher computational cost.

2.2.4 Solving the equations

Putting this all together shows that a Hartree potential is necessary for solving the Kohn-Sham equations. The electron density is necessary to calculate the Hartree potential, but this is dependent on the single-electron wave functions that comes from solving the Kohn-Sham equations. Therefore an iterative way of solving the equations have been developed:

1. Define an initial, trial electron density, $n(\mathbf{r})$.
2. Calculating the Hartree potential from equation 2.7.
3. Calculate the summed potentials given a specific exchange-correlation functional.
4. Solving the Kohn-Sham equation (2.6) to find the single-particle wave function $\psi_i(\mathbf{r})$.
5. Using this result to again calculate electron density from equation 2.5
6. Comparing this result to the initial electron density. If the guess was wrong you go back to the first step guessing the calculated electron density.

This loop is called the electronic convergence loop. When the initial and calculated energy densities are the same you have approached the the ground-state electron density which can be used to compute the total energy.

2.3 Pseudopotentials

The electronic structure for solids is mainly determined by the outer valence electrons. The *frozen core* approximation states that the core electrons are not important for either bonding or other properties and are fixed to the core [9]. Consequently they can be treated equally no matter the rest of the system. In DFT calculations, pseudopotentials are used to imitate the potential of the nucleus along with its core electrons. Different sets of pseudopotentials also determines the cutoff frequency as an upper threshold for which Bloch states should be evaluated or not. Core electrons are associated with plane waves oscillating on short length scales in real space and with high energies. The plane waves with higher energy than the cutoff frequency can be left out of the calculation. The most common used pseudopotentials used today derive from the projector augmented wave (PAW) method introduced by Blöchl, Kresse and Joubert [10].

3 Photocatalysis

3.1 Semiconductor physics

All solid materials contain electrons and are often categorized by how the electrons within the materials respond to an applied electric field. Semiconductors are classified as materials with a narrow band gap, meaning that there is a narrow energy gap between what is called the valence band (VB) and conduction band (CB). The VB is made up of orbitals with a bonding nature, while the orbitals of the CB have an antibonding nature. This means that electrons in the VB contribute to the bonds holding the material together, while electrons in the CB are free to move around the structure and is therefore contributing to the electric conductivity of the material. To retrieve information about the electric properties it is therefore important to gain information both about the electron energies as well as the intrinsic orbital energies of the materials. The electron energy increases as a function of temperature according to $E = k_b T$,where k_b is the Boltzmann constant and T is the temperature. The possible states that electrons can occupy as a function of energy is referred to as the density of states (DOS). In the free electron model, where an electron can move freely throughout the structure without interacting with other electrons, the density of states is described mathematically as:

$$DOS(E) = \frac{dN}{dE} = \frac{V}{2\pi^2}(\frac{2m}{\hbar^2})^{\frac{3}{2}}\sqrt{E} \tag{3.1}$$

where V is the crystal volume and m is the mass of an electron. However, this is not the case for semiconductors where electrons are subject to periodic potentials. As electrons are fermions, the electron distribution is controlled by the Fermi-Dirac distribution at a given temperature [11]:

$$f(E) = \frac{1}{e^{\frac{E-\mu}{k_B T}} + 1} \tag{3.2}$$

where μ is the chemical potential of an electron. The chemical potential is weakly dependent on temperature, but this is often neglected and μ is set equal to the fermi energy, E_F, being the chemical potential for electrons at 0K. Multiplying the density of states with the Fermi-Dirac distribution gives us to the occupied density of states. Because of the narrow band gaps of semiconductors they behave as insulators at low temperature, but with increasing conductivity as the temperature rises. This behaviour is related to the equilibrium state in semiconductors, meaning how they behave in the dark without illumination

Electrons can, however, also be excited from the valence band to the conduction band through photon absorption. Photons with frequency ν and energies $E_{ph} = h\nu$ can be absorbed by the material as long as the photon energy is equal to, or greater than, the band gap energy. The absence of the excited electron in the valence band is treated as a charge carrying quasiparticle called electron hole, which, in contrast to the electron, will have a positive charge. The electron hole will also work as a charge carrier and is the main contributor to conductivity in p-type conductors.

3.1.1 Band diagrams

The energy levels of the VB and CB are often illustrated by the use of band diagrams, showing how the energies of the bands changes as a function of **k** in reciprocal space. It will however be impossible to plot the energies in three different spatial directions of **k** and so, band diagrams are two-dimensional unfoldings of the four-dimensional case. All Brillouin zones are characterized with certain points in the structure with high symmetry and when plotting the band diagrams, only the high symmetry points are

taken into account. The high symmetry points located inside the first Brillouin zone are given greek letters, with the Γ-point always being in the center. The points at the boundary of the first Brillouin zone is given roman letters. In the case where the valence band maximum (VBM) and conduction band minimum (CBM) is located at the same **k**-vector, the band gap is called direct, while if they are located at different points in reciprocal space it is an indirect band gap semiconductor. An example of a band diagram is provided in Fig 3.1.

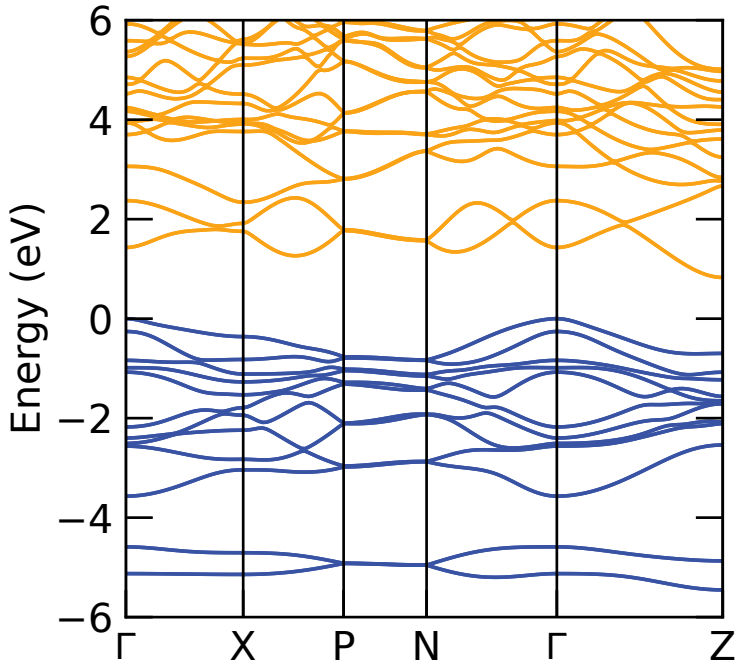

Figure 3.1: An example of a typical band diagram of an indirect band gap semiconductor. The energy of the VBM is set to 0 and is located at the Γ-point, while the CBM is located at the Z-point.

Because electrons move differently in a crystal lattice than in a vacuum, an effective electron mass, m^*, is introduced. This parameter takes into account the electrostatic forces from ions and other electrons as well as other quantum effects. By including this parameter both electron and hole can be described in a semi-classical way [11]. In one dimension the effective mass is described by the equation:

$$m^* = \frac{\hbar^2}{\frac{\partial^2 E}{\partial^2 k}} \tag{3.3}$$

Thus, the slope of the energy curve when moving through **k**-space depends on the effective masses of the charge carriers. Consequently, small effective masses, for which electrons and holes can move freely, relate to curvy bands, while heavier charge carriers with low mobility is related to flat bands.

3.1.2 Absorption and recombination

As already explained, photons with energy, $E_{ph} = h\nu$ can excite electrons from the VB to the CB as long as the energy of the incoming photon is larger than the direct band gap energy: $E_{ph} > E_g$. The very small and negligible **k**-contribution of the photon is not enough to initiate an indirect transition. The indirect absorption happens as a result of interacting with the crystal lattice. Consequently an indirect band gap

is dependent on both the photon absorption as well as the absorption or emission of the quasi-particle depicting the collective excitation of vibrations in the crystal lattice, known as phonons. This means that the probability for an indirect transition with sufficient energy is much lower than the probability of a direct transition. The absorption coefficient, α, for the direct case can be approximated to

$$\alpha \propto (E_{ph} - E_g)^2, \tag{3.4}$$

while for the indirect case the approximation is

$$\alpha \propto (E_{ph} - E_g)^{\frac{1}{2}}. \tag{3.5}$$

This coefficient relates to the attenuation of light travelling a distance, x, through the structure with incident intensity I_0 through the Lambert-Beer law[12]:

$$I = I_0 \cdot e^{-\alpha x} \tag{3.6}$$

This all leads to two quite different design principles for indirect and direct semiconductors because the indirect semiconductors need a larger thickness in order to have sufficient absorption. The idea of photocatalytic devices is to get the excited charge carriers to move through the bulk to an adhered substrate at the interface. Consequently, indirect band gap photocatalysts need longer charge carrier diffusion lengths such that the electron and hole are able to travel to the interface before they recombine. There are many different intrinsic recombination mechanisms that can not be avoided. The most important contribution, however, is the radiative recombination where the electron travels back down from the CB to the VB and emits a photon in the process. The full absorption and recombination process is illustrated in Fig 3.2. Arrow (1) shows the direct absorption of an incident photon with sufficient excitation energy. The excited electron will then follow arrow (2) in a process called thermalization. The electron loses energy when interacting with the lattice until it reaches the CBM value. Arrow (3) depicts the indirect absorption and recombination where both a photon and a phonon contribute to the transition. Arrow (4) and (5) show the process of hole and electron trapping in energy levels induced by defects.

Despite the longer diffusion path, an indirect band gap is beneficial for photocatalytic applications. Thermalization is a much faster process than recombination. This means that for indirect band gap semiconductors, a direct excitation is still possible as long as the energy of the photon is large enough, but the recombination will be indirect due to thermalization.

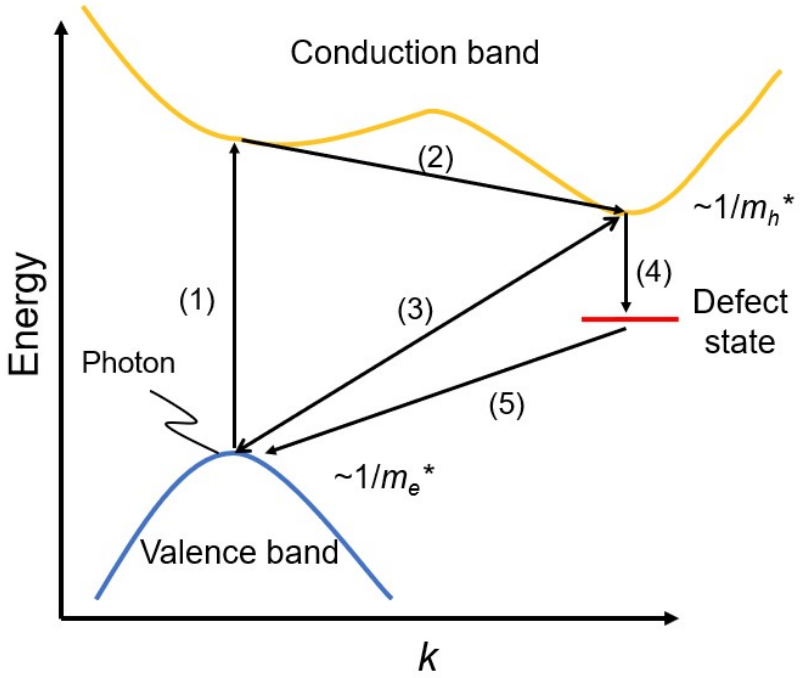

Figure 3.2: The absorption of a photon in a semiconductor. (1) corresponds to a direct optical absorption with photon energy higher or equal to the band gap of the semiconductor. (2) is thermalization, where the electron loses potential energy. (3) relates to band-to-band recombination or the indirect absorption also including a phonon. (4) and (5) shows the process of electron and hole trapping by defects.

The probability for the transition of an electron going from the VB to the CB can, according to first-order perturbation theory and Fermi's Golden Rule, be described mathematically with the transition moment integral,

$$\int_{-\infty}^{\infty} \psi_{el} \hat{M} \psi_{el}^{ex} d\tau = |\langle i|M|f\rangle| \tag{3.7}$$

where ψ is the electron wave function, i and f refer to the initial and final state and M is the transition dipole moment operator. The integral must be non-zero in order for a transition to occur, meaning that a transition is only allowed if two electronic states overlap. This gives rise to quantum mechanical selection rules such as the Laporte and spin-selection rules. The Laporte Rule states that in a centrosymmetric system, the integrand from equation 3.7 needs to contain the entire symmetric representation of the transition for it to be allowed. This gives rise to parity-forbidden transitions when the two electronic states have the same parity. This relates to the nature of the wavefunction and if it is changed upon inversion or not [13].

3.2 Photocatalysis

The energy of the excited electrons in the conduction band equals the energy of the incoming photon that excites it. However, if the energy is larger than the band gap energy, the electron will lose the excess energy due to thermalization. The remaining potential energy is what is exploited and turned into electrical energy in solar cells or used to overcome energy barriers in chemical reactions for photocatalysis. In photocatalysis, the electron-hole pair needs to travel throughout the structure to interact with adsorbed chemical species at interfaces. The electron works as a reducing agent, while the hole acts as an oxidizing agent. In order for this to work, the band gap energy of the semiconductor has to be larger than the redox potential of the wanted reaction to occur. However, having a too high energy gap would lead to fewer absorbed photons, and therefore fewer excited electron-hole pairs.

3.2.1 CO_2-reduction

The CO_2-molecule is a fully oxidized and highly thermodynamically stable molecule due to its linear C$\equiv$O-bonds. The amount of CO_2 in the atmosphere has increased in the past years through human alteration of the carbon-cycle, mainly by combustion of fossil fuels. Removing CO_2 in the atmosphere through reduction into solar fuels can be seen as a recycling process. The recombustion of the solar fuels will again lead to CO_2-emissions, but as it is a renewable energy source, it will not affect the carbon-cycle. The various potential reduction routes for the CO_2-molecule are described in Table 3.1.

Table 3.1: Important reduction potentials for CO_2-reduction as well as water splitting [14][15].

	Reduction potentials of CO_2	E^0 [V] vs SHE at pH 7
(3.8)	$CO_2 + e^- \longrightarrow CO_2^{\bullet -}$	-1.9
(3.9)	$CO_2 + 2\,H^+ + 2\,e^- \longrightarrow HCOOH$	-0.61
(3.10)	$CO_2 + 2\,H^+ + 2\,e^- \longrightarrow CO + H_2O$	-0.52
(3.11)	$CO_2 + 6\,H^+ + 6\,e^- \longrightarrow CH_3OH + H_2O$	-0.38
(3.12)	$CO_2 + 8\,H^+ + 8\,e \longrightarrow CH_4 + 2\,H_2O$	-0.24
(3.13)	$2\,H^+ + 2\,e^- \longrightarrow H_2$	-0.41
(3.14)	$2\,H_2O + 4\,h^+ \longrightarrow O_2 + 4\,h^+$	+0.82

Due to the high negative redox potential of the one-electron reduction of $CO_2/CO_2^{\bullet -}$, the process would rather follow the multi-electron and proton-assisted steps. The whole process will take place in water due to its abundancy, low-price and its ability to work as both an electron donor and proton source. H_2O is used as a reducing agent, where it interacts with positive holes in the VB of the semiconductor, oxidizing it to O_2. However, it can also be reduced to H_2 by interacting with electrons in the CB. This leads to a fight over the CB electrons between both CO_2 and H_2O. This problem has been subject to extensive research [3], and can be solved by the design of the photocatalyst, for instance by separating the cathode and anode in heterogeneous layers, or by using co-catalysts, two methods that both helps in the CO_2 and H_2O adsorption as well as in the redox reaction [16]. One can also make sure that this will not happen at a great extent by looking at the band gap alignements of the semiconductor compared to the redox-potentials of the CO_2 reduction and water splitting reaction [17].

The mechanism behind the photocatalytic reduction of CO_2 is illustrated in Fig 3.3. Incoming photons with energies $E_{ph} > E_g$ excites electrons from the VB to the CB. The different bands straddle the redox-potentials of the H_2O oxidation and the CO_2 reductions such that the redox reactions will be thermodynamically favourable. Because of the many alternative reaction routes and the fact that different reactions have similar reduction potentials, the exact product of the reaction can be hard to predict. Consequently,

it will also lead to a low selectivity of the desired product [18]. Several studies have been completed on analyzing the exact reaction mechanism, weighing in the factors affecting the CO_2 reduction. Possible impacts can be the characteristics and vacancies of the semiconductor interface and even the angle of the adsorbed CO_2-molecule [19].

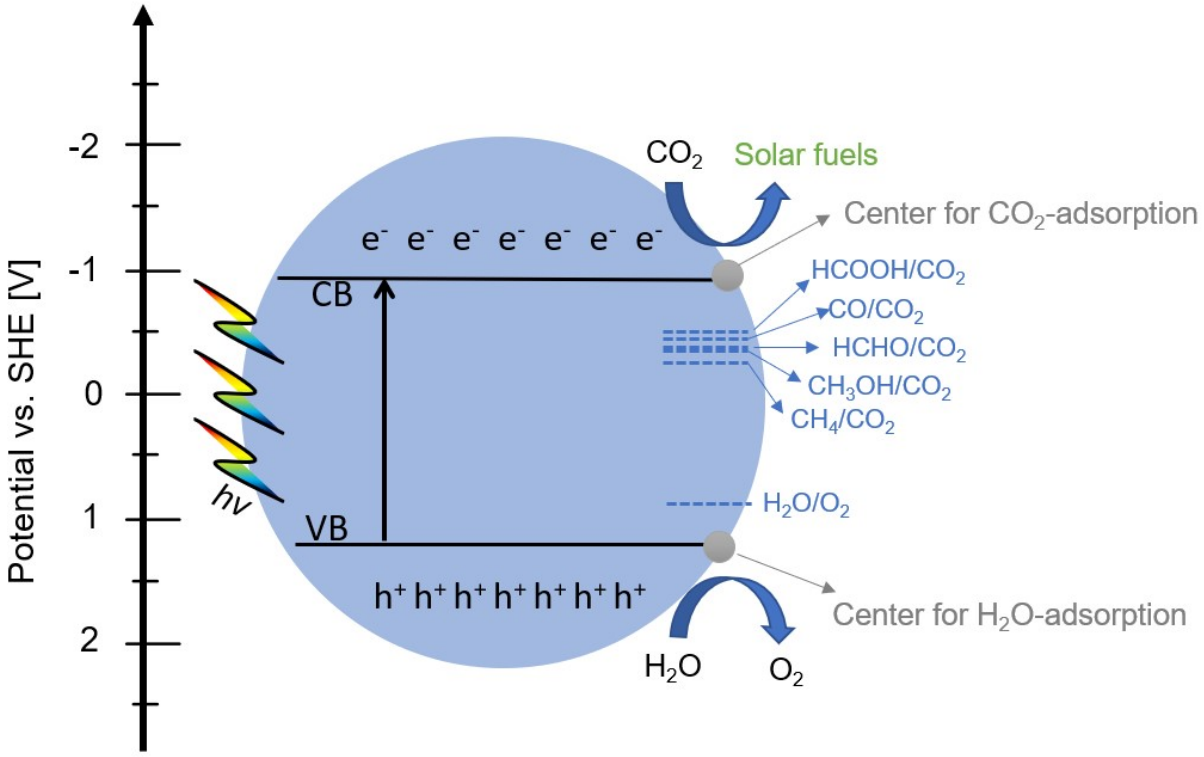

Figure 3.3: Schematic illustration of possible mechanism of photocatalytic CO_2-conversion into solar fuels by using a semiconductor. The band gap is sufficiently large such that it straddles the redox-potentials. The placement of the redox-potentials correspond to the values introduced in Table 3.1. CO_2 is reduced to solar fuels with the help of the electrons in the CB, while H_2O is oxidized to O_2 by the holes in the VB. The adsorption centers in modern day devices are different variations of co-catalysts.

3.2.2 Fundamentals of photocatalytic semiconductor design

In order to summarize the information given in the preceding section, the photocatalytic reduction of CO_2 is divided into 3 steps:

1. The first step consists of the photon absorption and electron-hole pair generation. To make sure that the generated electrons and holes contribute to the reaction, the conduction band edge in the band diagram needs to be more negative than the reduction potential for CO_2 and the valence band edge needs to be more positive than the reduction potential of water oxidation. This also needs to take into account overpotentials and other potential losses. However, a too high band gap will lead to lower absorption rates. Taking all these points into consideration leads to a wanted band gap of $E_g = 2.0 - 2.4eV$, with an additonal good band edge alignment.

2. The second step is the spatial separation of charge carriers. Electrons and holes need to be able to travel through the structure without recombining. Favourable properties in order to achieve this is

a slightly indirect band gap, together with low effective masses of both electrons and holes. Additionally, the material should be pure and have a low defect concentration to avoid charge carrier trapping.

3. The third step is the actual redoxreaction, where CO_2 is reduced and H_2O is oxidized. Additionaly, the process includes both the adsorption of CO_2 to the interface, and the desorption of the product after the reaction has taken place in order to avoid re-oxidation [20].

3.3 Tellurium materials

Tellurium is one of the least abundant elements in the lithosphere. Consequently, there is not much data published about its technological uses or the environmental impact of elemental Te in nature. Nevertheless, both of the ions Te(IV) and Te(VI) are considered to be toxic [21]. In the more recent years, Te has gotten more attention due to its uses in photovoltaics. Up-and-coming thin film solar cells of CdTe has shown great efficiencies with up to 19% in commercial modules. They have been reported to have very low environmental impact, with the largest risk being Cd leakage into the soil for broken modules [22]. According to VWR's safety data sheet, elemental Te is toxic if swallowed and safety precautions such as gloves and face masks should be worn when working with it. Because of its historically low technological importance Te has mainly been sourced as a by-product from Cu or Ni production. However, to meet future demands a larger search for Te deposits is necessary. There already exists mining facilities, even in Norway, that have larger Te deposits which can be of economic importance in the following years as the Te price is expected to rise [23].

Because of both high cost and low natural occurrence it would be reasonable to consider other anions. The majortiy of previous experimental data on photocatalytic CO_2-reduction has focused on oxides. The problem with oxides, however, is twofold. First of all, oxides typically have VBM of localized 2p orbital character leading to high hole effective masses. Secondly, the VBM tend to have a high ionisation potential, which means that the energy levels are located deep below the vacuum level, increasing the band gap necessary to straddle the redox potentials for the CO_2-reduction [24].

From before the most used semiconductor for these applications is TiO_2, which have proven to be very successful in both water splitting and CO_2 reduction. However, TiO_2 is a wide band semiconductor with $E_g = 3eV$, and therefore only absorbs UV light. New types of design principles involving heterojunctions and Z-schemes (aiming to imitate the reaction found in plans) are evolving, but they are still far from large-scale industrial implementation [25].

3.4 Lattice dynamics

As long as the temperature is not 0 K, all atoms in a lattice will vibrate. These small vibrations lead to nuclei continuously moving closer and further away from each other.. This quantum oscillating effect is described by the unit of vibrational energy arising from the thermal energy of the atoms and has previously been introduced as phonons.

Phonons are mostly important to describe how heat is transported throughout a material, but it can also be used as a tool to describe a materials inherent dynamic stability. The acoustic phonons are expected to rise from the Γ-point centre with the speed of sound of the material. However, for hypothetical materials there is a possibility of discovering negative phonons, which is unphysical and depicts poor dynamic stability. In order to evaluate the dynamic stability of hypothetical materials the phonon dispersion relations therefore needs to be evaluated[26]:

Fig 3.4 paints an easy, one-dimensional picture of a crystal lattice with atoms at their equilibrium positions.

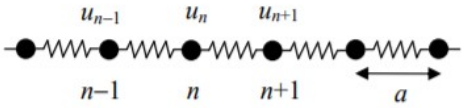

Figure 3.4: 1D monoatomic lattice with interatomic distance a.

Applying the harmonic approximation, which states that the forces working between the atoms are proportional to their relative displacements, we obtain from Hooke's law that the forces working on the n-th atom from its nearest neighbours:

$$F_n = C(u_{n+1} - u_n) + C(u_{n-1} - u_n) = -C(2u_n - u_{n+1} - u_{n-1}) \tag{3.15}$$

where C is the interatomic force constant and u_n is the atomic displacement. Applying Newton's second law leads to the differential equation:

$$M\frac{d^2u_n}{dt^2} = -C(2u_n - u_{n+1} - u_{n-1}) \tag{3.16}$$

where M is the mass of the atom. Solving for the entire system means that a similar equation should be written for all N atoms in the lattice, leading to N differential equations that should be solved at the same time. But because we are in a periodic crystal lattice we can again look for a solution in the form of a travelling Bloch wave:

$$u_n = u_0 e^{i\mathbf{q}x-\omega t}. \tag{3.17}$$

All atoms will then oscillate with the same frequency ω, have the amplitude u_0 and wavevector $\mathbf{q}$. Substituting 3.17 into 3.16 and solving for ω gives us the relationship between the frequency of vibrations and wavevector $\mathbf{q}$:

$$\omega = \sqrt{\frac{4C}{M}}\left|\sin\frac{qa}{2}\right| \tag{3.18}$$

This solution is periodic and can be reduced to just the first Brillouin Zone, i.e. $-\frac{\pi}{a} \leq \mathbf{q} \leq \frac{\pi}{a}$. It is also clear that $\omega(\mathbf{q} = 0) = 0$.

Introducing an additional atom in the one-dimensional lattice leads to a different case, however. To describe the system, two equations of motion are now needed:

$$M_1 \frac{d^2 u_n}{dt^2} = -C(2u_n - u_{n+1} - u_{n-1})$$
$$M_2 \frac{d^2 u_{n+1}}{dt^2} = -C(2u_{n+1} - u_{n+2} - u_n) \tag{3.19}$$

We are still looking for the solution on the form of a traveling mode for the two atoms:

$$\begin{bmatrix} u_n \\ u_{n+1} \end{bmatrix} = \begin{bmatrix} A_1 e^{iqna} \\ A_2 e^{iq(n+1)a} \end{bmatrix} e^{-i\omega t} \tag{3.20}$$

Using the same method as before leads to a system of linear homogeneous equations and eventually the solution:

$$\omega^2 = C\left(\frac{1}{M_1} + \frac{1}{M_2}\right) \pm C\sqrt{\left(\frac{1}{M_1} + \frac{1}{M_2}\right)^2 - \frac{4\sin^2(\mathbf{q}a)}{M_1 M_2}} \tag{3.21}$$

The frequency ω here has two different solutions leading to two different dispersion curves, one strictly positive and one with the trivial solution $\omega(0) = 0$ [27].

For the threedimensional and multiatomic case, the mathematics get more complicated. However, the nature of the solutions remain the same. The non-zero branches are called optical phonons, while the branches going towards zero for $\mathbf{q} = 0$ are the acoustic phonons. The phonon dispersion diagrams are plotted only with q-vectors in the high symmetry directions, as explained earlier in section 3.1.1 for the band diagrams. An example of such a diagram is presented in Fig 3.5. A clear distinction can be seen between the optical and acoustic phonons and that the acoustic phonons go to zero at the Γ-point. The frequencies all correspond to a restorative force for the atoms to go back to its start positions. Negative modes correspond to imaginary frequencies where no such restorative force is present. Normal modes with negative energies along their displacement vector $\mathbf{q}$ might indicate that there exists an energy favourable distortion of the cell in the form of a displacive phase transition, but that the compound might still be stable at room temperature. As the Γ-point represents the $\mathbf{q}$=0 case, the phonon modes at this point would be the entire cell moving in unison. Negative modes at this point would therefore indicate that the structure is dynamically unstable [26].

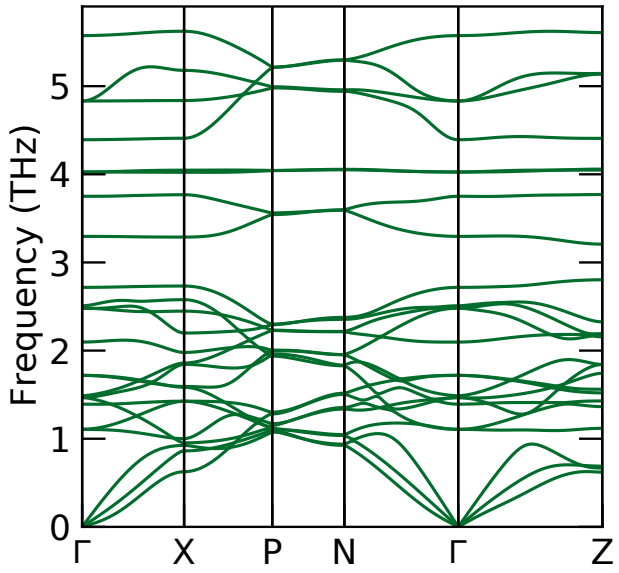

Figure 3.5: Example of a typical phonon dispersion relation, where a clear distinction between the acoustic and optical phonons is present. All vibrational modes are positive, and so the material with this phonon dispersion relation will be dynamically stable.

4 Computational methodology

This project is a computational materials search for a potential semiconductor suitable for photocatalytic CO_2 reduction. The main focus is the electronic and optical properties of the semiconductor, while more practical issues such as synthesize routes, material design, use of co-catalysts and so on has to be evaluated at a later stage.

4.1 VASP

Vienna Ab-initio Simulation Package (VASP) is a program for performing first principle calculations for atomic scale materials modelling. In this project, DFT will be used to approximate solutions of the Schrödinger equation using VASP. The computations were performed on resources provided by UNINETT Sigma2 - the National Infrastructure for High Performance Computing and Data Storage in Norway.

4.1.1 Input files

To run calculations on VASP the following input files are necessary: INCAR, POSCAR, POTCAR, job and KPOINTS. The different files will be briefly explained in the following subsection, while an example of all input-files can be found in Appendix B

- **INCAR**
  The INCAR-file includes a lot of different parameters giving information about what to do and how to do it. The most important parameters are listed here, but a more complete explanation can be found on the VASP-wiki INCAR site. [28]
  - EDIFF - Defines the treshold difference between the initial energy and calculated energy in the convergence loop.
  - GGA - Specifies the functional for the exchange-correlation potential.
  - NSW - Defines the number of ionic steps.
  - IBRION - Chooses the convergence algorithm.
  - ISMEAR - Energy smearing approximates the states in between the k-points with a function.
- **POSCAR**
  This file contains information about the geometry of the lattice as well as all ionic positions.
- **KPOINTS**
  Defines the sampled k-point density. It usually consists of a Γ-centered mesh with varying k-points in the different directions according to the Monkhorst-Pack scheme [29].
- **POTCAR**
  Here you will find the pseudopotentials for all the elements included in the structure. It is generated through VASP's own implemented code.
- **job**
  More general information are found here, including the name of your account, the name of the job, maximum computing time and how many nodes that are requested for the job.

4.1.2 Output files

- **OUTCAR**
  The most comprehensive of the output files. It includes information about all the electronic steps and forces on the atoms.
- **CONTCAR**
  An updated version of the POSCAR with slightly displaced atoms to minimize the energy.
- **DOSCAR**
  Contains information about the calculated DOS.
- **vasprun.xml**
  Provides the data in a format that can be used as an input-file for data processing and plots.

4.2 Earlier work

The project is a continuation of introductory work already completed by Råheim [1]. The following is therefore a brief explanation of what has already been completed.

The materials of interest at the beginning of the project were computer generated ternary tellurides with the composition $ABTe_2$, where A = Li, Na, K, Cs, Rb and B = Al, Ga, In. The compounds were computer generated by finding stable crystal structures with similar compositon at the Materials Project database [4], and then swapping the different ions so that it follows the $ABTe_2$-composition using the python package pymatgen [30] [31] [32]. This resulted in 15 different compositions, each with 11 space group variations and therefore 165 potential candidates. The different crystal structures that were used as a basis for the generation of the wanted telluride structures are shown in Table 4.1. Additionally, the compounds that already existed at the MP database with the desired composition was included.

Table 4.1: Table of generated crystal systems. The number and space group symmetry are described using Herman Mauguin notation. Nsites correspond to the number of atoms in the cell and the mp-id to the compound's identification number at the MP database.

#	Symmetry	Space group	Nsites	Origin	mp-id
15	Monoclinic	$C2/c$	8	$CsGaS_2$	mp-5038
15	Monoclinic	$C2/c$	32	$CsInTe_2$	mp-1199743
33	Orthorombic	$Pna2_1$	16	$NaGaO_2$	mp-3338
61	Orthorombic	$Pbca$	64	$CsGaO_2$	mp-1213401
92	Tetragonal	$P4_12_12$	16	$KAlO_2$	mp-12807
109	Tetragonal	$I4_1/md$	8	$LiInO_2$	mp-1222354
122	Tetragonal	$I\bar{4}2d$	8	$KInSe_2$	mp-1120779
140	Tetragonal	$I4/mcm$	8	$RbInTe_2$	mp-22255
141	Tetragonal	$I41/amd$	8	$LiInO_2$	mp-5488
166	Trigonal	$R\bar{3}m$	4	$KInO_2$	mp-1018031
227	Cubic	$Fd\bar{3}m$	8	$CsGaO_2$	mp-1178397

4.2.1 Thermodynamic stability

The thermodynamic stability for all of the candidates were decided by calculating the ΔE_{hull} for each structure. This was done by relaxing all available MP-compounds for the A-B-Te system as well as the

acquired candidates. The ΔE_{hull}-values for the candidates were calculated by comparing all the DFT-energies for all the possible structures in the system using the python package pymatgen's phasediagram analysis [33]. An upper threshold was introduced to screen out the most unstable compounds at $\Delta E^{hull} > 0.03$. The compounds that passed the thermodynamic stability screening is reported in table 4.2.

Table 4.2: Compounds passing the initial thermodynamic screening. ΔE^{hull} is the energy of decomposition of a material into the set of most stable materials at this chemical composition.

Structure	Spacegroup		Symmetry	Nsites	ΔE^{hull} [eV]
$LiAlTe_2$	122	$I\bar{4}2d$	Tetragonal	8	0.000
	33	$Pna2_1$	Orthorombic	16	0.002
$LiGaTe_2$	122	$I\bar{4}2d$	Tetragonal	8	0.000
	33	$Pna2_1$	Orthorombic	16	0.004
$LiInTe_2$	122	$I\bar{4}2d$	Tetragonal	16	0.000
	33	$Pna2_1$	Orthorombic	16	0.003
$NaAlTe_2$	140	$I4/mcm$	Tetragonal	8	0.000
$KAlTe_2$	140	$I4/mcm$	Tetragonal	8	0.000
	15	$C2/c$	Monoclinic	8	0.023
	15	$C2/c$	Monoclinic	32	0.010
$KGaTe_2$	140	$I4/mcm$	Tetragonal	8	0.000
	15	$C2/c$	Monoclinic	8	0.030
	15	$C2/c$	Monoclinic	32	0.013
$KInTe_2$	140	$I4/mcm$	Tetragonal	8	0.000
	15	$C2/c$	Monoclinic	8	0.000
$RbAlTe_2$	140	$I4/mcm$	Tetragonal	8	0.008
	15	$C2/c$	Monoclinic	8	0.013
	15	$C2/c$	Monoclinic	32	0.000
$RbGaTe_2$	140	$I4/mcm$	Tetragonal	8	0.008
	15	$C2/c$	Monoclinic	8	0.026
	15	$C2/c$	Monoclinic	32	0.000
$RbInTe_2$	140	$I4/mcm$	Tetragonal	8	0.000
	15	$C2/c$	Monoclinic	32	0.022
$CsGaTe_2$	15	$C2/c$	Monoclinic	8	0.023
	15	$C2/c$	Monoclinic	32	0.000
$CsInTe_2$	140	$I4/mcm$	Tetragonal	8	0.002
	15	$C2/c$	Monoclinic	8	0.024
	15	$C2/c$	Monoclinic	32	0.000

To differentiate the two monoclinic cells with the same space group, they will from now on be referred to as $C2/c$_8 and $C2/c$_32 depending on the number of atoms in the cell. It is also worth noticing that the $I\bar{4}2d$-phase of $LiInTe_2$ consist of a larger cell than its counterparts $LiAlTe_2$ and $LiGaTe_2$.

4.3 Computational approach

As this is a continuation of Råheim's project, the initial input-files were influenced by earlier results. The structure POSCAR-files correspond to already relaxed CONTCAR-files while the POTCAR-files are identical as before and produced via the VASP implemented PAW formalism.

4.3.1 Band structure calculations

PBEsol band structure calculations with a Γ-centered k-mesh has already been completed and plotted with the python package amset [34][35] by Råheim. The results were, however, predicted to be unprecise, and so new bandstructures with a wider selection of k-points were produced for this project.

To start off the band structure calculations a DOS-calculation was run by simply switching the following parameters in the INCAR:

- NSW = 0
- NEDOS = 2000
- LORBIT = 11
- ISMEAR = 0
- IBRION = -1
- SIGMA = 0.2

This first calculation is done in order to generate a CHG-,CHGCAR- and WAVECAR-file. These outputfiles contain information about the charge density and predicted wavefunctions, and allows the next step of calculations to run faster as these parameters already are predicted. The NEDOS correspond to the number of intervals the energy frequency is divided into, LORBIT=11 correspond to a calculation of DOS with contribution from each orbital, ISMEAR=0 means that the points in between two sampled k-points will be smeared out with a Gaussian function, similar to a normal distribution, with SIGMA defining the width of the smearing. The combination of IBRION=-1 and NSW=0 means that there is no relaxation of the structure and ions remain in the same place.

In order to have a wider selection of k-points, that additionally is located along the high-symmetry directions, the python-package sumo-kgen [36] is used to generate a new KPOINTS-file. The calculations is then run again with the newly generated KPOINTS-file.

Because all structures in this project are on the form $ABTe_2$, and Te is a heavy element, spin-orbit coupling (soc) contributions should be included in the calculations. In order to get information about how large this noncollinear contribution is, the DOS-calculations are all run both with and without spin-orbit coupling. In order to include spin-orbit coupling in the calculations the following INCAR-parameters are necessary:

- LSORBIT = TRUE
- ISYM=0
- ISPIN=2

This has to be run as a non-collinear calculation instead of the standard VASP calculation. VASP usually uses a memory conserving symmetrisation, but is in this case turned of with ISYM=0. LSORBIT=TRUE simply switches on spin-orbit coupling contributions, and with ISPIN=2 spin-polarized calculations are performed.

4.3.2 Optical DOS

To also get information about photon absorption, an optical DOS is calculated. The INCAR-file is changed to:

- NBANDS = 1024
- ISMEAR=-5
- LOPTICS = TRUE
- CSHIFT= 1E-6

ISMEAR=-5 means integrating over the Brillouin Zone by the tetrahedron method with Blöch corrections [37] instead of the earlier Gaussian smearing. Setting LOPTICS=TRUE initiates the calculation of the frequency dependent dielectric matrix after the electronic ground state has been determined. The CSHIFT parameter sets the complex shift in the function. As well know, the real part of dielectric function describes polarization and the imaginary one treats absorption. The latter is derived by the optical transitions between occupied and unoccupied bands.The number of bands, NBANDS, are doubled in order to get sufficient available empty conduction band states. LORBIT=TRUE only supports a Γ-centered KPOINTS-file, and so these calculations were performed using the old KPOINTS-files from Råheim's project, corresponding to a k-point density of at least 0.2332 according to a k-point convergence test. The rest of the input parameters remained the same as in the previous calculation, which means that spin-orbit contributions is still accounted for.

The python package sumo [36] was then used for further data processing and visualization. The effective masses for electrons and holes were calculated by sumo using a parabolic fitting from the band edge extrema to the nearest high symmetry points. This leads to effective masses in up to three different directions depending on the symmetry of the lattice and the positioning of the VBM and CBM. A joint representative effective mass was obtained by calculating the harmonic average of the values from the different directions. All numerical values for the effective mass calculations can be found in Appendix C. The orbital contribution for the DOS at the band edge extrema were calculated using a python-script using the BSVasprun package from pymatgen [38]. The table for these contributions can be found in Appendix D. All structural visualization is done with the 3D visualization software `VESTA` [39].

In order to obtain the candidates with the best electronic performance a lower threshold of $E_g < 1.2eV$ was applied, as well as $m^* < 0.6m_0$ for the effective masses of both electrons and holes. The effective masses is always given as a fraction of the electron mass, m_0.

4.3.3 Phonon dispersion relations

For the candidates passing the electronic structure criteria, phonon dispersion relations were calculated in order to determine dynamic stability. They were calculated using the Frozen-Phonon method, which consists of two steps. The lattice dynamics theory from Section 3.4 refers to energy minimized lattices

with no forces or stresses between the atoms that are placed at their equilibrium positions. Stricter relaxation criteria are therefore necessary to realize this and so the first step is therefore a tight relaxation.

The tight relaxation input files were based on the relaxed structures from Råheim's project, with the following changes in the INCAR-file:

- EDIFF = 1e-8
- EDIFFG = -0.001
- ADDGRID = .TRUE.
- PREC = Accurate
- LREAL = .FALSE.

EDIFF sets the global break condiction for the electronic self-consistency steps, meaning that the iteration is stopped if the total free energy change and the band structure energy change between two steps are smaller than EDIFF. The EDIFFG parameter decides whether the relaxation is stopped if the norms of all the forces are smaller than |EDIFFG|. PREC=ACCURATE together with ADDGRID=TRUE is necessary to increase the precision of the relaxation. LREAL=FALSE means that the projection is done in reciprocal space, leading to more precise results. After each run, the POSCAR was updated with the CONTCAR and NSW was increased with 10 until the calculations reached required accuracy.

The second step of the Frozen-Phonon method refers to the finite displacement calculations. They were prepared using the *phonopy* [40] python package. The idea is to generate a more or less cubic supercells with finite atomic displacements, based on the tight relaxed structure. The amount of generated supercells and the displacements of the atoms are inherently decided by the symmetry of the crystal. In order for the supercell to be sufficiently large, the tight relaxed structure is multiplied with an integer such that each lattice parameter exceeds 10Å. If the cell is larger, the calculations can have problems with running due to a large memory demand, while for smaller cells the finite displacement will have a too large contribution to the atomic forces of the system. The dimension multiplier used to generate the supercells are tabulated in Table 4.3. Each supercell involves one displaced atom leading to multiple force constant calculations. After the calculations have finished phonopy code is used again to create a FORCE_SETS-file containing information about all the atomic forces for each supercell. Sumo plotting is then used to plot the phonon dispersion diagrams based on the sets of atomic forces gathered from the finite differences calculations.

Table 4.3: Dimensions of the generated supercells by space group and how many atoms are in original cell

Space group	Nsites	Dimension [a x b x c]
$C2/c$	8	2 x 3 x 2
$C2/c$	32	3 x 3 x 1
$I\bar{4}2d$	8	4 x 4 x 2
$I\bar{4}2d$	16	2 x 2 x 1
$I4/mcm$	8	3 x 3 x 4
$Pna2_1$	16	2 x 2 x 2

5 Results

In the following section the most important results regarding the electronic screening, electronic properties, optical properties and lattice dynamics will be presented. A more in-depth and analytical view of the results will follow in the Discussion section (6).

5.1 Electronic screening

The fundamental band gap correspond to the numerical difference in energy between the VBM and CBM. In Fig 5.1 the fundamental band gaps of each of the structures are plotted against both A and B cation. They are additionally separated in terms of space groups through labels. The black dotted line at E_g = 1.2 eV correspond to the threshold value for which structures below this value is screened out.

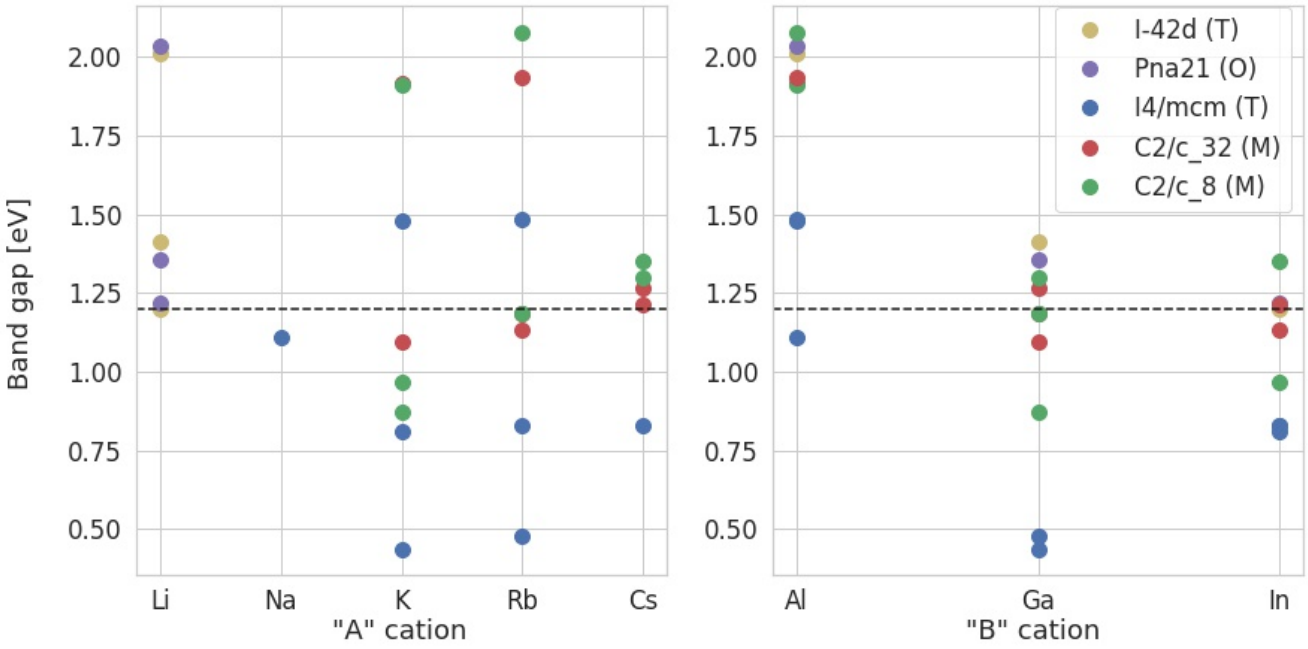

Figure 5.1: Fundamental band gap values plotted both vs its A and B cation. The colour separation is done according to each space group with T-tetragonal, O-orthorombic and M-monoclinic.

From Fig 5.1 it is easily realizable that it is the B cation that has the most influence on the electronic structure. Looking at the plot for the A cations show a high spread of the band gap values for each cation, meaning that it is probable that there is no direct correlation between A cation and band gap. One can argue that the Li values are larger than the others, but this can be explained by the space groups $Pna2_1$ and $I\bar{4}2d$ only being prevalent for the Li. In addition the Cs values might seem more localized than the others, but that stems from the fact that $CsAlTe_2$ did not have any thermodynamically stable phases such that the Cs values only are comprised of $CsGaTe_2$ and $CsInTe_2$. Now for the B cation there is a clear correlation between the band gap and cation. The plot also shows how much the space group, and thereby also the coordination of ions, can affect the band gap. The electronic structure also depend on the spatial structure of the lattices. This is analyzed further in Fig 5.2 where the band gap is plotted vs.

lattice parameters a and c for the $C2/c_8$, $I4/mcm$ and $C2/c_{32}$ space groups. The $I\bar{4}2d$ and $Pna2_1$ are not a part of these plots as it is only the Li compounds that exhibit this kind of symmetry.

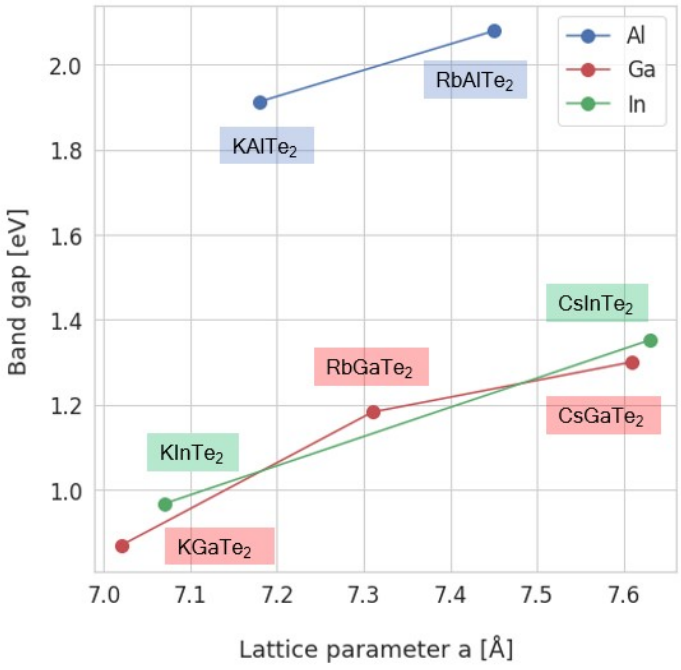

(a) $C2/c_8$

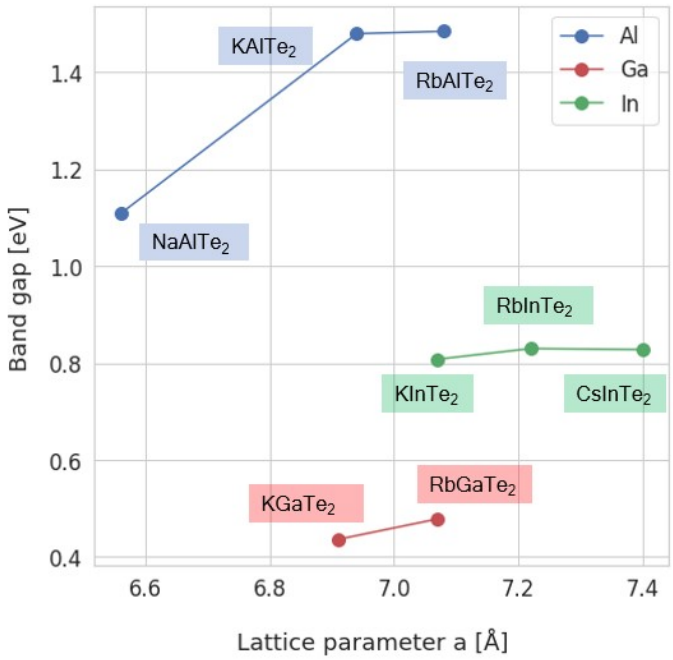

(b) $I4/mcm$

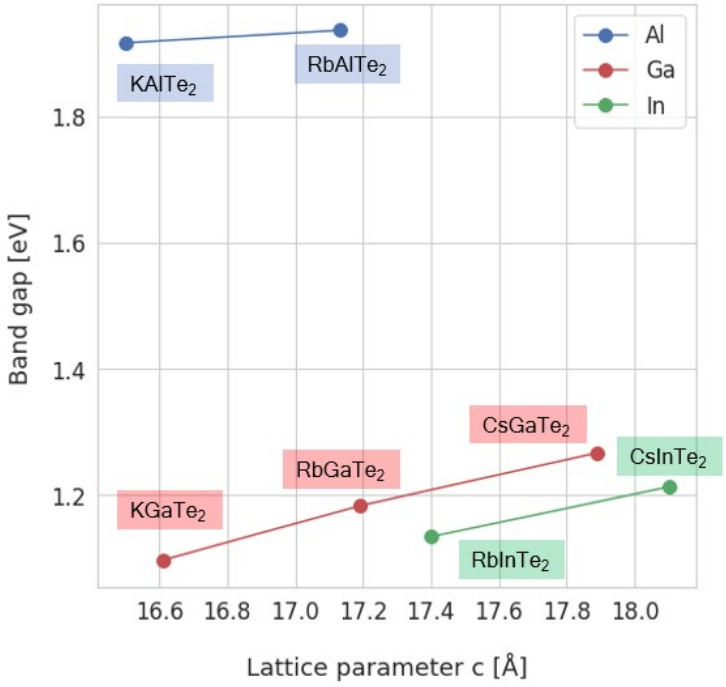

(c) $C2/c_{32}$

Figure 5.2: Band gaps plotted as a function of lattice parameter a for the $C2/c_8$ and $14/mcm$ structures and c parameter for the $C2/c_{32}$ structures.

The electronic screening is continued with calculations of effective masses. The full list of all effective masses in all directions can be found in Appendix C. The structures already passing the band gap criteria of $E_g > 1.2$ eV is plotted in Fig 5.3. The green shaded area correspond to $m_h^* < 0.6 \bigcup m_e^* < 0.6$.

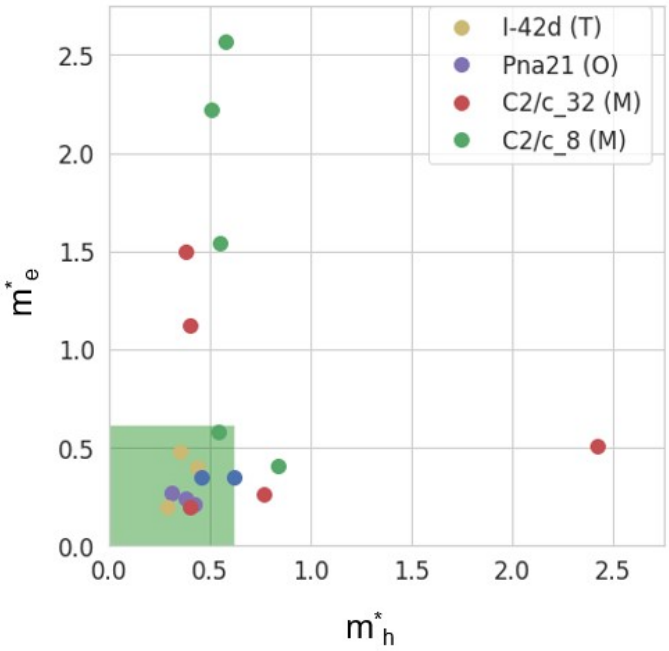

Figure 5.3: Effective masses of both holes and electrons for the structures with $E_g > 1.2$ eV. The structures inside the green shaded area passes the effective mass screening criteria.

Applying both of our screening criteria to all of the structures leaves us with the candidates in Table 5.1. As a small indirect band gap also is preferred a ΔE_g is also calculated. This correspond to the difference in energies between the direct (E_g^{dir}) and indirect (E_g^{ind}) band gaps: $\Delta E_g = E_g^{dir} - E_g^{ind}$.

Table 5.1: Candidates passing the electronic structure criteria. The effective masses are given as fractions of the electron mass, m_0. ΔE_g relates to the difference between the indirect and direct band gap. If this value is zero, the band gap is direct.

Composition	Space group	$E_g[eV]$	m_e^*	m_h^*	ΔE_g
$LiAlTe_2$	$Pna2_1$	2.03	0.24	0.38	0.22
$LiAlTe_2$	$I\bar{4}2d$	2.01	0.40	0.44	0
$LiGaTe_2$	$Pna2_1$	1.35	0.27	0.31	0.11
$LiGaTe_2$	$I\bar{4}2d$	1.41	0.48	0.35	0.07
$LiInTe_2$	$Pna2_1$	1.22	0.21	0.42	0
$LiInTe_2$	$I\bar{4}2d$	1.20	0.20	0.29	0
$KAlTe_2$	$I4/mcm$	1.48	0.35	0.62	0.22
$RbAlTe_2$	$I4/mcm$	1.49	0.35	0.46	0.37
$CsGaTe_2$	$C2/c_8$	1.30	0.58	0.54	0.21
$CsInTe_2$	$C2/c_{32}$	1.21	0.20	0.40	0

The rest of the result section will mainly focus on a more deeper analysis for the candidates already pass-

ing this electronic screening.

5.2 Band structures

Spin orbit coupling band diagrams for compounds representing all of the space groups are provided in the two following Fig 5.4 and 5.5. The energies of each band are by convention plotted along the high symmetry directions with the VBM set to zero.The space group symmetry heavily influences the shape of the band diagrams and determines the high symmetry directions for which the bands are plotted. The number of atoms in the cell will also influence the band structures and larger structures having a greater amount of available bands. The rest of the band diagrams (both with and without spin-orbit coupling) can be found in appendix E.

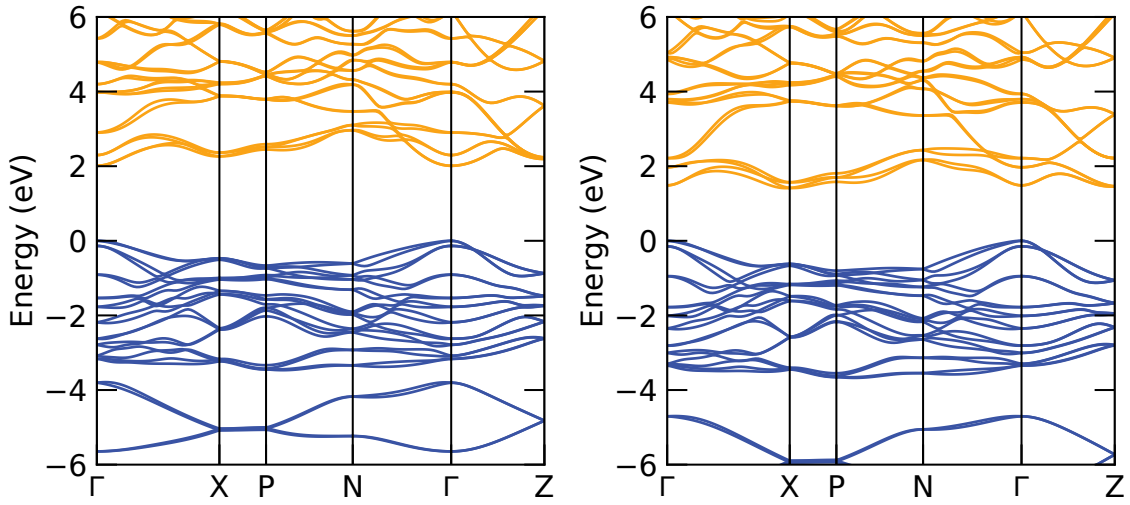

(a) $LiAlTe_2$ $I\bar{4}2d$ **(b)** $LiGaTe_2$ $I\bar{4}2d$

Figure 5.4: PBEsol+soc band diagrams

The two presented band diagrams in 5.4 represent two different compounds with the same space group. The symmetry of the Brillouin Zone heavily influences the electronic structure, and therefore also the band diagrams. Consequently, the VBM and CBM often are located at the same point in the Brillouin Zone for two compounds with similar space groups. This is, however, not the case in this example. For $LiAlTe_2$ the band gap correspond to a direct transition with both the VBM and CBM located at the Γ-point. For $LiGaTe_2$ the VBM is still located at the Γ-point, but the CBM is located in the space between Γ and X.

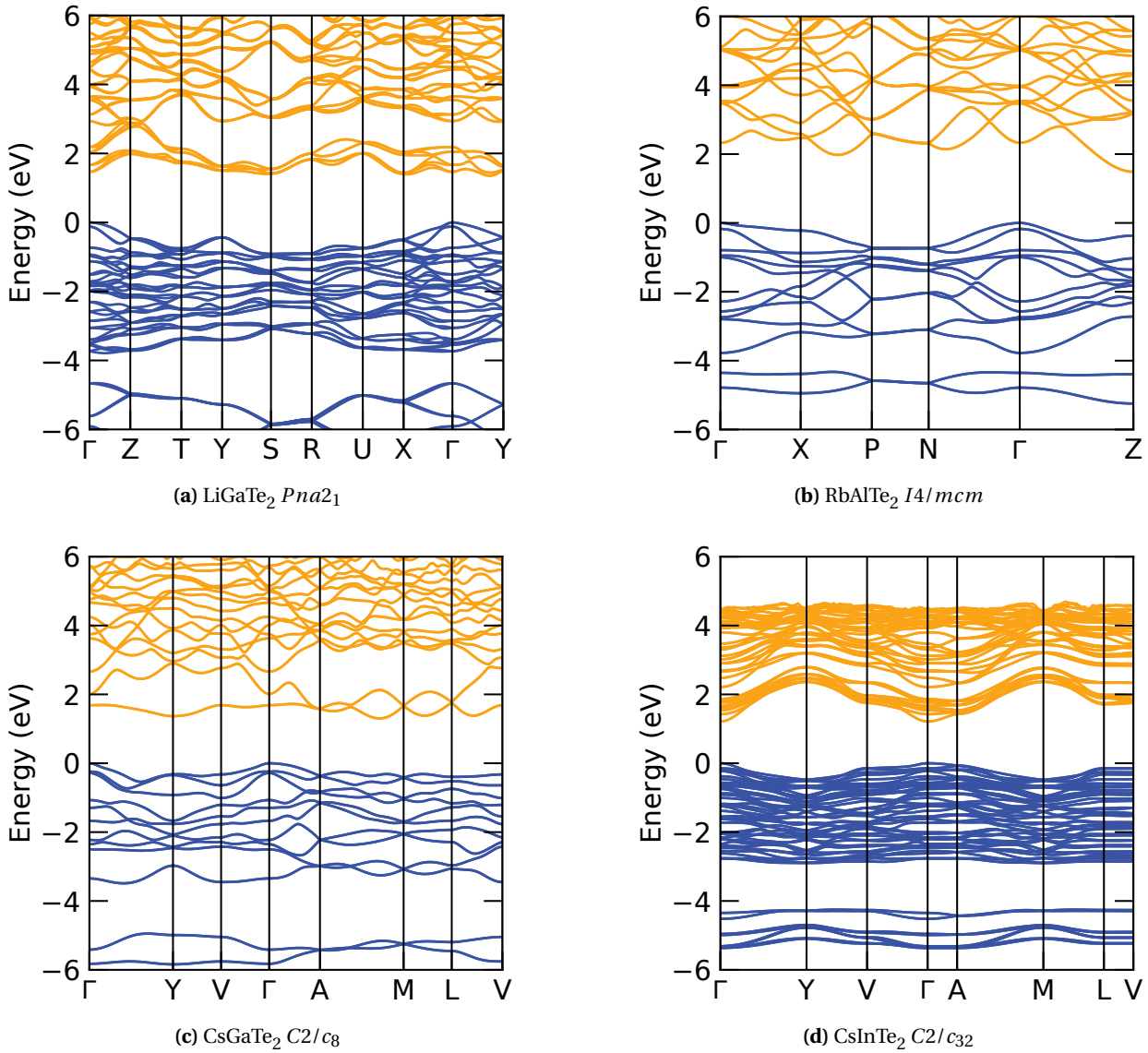

(a) $LiGaTe_2$ $Pna2_1$

(b) $RbAlTe_2$ $I4/mcm$

(c) $CsGaTe_2$ $C2/c_8$

(d) $CsInTe_2$ $C2/c_{32}$

Figure 5.5: PBEsol+soc band diagrams

The band diagrams presented in Fig 5.5 show examples of band structures for compounds with different structures. Because they are subgroups of different Bravais lattices, the high symmetry directions the bands are plotted in differ from each other. However, both (**c**) and(**d**) have the same monoclinic space group symmetry and therefore also the same high symmetry directions. The band gaps at (**a**), (**b**) and (**c**) are all indirect, while for (**d**) it is direct. They all have VBM located at the Γ-point while the CBM varies. Worth noting is also the highly indirect nature of the band gap for the space group $I4/mcm$ in (**b**).

5.3 Density of states (DOS)

The density of states correspond to the allowed energy levels for the electrons in the structure as explained in Section 3.1. Elemental resolved DOS-plots are provided in Fig 5.6 and 5.7 The rest of the calculated plots can be found in Appendix H. Similarily to the band diagrams, the energy of the VBM is also in this case chosen as E=0, meaning that the states with a negative energy value represent the valence band and the positive energy states represent the conduction band, with the band gap separating them. The y-axis correspond to an arbitrary unit representing the number of available electron states. The A cations are left out of the plots, due to their low contribution to the electronic structure. Te p states is clearly the most prevalent phase in all valence bands, while the conduction band close to the band gap have both a B s and Te p character. The best case scenario involves sharp-rising peaks at band edge values, but still with sufficient available states at higher energies.

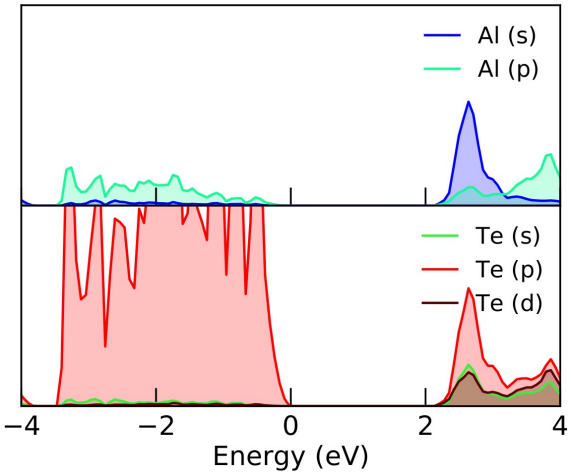

(a) $LiAlTe_2$ $I\bar{4}2d$

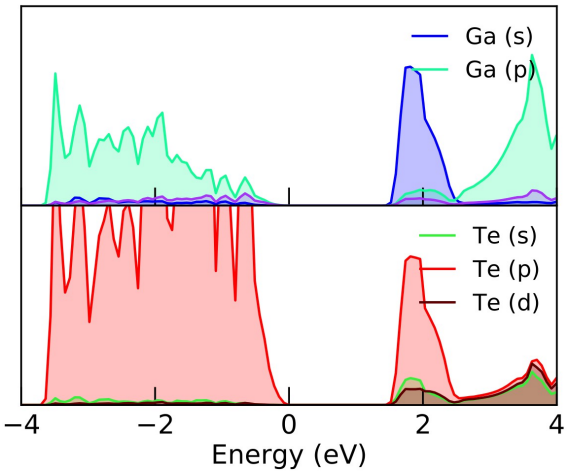

(b) $LiGaTe_2$ $I\bar{4}2d$

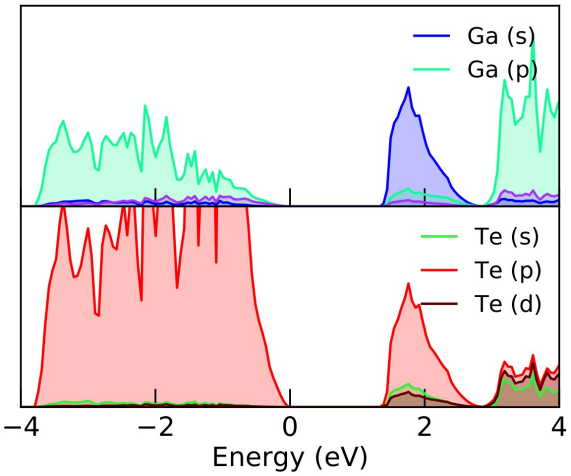

(c) $LiGaTe_2$ $Pna2_1$

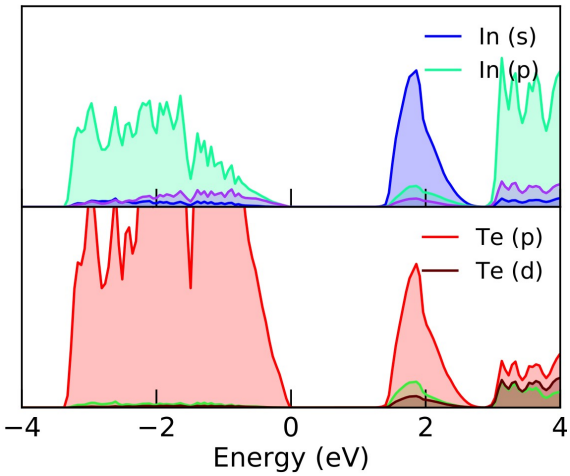

(d) $LiInTe_2$ $Pna2_1$

Figure 5.6: Elemental DOS-plots for different compounds. (**a**) and (**b**) have a similar structure, but the first peak in the conduction band has a different character. In (**a**) the peak is further away from the band edge, which might indicate lower absorption. The conduction band peaks in (**c**) and (**d**) have more similar shapes and it is therefore expected that these have a more similar absorption close to the band gap value.

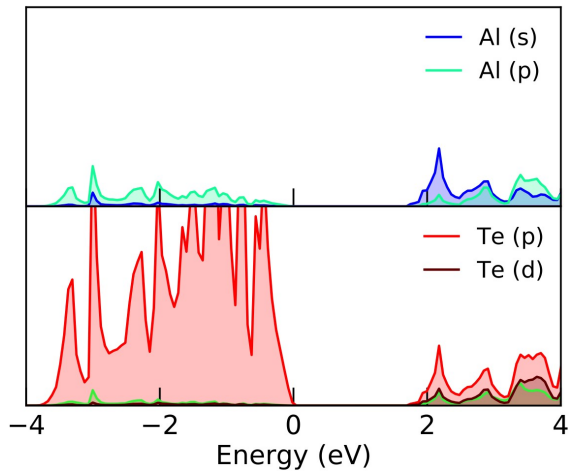

(a) $I4/mcm$ $KAlTe_2$

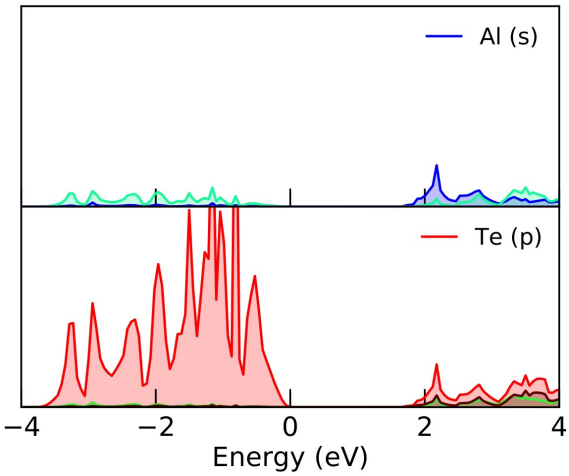

(b) $I4/mcm$ $RbAlTe_2$

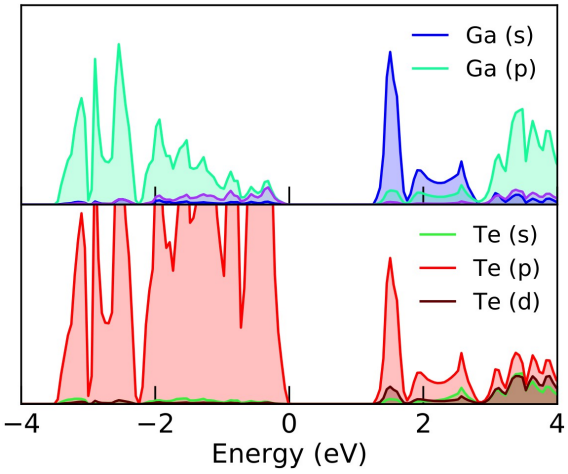

(c) $CsGaTe_2$ $C2/c_8$

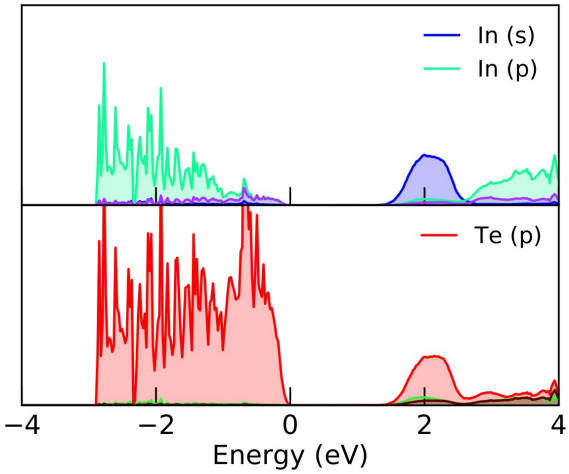

(d) $CsInTe_2$ $C2/c_{32}$

Figure 5.7: DOS for other passing candidates. (**a**) and (**b**) both have the $I4/mcm$ space group and have few available states in the conduction band, which might indicate bad absorption. In (**c**) there is a peak close to the CBM, but the sharp descent to almost zero might indicate a good absorption for photons with energy close to the band gap, but not so much for higher energy photons. In (**d**) all of the intensities are small compared to the other plots, but bear in mind that these plots are only representing arbitrary units, and so the relative intensities is what is important.

5.4 Optical absorption

Absorption coefficients α are plotted as a function of incident photon energies in Fig 5.8 and 5.9. The vertical dotted line correspond to the direct band gap of the compound. This is done because VASP only considers direct band-to-band transitions in its calculations. Good absorption can be thought of as a small area between the plotted absorption coefficient and the dotted band gap line. This implies that absorption should start already close to the band gap line.

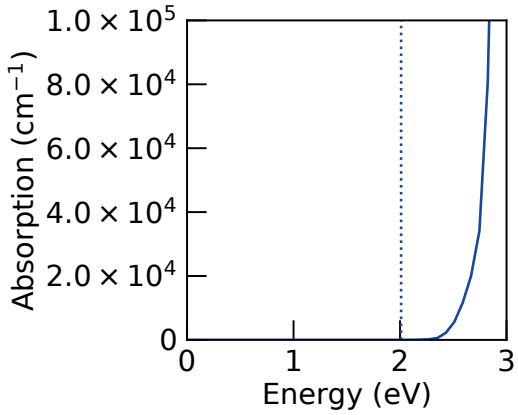

(a) LiAlTe$_2$ $I\bar{4}2d$

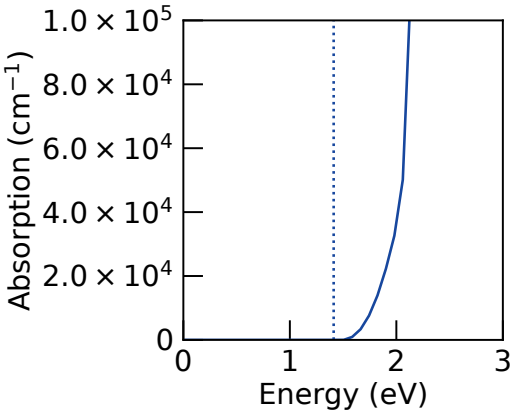

(b) LiGaTe$_2$ $I\bar{4}2d$

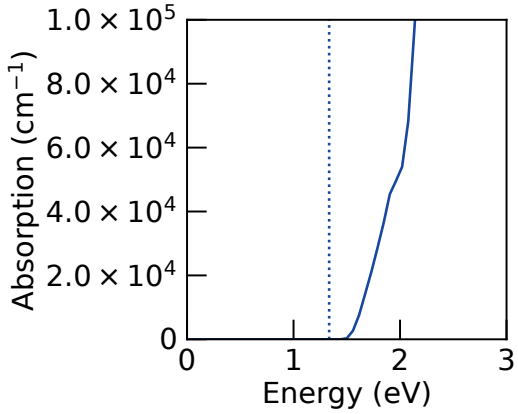

(c) LiGaTe$_2$ $Pna2_1$

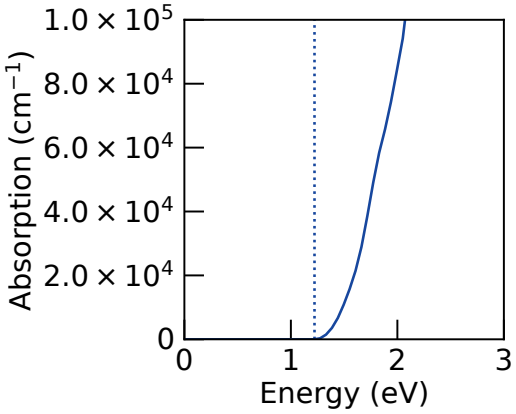

(d) LiInTe$_2$ $Pna2_1$

Figure 5.8: Absorption plots for compounds with space group $I\bar{4}2d$ and $Pna2_1$. As expected from the DOS in Fig 5.6, $I\bar{4}2d$ LiAlTe$_2$ has a small onset from the band gap to absorption start. The rest of the compounds, however, show great absorption.

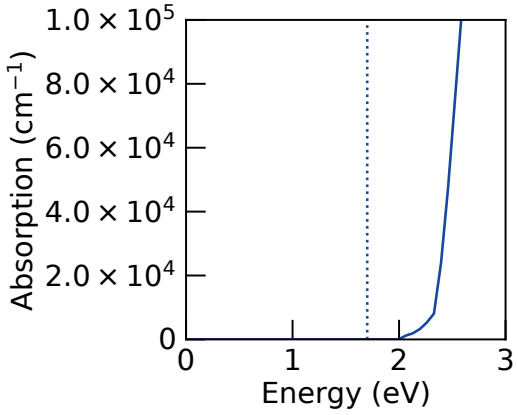

(a) $I4/mcm$ $KAlTe_2$

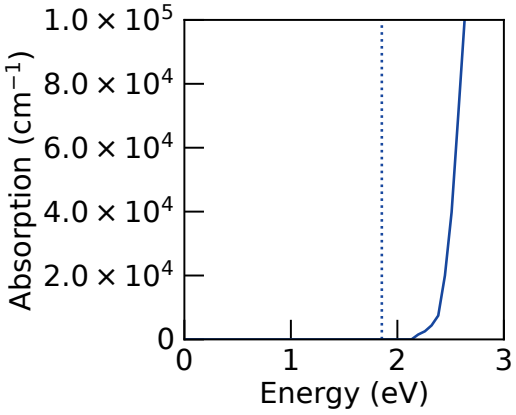

(b) $I4/mcm$ $RbAlTe_2$

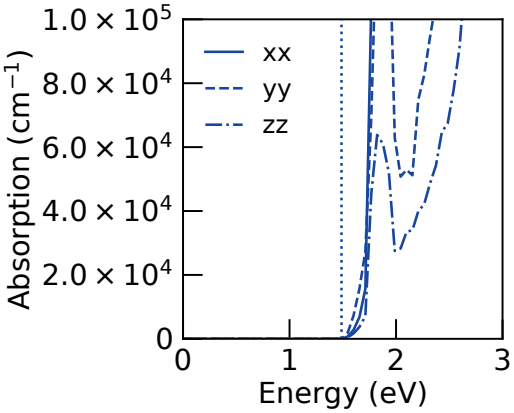

(c) $CsGaTe_2$ $C2/c_8$

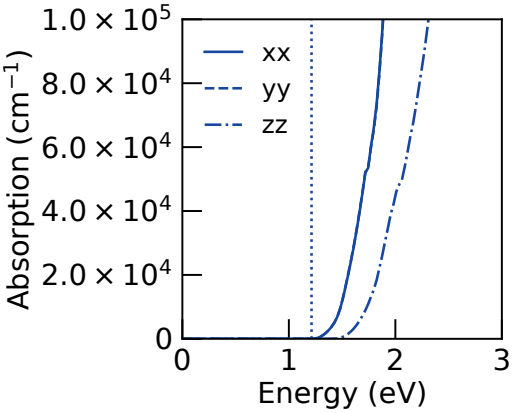

(d) $CsInTe_2$ $C2/c_{32}$

Figure 5.9: Absorption plots for candidates with space groups $I4/mcm$ and $C2/c$. As expected from DOS-plots in Fig 5.7 the two $I4/mcm$ compounds in (**a**) and (**b**) have a low absorption close to band edges. The two monoclinic cells in (**c**) and (**d**) both showed anisotropic nature and so they were plotted with the different contributions in different directions. In (**c**) there is a dip for both y and z directions at around 2 eV, which can also be found in the DOS-plot in Fig 5.7. In the larger monoclinic cell in (**d**), there is a more uniform anisotropy with general worse absorption in the z-direction.

5.5 Lattice dynamics

Phonon dispersion diagrams have been plotted in order to determine the dynamic stability of the systems. Remembering from Section 3.4 that negative frequencies in general is not a good sign for structure stability. Negative modes at the Γ-point indicates that the structure is not at ground state energy and that there exists a lower energy phase. In the following figure the phonon dispersion diagrams for two different space groups of $LiInTe_2$ are shown.

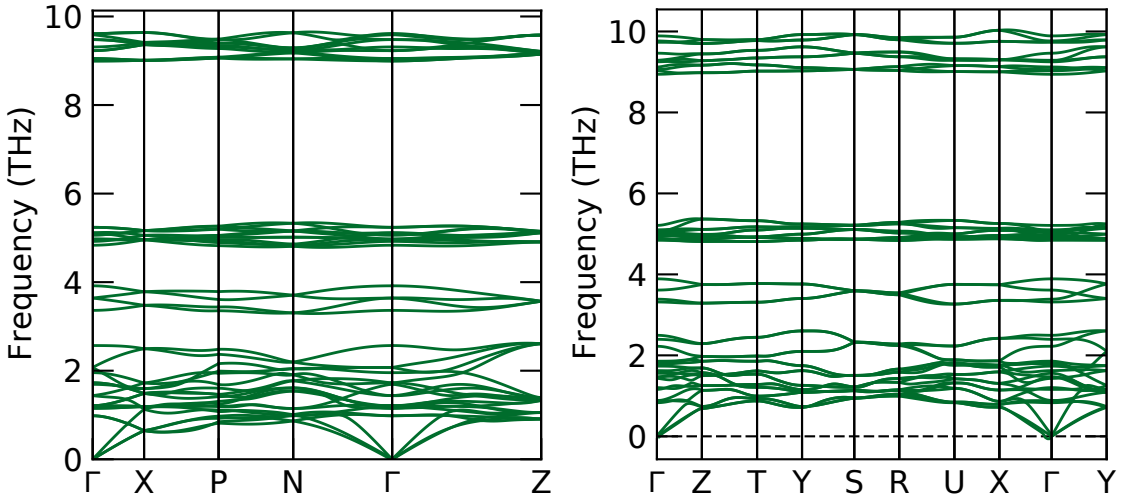

(a) $I\bar{4}2d$ **(b)** $Pna2_1$

Figure 5.10: Phonon dispersion diagram of $LiInTe_2$ with the space groups $I\bar{4}2d$ (a) and $Pna2_1$ (b)

It is clear that the tetragonal $I\bar{4}2d$ phase does not have any instability modes and therefore will be dynamically stable. However, For the orthorombic $Pna2_1$ phase there seem to be a very small negative frequency close to the Γ-point. Nevertheless, the contribution from this subtly negative mode is likely to be small enough to be neglected.

Further on, phonon dispersion relations for two different space groups of $CsInTe_2$ are presented in Fig 5.11. For the monoclinic $C2/c_8$ structure there is a clear negative frequency between the Γ-point and A. Interpreting the consequence of the negative frequencies that are not located at the Γ-point is not straight-forward. Nonetheless one can say that the tetragonal $I4/mcm$ is at least more dynamically stable than the monoclinic $C2/c_8$, but that it might be stable at room temperature.

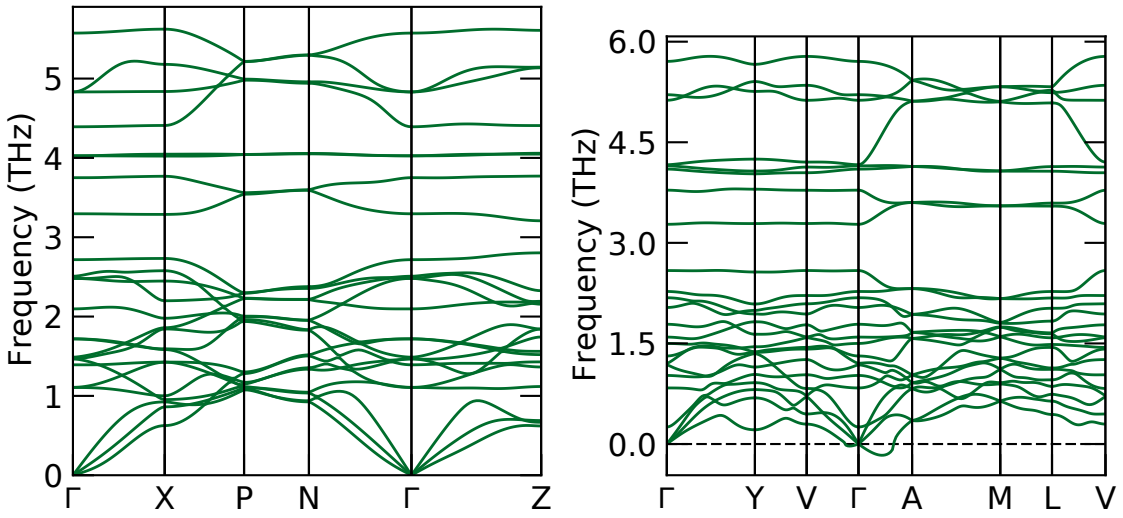

(a) $I4/mcm$ **(b)** $C2/c_8$

Figure 5.11: Phonon dispersion diagram of $CsInTe_2$ with the space groups (a) $I4/mcm$ and (b) $C2/c_8$

In the case of $RbGaTe_2$ in Fig 5.12 there is a clear negative mode located at the Γ-point. The structure is therefore deemed dynamically unstable.

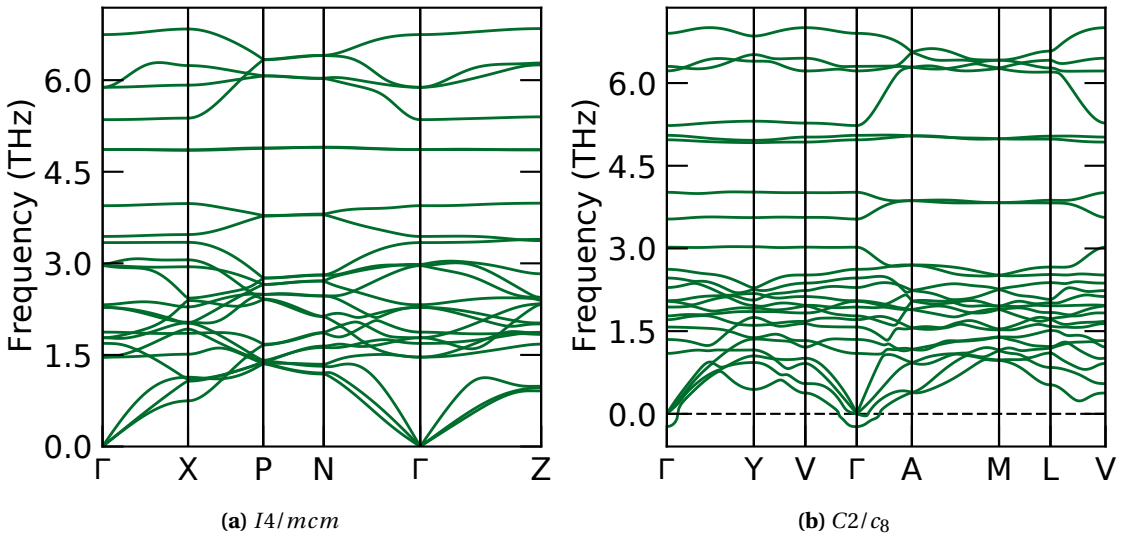

(a) $I4/mcm$ **(b)** $C2/c_8$

Figure 5.12: Phonon dispersion diagram of $RbGaTe_2$ with the space groups (a) $I4/mcm$ and (b) $C2/c_8$

The results for the dynamic stability analysis regarding the compounds passing the electronic screening has been summarized in Table 5.2. The dynamic stability for $C2/c_{32}$ $CsInTe_2$ is unknown as it has not yet been completed. The rest of the calculated phonon dispersion diagrams can be found in Appendix G.

Table 5.2: Results regarding the dynamic stability analysis for the structures passing the electronic screening

Composition	Space group	Dynamically stable
$LiAlTe_2$	$Pna2_1$	Yes
$LiAlTe_2$	$I\bar{4}2d$	Yes
$LiGaTe_2$	$Pna2_1$	Yes
$LiGaTe_2$	$I\bar{4}2d$	Yes
$LiInTe_2$	$Pna2_1$	Yes
$LiInTe_2$	$I\bar{4}2d$	Yes
$KAlTe_2$	$I4/mcm$	Yes
$RbAlTe_2$	$I4/mcm$	Yes
$CsGaTe_2$	$C2/c_8$	Yes
$CsInTe_2$	$C2/c_{32}$	Unknown

6 Discussion

Understanding how the fundamental electronic band gap changes depending on different parameters is an important step in future designs of telluride materials for all types of optoelectronic devices. The already presented plot in Fig 5.1 shows how the band gap changes for the different types of both A and B cation. It has already been discussed that it is the B cation that has the largest contribution to the band gap while the A cation only has a subtle and indirect contribution through changing the lattice parameter. Going down the periodic table for the alkali metal A cations the atomic radii increases, which of course happens due to the larger spatial extent of the higher-order orbitals. One can see from Fig 5.2 that increasing atomic number Z for the A cation also increases the lattice spacing as anticipated. For the B cations, however, the same trend is not observed. In general, following the points with similar A cation in (**b**) and (**c**), the compounds have a similar lattice constants for the Al and Ga compounds with a subtle increase for the In compounds. In (**a**), however, $KAlTe_2$ has a larger lattice constant than both $KGaTe_2$ and $KInTe_2$.

A periodic trend for the band gap is also expected for the group-III B cations. In general electrons in higher order orbitals are easier to polarize to due the lower effective nucleus charge. It is clear from both 5.1 and 5.2 that the Al compounds has larger band gaps than the compounds containing Ga and In, but for the latter, the band gap values are pretty similar. For the $I4/mcm$ space group Ga compounds even have the lowest band gaps with a subtle increase to In.

There have not been completed much research regarding ternary tellurides, especially with similar compositions as in this project. Most research mainly focus on oxides or different forms of chalcogenides with Se and S instead of Te. However, a study of ternary chalcopyrites (space group $I\bar{4}2d$) report literature values for similar systems with Cu as A-cation that has been tabulated in Table 6.1. From the table it is clear that the band gap difference between the $CuGaSe_2$ and $CuInSe_2$ is sufficiently larger than the band gap difference between $CuGaTe_2$ and $CuInTe_2$. This might indicate that the interactions between Te p states and Ga s or In s states is more similar than the interactions between Se p states and Ga s or In s, justifying the results found in this project.

Table 6.1: Literature values for other compounds with the $I\bar{4}2d$ structure. These values are included to showcase the band gap values for $MGaTe_2$ and $MInTe_2$ are much closer in value than $MGaSe_2$ and $MInSe_2$.

Compound	Band gap [eV] [41]
$CuAlSe_2$	2.70
$CuGaSe_2$	1.70
$CuInSe_2$	1.04
$CuAlTe_2$	2.06
$CuGaTe_2$	1.00
$CuInTe_2$	0.95

6.1 Screening

The most important parameter regarding the band gap is as already discussed to be the B cation. No compounds were screened out due to a too large band gap and there were not found any general trends tying the B cation to the effective masses. Consequently, Al, with the largest band gap, seem to be the best B cation on these premises. The best space group is harder to determine, and so a more thorough analysis of the advantages and disadvantages of each space group will follow.

6.1.1 Space group $I\bar{4}2d$

All of the three $I\bar{4}2d$ compounds from the beginning of the project also made it to the screening process. The $I\bar{4}2d$ structure is often called the chalcopyrite structure and can be seen visualized with `VESTA` in Fig 6.1. It is mostly the B-Te interactions which are of interest and therefore why only these bonds are displayed. The structure consists of evenly distributed [BTe_4] corner-sharing tetrahedra. The compounds are characterized by overall favourable band gaps and good charge conduction in all directions, with $LiInTe_2$ having some of the lowest effective mass values of all candidates (and therefore also best charge carrier conduction) with $m_e^* = 0.20$ and $m_h^* = 0.29$. In general this means that the orbital overlap between B s states and Te p states is good in all spatial directions and favours the delocalization of charge carriers.

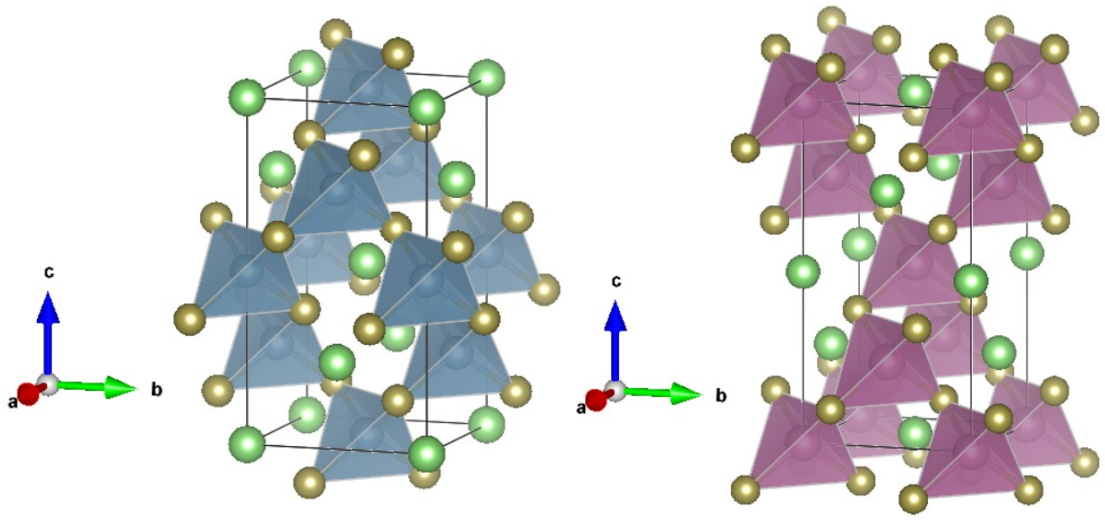

(a) $LiAlTe_2$ **(b)** $LiInTe_2$

Figure 6.1: Visual representations of the conventional cell for $LiAlTe_2$ and $LiInTe_2$ with spacegroup $I\bar{4}2d$ through `VESTA`. Both compounds are characterized by $[BTe_4]^{5-}$ corner-sharing tetrahedra. They might appear different from each other, but that is just because the A and B cations have swapped positions.

The two structures in Fig 6.1 has a different appearance, but is essentially the same. The difference stems from the inital thermodynamic screening done by Råheim [1], where the generated $I\bar{4}2d$ $LiInTe_2$ did not pass the screening, while the already existing MP candidate did. This means that both $LiAlTe_2$ and $LiGaTe_2$ originate from the primitive structure for $KInSe_2$ found in the MP database (as explained in Table 4.1), while the $LiInTe_2$ was downloaded directly from the database. The reason why the generated $LiInTe_2$ was screened out is likely due to the large elongation in c-direction that happened during the thermodynamic relaxation. For the lattice parameters of the conventional cell of the $KInSe_2$ the a/c-ratio is 0.77, while for $LiInTe_2$ it is 0.51. $LiAlTe_2$ has a ratio of 0.54 which is at least closer to the $KInSe_2$ value. This all seems to have a little impact on the final structural results, as the relaxed $LiAlTe_2$ and $LiInTe_2$ compounds from Fig 6.1 looks very similar. The $LiInTe_2$ POSCAR-cell that the calculations was run on was the conventional cell, rather than the primitive cell. This affects the appearance of the band diagrams, but is not expected to actually affect the electronic structure of the material.

It is also worth mentioning that chalcopyritic solar cells have been of great interest in the later years, mainly through thin film Cu(In,Ga)Se_2 (CIGS) solar cells. The band gap in these materials is tuned by the In/Ga ratio and they are characterized by very high absorption coefficients [42]. However, commercialization has been hampered by low yields and high cost production.

6.1.2 Space group $Pna2_1$

All of the compounds in the space group $Pna21$ passed the screening as well. This means that also this space group is characterized by favourable band gaps and good charge carrier conduction. The $Pna2_1$ DOS-plots in Fig 5.6 have fast-rising peaks close to the CBM, which indicates that there are many available electron states at similar energies already close to the band gap. This is of course favourable, as it indicates high absorption rates close to band gap values, but it might also indicate flat bands. However, the $Pna2_1$ band diagram in in (**a**) in Fig 5.5 is characterized by many small peaks and valleys. This results in many available states with similar energies, while still having good charge carrier conduction. The structure is visualized in Fig 6.2. Despite being an orthorhombic cell with different a, b and c lattice parameters, there is no emerging anisotropic trend. This is likely due to the well distributed [BTe_4] tetrahedra with alternating orientations.

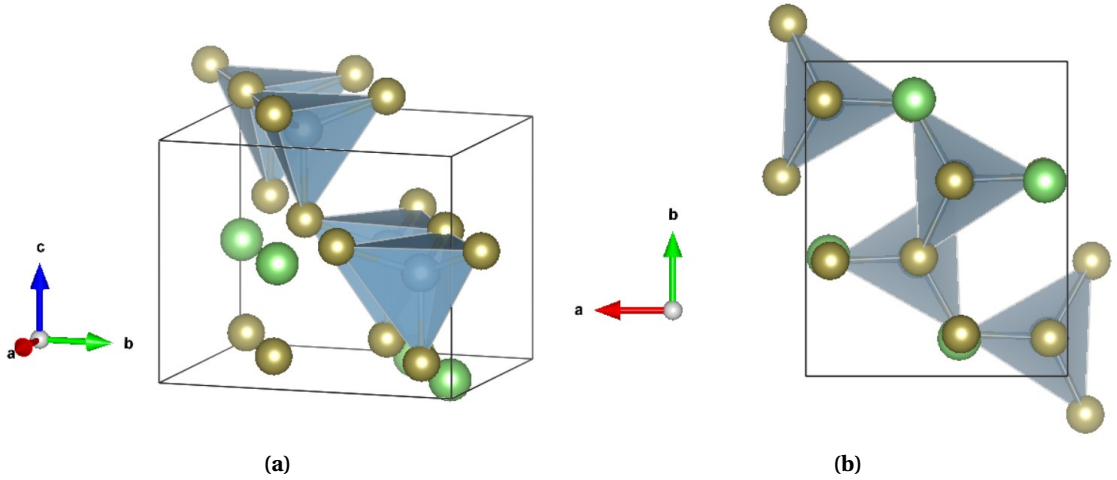

(a) **(b)**

Figure 6.2: Conventional cell for $Pna2_1$ $LiAlTe_2$. (**a**) shows the corner-sharing $[AlTe_4]^{5-}$ tetrahedra and (**b**) the rotation of said tetrahedra in the ab plane.

6.1.3 Space group $I4/mcm$

For the compounds with space group $I4/mcm$, only 2/8 compounds passed the electronic screening. The band diagrams in (**b**) from Fig 5.5 as well as E.3 in Appendix E show a characteristic deep valley in the conduction band at the Z-point. The two compounds passing the screening, $KAlTe_2$ and $RbAlTe_2$, stands out as the two with smallest change between the direct and indirect band gap, relating to a more shallow Z-valley. Consequently, these are the only two compounds with large enough band gap to make it through are screening process. It is probable that the indirect absorption process for these kind of materials would be bad due to the single-band valley causing few absorption points close to the band gap value, as well as large thermalization losses for the higher energy electrons. On the other hand, these band structures have the advantage good charge carrier conduction, especially for the electrons in the conduction band.

The large dispersion of the bands between Γ and Z can be explained by structural visualization. The conventional structure is displayed in Fig 6.3. Brillouin Zone analysis with the help of Fig A.4 in Appendix A, makes it clear that the direction Γ →Z relates to the c-axis in the real space structure. The edge-sharing tetrahedron symmetry causes a shorter bond length between the two cations inside the tetrahedron com-

pared to the corner-sharing tetrahedral configuration. Consequently the Al s orbitals have a great overlap in the direction along the formed tetrahedra. From the DOS-plot in (**b**) from Fig 5.7, it is clear that the Al s orbitals mainly contributes to conduction band states and therefore this large orbital overlap is what causes the valley seen in the band diagrams at point Z. The close proximity of the cations also increases the cation-cation electrostatic repulsion, which decreases stability. As well known, this also lead to lower band gaps and can be seen as the reason for why the main screening conditions for these compounds were the low fundamental band gap values.

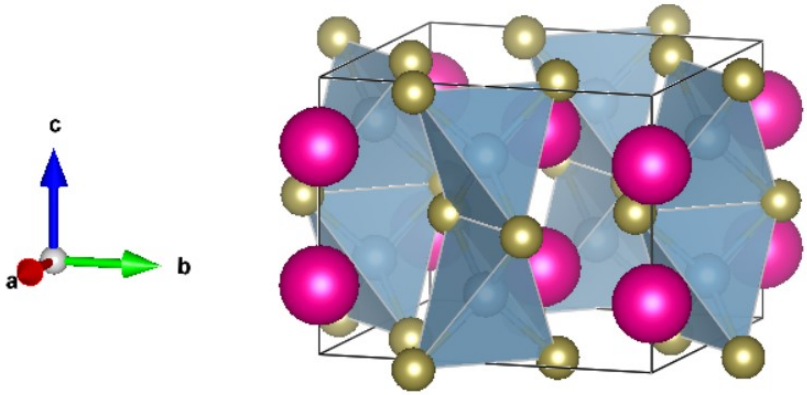

Figure 6.3: Generated conventional standard of the $I4/mcm$ $RbAlTe_2$ structure visualized through `VESTA`. $AlTe_4$ is here forming edge-sharing tetrahedra along the c-axis.

This spacegroup was also the only one were a clear trend tying lattice parameters to effective masses were observed. The electron mass is plotted vs. lattice parameter c in Fig 6.4. This can be due to the clear alignments of the tetrahedra in the c-direction directly influencing the orbital overlaps. Larger orbital overlap relates to more delocalized electrons and therefore lower effective masses. In other situations the exact bond-length or bond angles should be considered for a similar analysis. The two compounds surviving the screening are the two with the largest electron effective masses of $m_e^* = 0.35 m_0$.

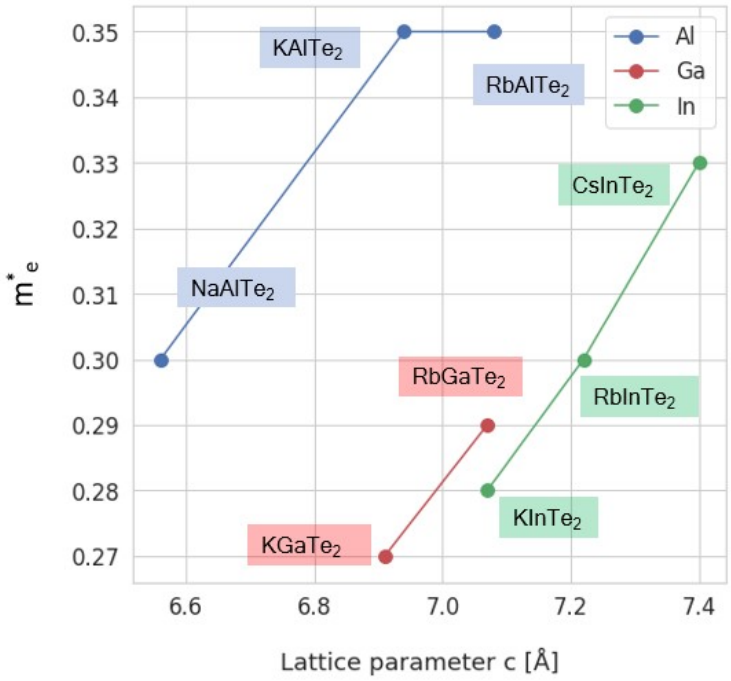

Figure 6.4: Electron effective mass vs. lattice parameter c for space group $I4/mcm$

6.1.4 Space group $C2/c_8$

For the $C2/c_8$ compounds only 1/7 compounds passed the electronic screening. Only three were screened out due to a low band gap and so the most strict screening criteria was in this case the effective masses. The surviving compound $CsGaTe_2$ has effective masses of $m_h^* = 0.58m_0$ and $m_e^* = 0.54m_0$ and barely makes it through the screen. Similarly to $Pna2_1$, the DOS-plots for the compounds with this structure is characterized by a large number of available states close to the band edge leading to great absorption close to the band edges, but in this case that also relates to flat bands in the electronic structure. In general it is the electron effective masses that stands the most out, but no apparent trend is spotted. Fig 6.5 shows a visualization of the structure which similar to $I4/mcm$ show edge-sharing $GaTe_4$ tetrahedra. However, this monoclinic cell is more more anisotropic with a $\neq$ b $\neq$ c and angle $\beta \neq 90°$. The anisotropy of the structure can be the cause of the seemingly random behaviour. The electron effective mass is expected to vary as a function of the interatomic distance between the two B ions in the edge-sharing tetrahedra. Trends show that increasing the size of the A cations leads to shorter interatomic distance between the B cations in the edge-sharing tetrahedra due to a changing of the β angle. However, this interatomic distance was unsuccessfully tied to electron effective mass.

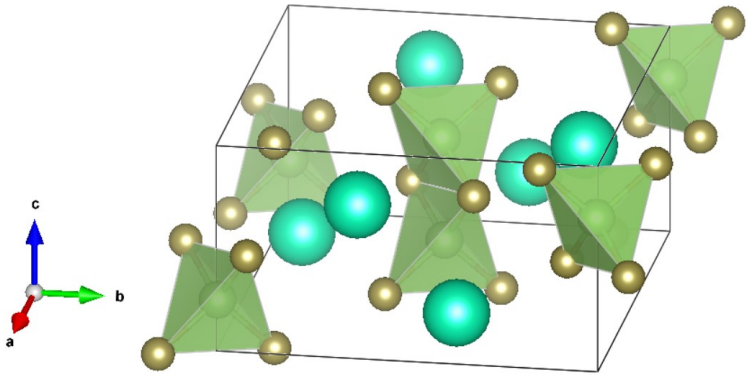

(a)

Figure 6.5: Generated conventional standard cell of $CsGaTe_2$ with space group $C2/8_c$. $GaTe_4$ form edge-sharing tetrahedron. As this is just a representation of a repeating unit, also the tetrahedra at the edges of the cell will together form similar edge-sharing tetrahedra.

6.1.5 Space group $C2/c_{32}$

For the compounds with the larger monoclinic cell, also here 1/7 makes it through the screening process. Out of the seven candidates, four have large enough band gaps, five has sufficiently low m_e^* and five has low enough m_h^*. The disadvantages for this structure is that it only displays direct band gaps, and that the charge carrier conduction in the $\Gamma \rightarrow A$ is extremely low for some of the compounds. For the calculations without spin-orbit coupling, both $RbAlTe_2$ and $RbGaTe_2$ reported infinitely large effective electron masses in the $\Gamma \rightarrow A$ direction. This happens as the parabolic fitting used to calculate the effective masses only resulted in a straight line. Nevertheless, the problem was not encountered when soc was included in the calculation, although the values were still high.

The structure for the screening survivor $CsInTe_2$ is vizualised with `VESTA` in 6.6. The structure consists of different layers with corner sharing $InTe_4$ tetrahedra which again form In_4Te_{10} prismatic clusters. The layers are stacked perpendicular to the c-axis and with a 90° rotation on the layer plain. Bonding between the layers happen between Cs and Te. A short Brillouin Zone analysis on the representation for the space group in Fig A.1 tells us that the Brillouin Zone direction $\Gamma \rightarrow A$ correspond to the c-axis, and so the interlayer between the alternating prismatic clusters can be seen as an explanation for this low charge carrier conduction.

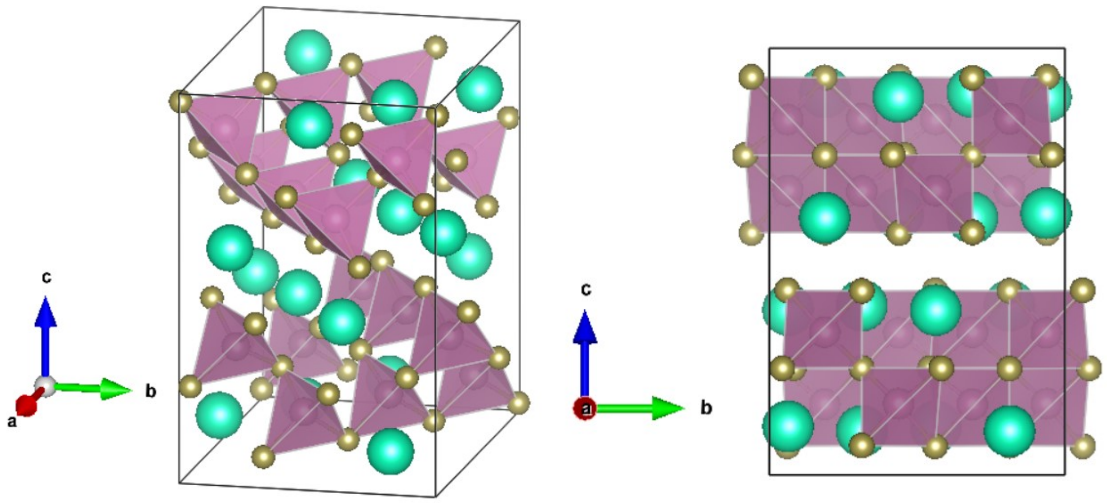

(a) **(b)**

Figure 6.6: Generated conventional structure of $C2/c_{32}$ $CsInTe_2$. Two different perspectives is included in order to both show the nature of the prismatic clusters formed by corner sharing $InTe_4$ tetrahedra in (**a**) as well as the layered nature of the structure in (**b**).

The reason why $CsInTe_2$ makes it through the screening process however can be due to the large spatial extent of both Cs and In, causing the interlayer distance to be smaller compared to the spatial size of the orbitals.

The screened out materials have a too bad bulk performance to make it through the screening process. However, due to their anisotropic nature, they can still have their uses as ordered thin-film materials with both good in-plane absorption and charge carrier conduction. Luckily, the band gaps for all these materials are direct, which therefore allows good absorption, even for thin film materials.

6.1.6 Space group summary

The two space group symmetries with the most promising features, $I\bar{4}2d$ and $Pna2_1$, are both characterized by evenly distributed corner-sharing [BTe_4] tetrahedra, leading to suitable band gaps and good charge carrier conduction in all directions. All compounds with these symmetries made it through the screening process. The edge-sharing tetrahedra found in tetragonal $I4/mcm$ and monoclinic $C2/c_8$, on the other hand, does not have as favourable properties. In $I4/mcm$ the close proximity of the B-cations in the edge-sharing tetrahedra lead to good electron conduction specifically along the c-axis, but also to too narrow band gaps. The small monoclinic phase, $C2/c_8$, is generally characterized by flat bands, indicating low charge carrier conduction all over. The larger monoclinic phase, $C2/c_{32}$, again displays corner sharing BTe_4-tetrahedra, but with a more layered structure. This leads to anisotropic behaviour and low charge conduction between the layers.

6.2 Optical absorption

Good absorption is characterized by fast increasing absorption coefficients already close to band gap values. In some cases the potential candidates show a small onset before full absorption starts, indicating that the optical band gap does not equal the direct band gap. This is expected to be caused by either

parity-forbidden transitions as explained in section 3.1.2, or due to few available states at the band edges. This is then also expected to show up in the DOS-plots.

The Table 6.2 addresses the differences between the vertical electronic band gap and the optical band gap. The optical band gap comes from visual interpretation of the starting point for the absorption plots in section 5.4. It is worth noticing that the optical DOS calculations were based on a Γ-centered mesh and so the sampling of the Brillouin Zone is not as good as for the calculations were the numerical values from the direct band gap comes from. The numerical values of E_{opt} is therefore only approximate values. The difference between the optical and electronic band gap is referred to as optical losses. The candidates with non-negligible optical losses is expected to show bad photocatalytic performance and will therefore not further be considered as potential candidates.

Table 6.2: Optical losses for the structures surviving the electronic screening. Optical losses refer to the difference between the optical and electronic band gap.

Composition	Space group	$E_g^{dir}[eV]$	$E_{opt}^{dir}[eV]$	Optical losses
$LiAlTe_2$	$Pna2_1$	2.3	2.3	0
$LiAlTe_2$	$I\bar{4}2d$	2.0	2.3	0.3
$LiGaTe_2$	$Pna2_1$	1.5	1.5	0
$LiGaTe_2$	$I\bar{4}2d$	1.5	1.5	0
$LiInTe_2$	$Pna2_1$	1.2	1.2	0
$LiInTe_2$	$I\bar{4}2d$	1.2	1.2	0
$KAlTe_2$	$I4/mcm$	1.7	2.0	0.3
$RbAlTe_2$	$I4/mcm$	1.9	2.1	0.2
$CsGaTe_2$	$C2/c_8$	1.6	1.6	0
$CsInTe_2$	$C2/c_{32}$	1.2	1.2	0

Interestingly, only one of the compounds with the $I\bar{4}2d$ space group has a notable difference between the direct electronic and optical band gap. To understand why, the band diagrams for $LiAlTe_2$ and $LiGaTe_2$ are plotted with projected orbital contributions to each band in Fig 6.7. The orbital contributions are stacked on top of each other in the order of the labels. Consequently, the order of the orbital stacking affects the outcome of the plot. The latter orbitals might therefore come of with a larger contribution to the band structure than it really has. By looking at the the projected band structure of both $LiAlTe_2$ and $LiGaTe_2$ in Fig 6.7 one can see that there are different bands constituting the direct band gap at Γ.

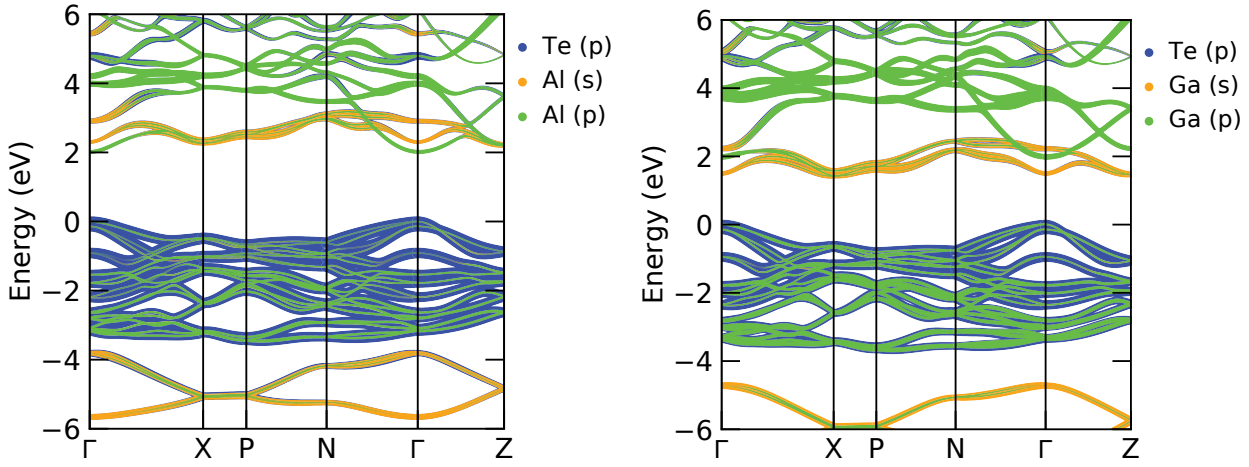

(a) $LiAlTe_2$ **(b)** $LiGaTe_2$

Figure 6.7: Band structures with orbital projected DOS for the bad absorber $LiAlTe_2$ (**a**) and good absorber (**b**), both with the space group $I\bar{4}2d$.

Both compounds have a VBM governed by Te p states, but for $LiAlTe_2$ it is the p-orbital of the B-cation that governs the CBM, while for $LiGaTe_2$ it is the s-orbital of the B-cation governing the CBM. This likely happens due to the greater spatial extent of Ga's 4s-orbitals compared to Al's 3s-orbitals and the same phenomenon is also happening with $LiInTe_2$ due to its large 5s-orbitals. These projected band diagrams are implying that the transition of an electron at Γ from Te p states to B p states is a forbidden transition. However, Laportes rule of forbidden transitions states that this only happens in centrosymmetric space groups due to breaking of symmetry. The spacegroup $I\bar{4}2d$ does not have an inversion center and is not centrosymmetric. The zoomed in version of the absorbance plot is displayed in Fig 6.8 and shows that electrons from Te p-states are in fact excited to the Al p-states, but it happens at an almost negligible rate. Fewer possible absorption points close to the band edges for $LiAlTe_2$ compared to $LiInTe_2$ can be seen on the DOS-plot in (**a**) and (**b**) in Fig 5.6 and is therefore used as an explanation for the bad absorption in this case.

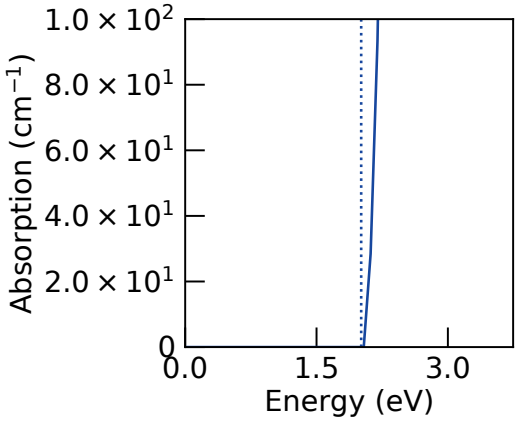

Figure 6.8: Zoomed in absorption plot for $I\bar{4}2d$ $LiAlTe_2$

Optical losses is also found in the two $I4/mcm$ candidates, as well as in all of the screened out compositions with this structure. The orbital-projected band diagram in Fig 6.9 show uniform orbital contribution of the band edges throughout the Brillouin Zone, and so the low absorption can not be explained in the same way as for $LiAlTe_2$. Fig 6.9 also show a zoomed in absorbance plot, which in fact tells us that the material is subject to forbidden transitions. The $I4/mcm$ space group has an inversion center and so the Laporte rule from section 3.1.2 can be used to explain these parity-forbidden transitions. Consequently, $I4/mcm$ is not a symmetry that should be further investigated in similar projects.

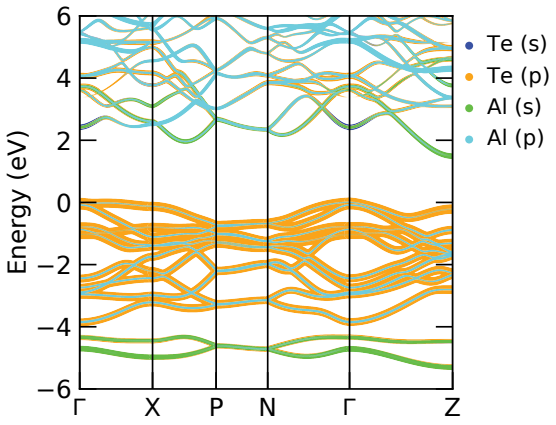

(a) Orbital-projected band diagram of $I4/mcm$ $KAlTe_2$

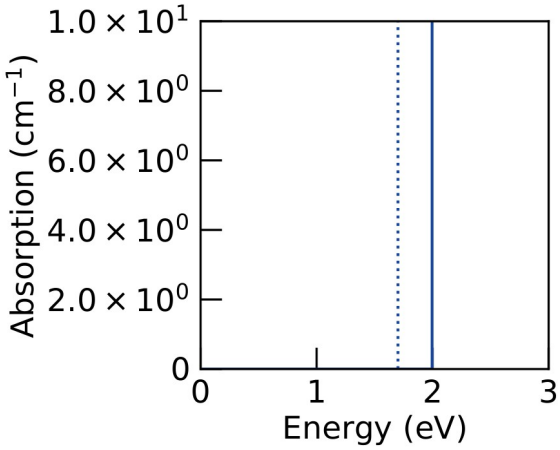

(b) Zoomed in absorbance plot for $I4/mcm$ $KAlTe_2$

Figure 6.9: Orbital-projected band diagram (**a**) and zoomed in absorption plot (**b**) of $I4/mcm$ $KAlTe_2$

6.3 Candidate history

All of the candidates (with the exception of $I\bar{4}2d$ $LiInTe_2$) are computer generated structures, and therefore not necessarily found in neither literature or laboratories before. Table 6.3 states whether or not

the remaining candidates have been predicted in the MP database and if they have been successfully synthesized according to literature.

Table 6.3: The remaining candidates categorized by if they have been predicted by the MP database or can be found synthesized in literature.

Composition	Space group	MP database	Experimental
$LiAlTe_2$	$Pna2_1$	No	Yes [43]
$LiAlTe_2$	$I\bar{4}2d$	Yes	Yes [43]
$LiGaTe_2$	$Pna2_1$	No	No
$LiGaTe_2$	$I\bar{4}2d$	Yes	Yes [44]
$LiInTe_2$	$Pna2_1$	No	No
$LiInTe_2$	$I\bar{4}2d$	Yes	Yes [45]
$KAlTe_2$	$I4/mcm$	Yes	Yes [46]
$RbAlTe_2$	$I4/mcm$	No	No
$CsGaTe_2$	$C2/c_8$	No	No
$CsInTe_2$	$C2/c_{32}$	Yes	Yes [47]

Similarily, screened out candidates that have been predicted stable both by thermodynamic and dynamic stability can be found in Tab 6.4.

Table 6.4: Thermodynamically stable compounds screened out during the electronic screening.

Composition	Structure	Dynamically stable	Mp database	Experimental
$NaAlTe_2$	$I4/mcm$	Unknown	Yes	Yes [46]
$KAlTe_2$	$C2/c_8$	Unknown	No	No
$KAlTe_2$	$C2/c_{32}$	Unknown	Yes	Yes [43]
$KGaTe_2$	$I4/mcm$	Unknown	Yes	No
$KGaTe_2$	$C2/c_8$	Unknown	No	No
$KGaTe_2$	$C2/c_{32}$	Unknown	Yes	Yes [48]
$KInTe_2$	$I4/mcm$	Unknown	Yes	Yes [49]
$KInTe_2$	$C2/c_8$	Unknown	No	No
$RbAlTe_2$	$C2/c_8$	Unknown	No	No
$RbAlTe_2$	$C2/c_{32}$	Unknown	No	No
$RbGaTe_2$	$I4/mcm$	Unknown	No	No
$RbGaTe_2$	$C2/c_8$	No	No	No
$RbGaTe_2$	$C2/c_{32}$	Unknown	No	No
$RbInTe_2$	$I4/mcm$	Unknown	Yes	Yes [50]
$RbInTe_2$	$C2/c_{32}$	Unknown	No	No
$CsGaTe_2$	$C2/c_{32}$	Unknown	Yes	Yes [51]
$CsInTe_2$	$I4/mcm$	Yes	No	No
$CsInTe_2$	$C2/c_8$	Yes	No	No

This means that 4/10 of the still remaining candidates and 11/18 screened out candidates has not before been synthesized according to literature.

6.4 Spin-orbit coupling

Spin-orbit coupling (soc) is the relativistic interaction between the magnetic moment created by an electrons spin and the magnetic moment originating from the orbital movement of the electron. In general, this leads to an additional hamiltonian term in the Schrödinger equation and changes the total energy of the system. The effect of the coupling increases with the heavier elements, but it also depends on the symmetry of the system. Among the remaining candidates, soc, in general, lowered the band gap by around 15%. Additionally, it altered the shape of the bands, mainly by the characteristic soc band splitting.

It is also worth noticing that the compounds with largest soc-induced band gap change had a smaller soc-induced impact on the effective masses. The average of the harmonic averages for all compounds are tabulated in Table 6.5, and shows that it is mainly the VB shape that is affected. This is as expected, because the VB mainly consists of p-orbitals from the heavy Te. This also implies that the large soc-contribution is positive for hole conduction and can be seen as one of the reasons for why Tellurium is a good anion choice for these materials.

Table 6.5: Average effective masses for all compositions with and without spin-orbit contributions

	non-soc	soc
m_h^*	1.00	0.60
m_e^*	0.65	0.61

The band diagrams for the case with largest change in band gap when including spin-orbit contributions is shown in Fig 6.10. It is clear from the figure that the two degenerate bands at the VBM at Γ is split into separate energy values. The dislayed band diagram is for $I4/mcm$ $RbGaTe_2$ which have an inversion center.

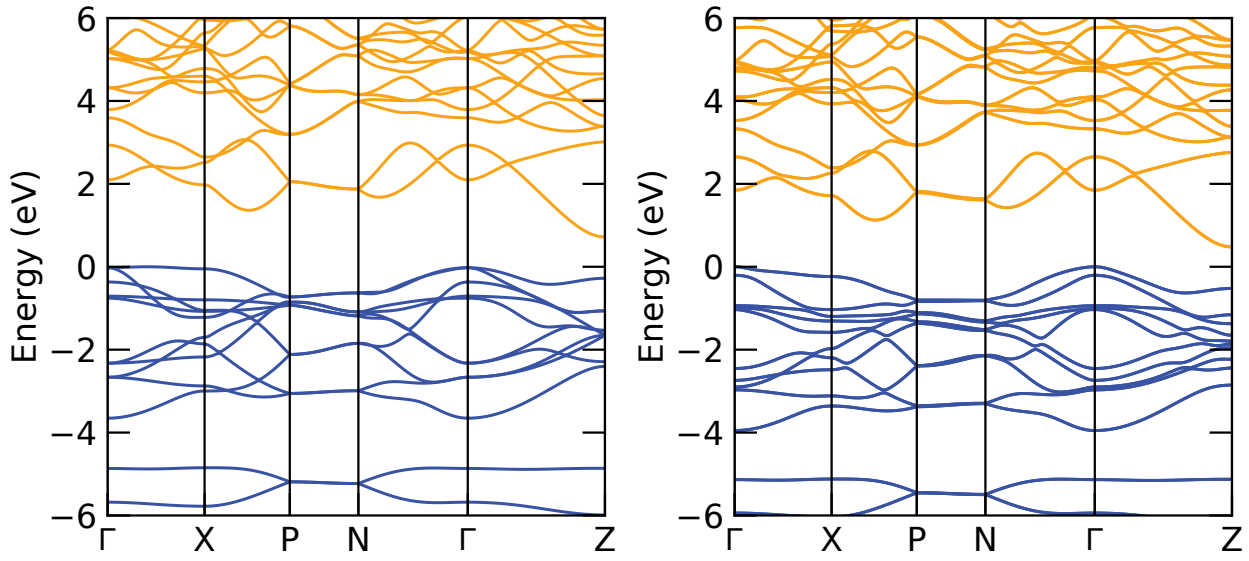

(a) PBEsol band diagram with E_g=0.72

(b) PBEsol+soc band diagram with E_g=0.48

Figure 6.10: Band diagrams for $I4/mcm$ $RbGaTe_2$ both with and without soc-contributions. Without soc (**a**) there are two degenerate bands at the Γ-point. VBM for (**a**) located between Γ and X, while for (**b**) it is at the Γ-point. The direct band gap at the Z-point is, however, unchanged.

6.5 Phonon calculations

All of the phases that passed the electronic structure criteria are dynamically stable according the the phonon dispersion diagrams calculated for each phase, with the exception being the $C2/c_{32}$ $CsInTe_2$-phase. In this case the phonon dispersion relation has yet to be calculated. It stands out from the rest as a much larger cell to begin with. To get sufficient information about the atomic forces in the cell to plot the phonon dispersion diagrams it was necessary to split the calculation into 48 different jobs, each containing a unique supercell. For comparison the other structures needed either 14 or 24 different jobs for the same calculations. Due to both time and computing constrains this calculation therefore has yet to be completed. However, according to Table 5.2, this phase have been successfully synthesized in literature, and so we can conclude with it being dynamically stable. In an ideal world phonon dispersion relations would be calculated for all compounds that have not yet been synthesized in literature, but again, due to both time and computational constraints this was not possible. This is, however, an important step in also determining candidates for other types of applications.

6.6 Final remarks

The fundamental band gap energy threshold was initially planned to be $1.2eV < E_g < 2eV$. However, when including spin-orbit coupling in the electronic structure calculations the band gaps changed more than expected. In order to not exclude possible high-functioning materials, only a lower threshold value of $E_g < 1.2eV$ was applied. This is also the reason that the $I4/mcm$ $KAlTe_2$-structure was included despite having a $m_h^* = 0.62m_0$.

The screening process of this project is heavily influenced by Singh et. al's similar project, with a lot more variety of materials [52]. However, the screening conditions applied in this project are stricter. The ther-

modynamic screening in this project used a cutoff of $\Delta E_{hull} < 0.03$ eV, while Singh et. al used $\Delta E < 0.08$ eV. Deciding a materials phase stability is not a straight-forward task and can not be decided by simply putting an upper threshold of ΔE_{hull}. As this project is subject for both time and computational constrains, strict screening conditions reassures that the final candidates with a higher probability actually will be good candidates. For a high-cost material like Tellurium, the photocatalytic performance have to be excellent for it to actually become available commercially, justifying the strict criteria. However, as a part of future work, also candidates screened out should be further analyzed. As compounds with $Pna2_1$ and $I\bar{4}2d$ has shown excellent properties, these types of structures should be prioritized. The MP database has for instance reported $NaGaTe_2$ in the $I\bar{4}2d$ symmetry to be thermodynamically stable, but was screened out during Råheim's previous project [1].

7 Further work

There are still a lot of work necessary before any concluding remarks can be made on this project. First of all, it is necessary to complete new electronic structure calculations with a hybrid functional to all the remaining candidates to get a better estimation of the actual band gap value. Trends from these results can indicate whether a lower threshold of $E_g > 1.2eV$ was a useful screening parameter based on the actual aspired band gap range of 2.0 eV< E_g < 2.4 eV. Additionally, the vacuum level energy needs to be introduced. This can be done in VASP by using slab model systems [53], and allows the bands to be set in the same reference state as the redox-reactions. As earlier explained this is necessary to thermodynamically drive the reactions forward. Chalcogenides, in general, are known to form p-type materials with low ionization potential [54] [55], which is favourable for the band alignments.

This high-throughput initiative has the potential to initiate and accelerate similar projects with different goals. Compounds that fail the screening due to their electrical characteristics may nevertheless be capable of serving as high-performance devices for other technologies. Compounds with an excessively small band gap may be ideal for solar cell devices, whereas structures with a too large band gap may suggest a good p-type transparent conductor. Therefore, candidates with an unfavourable band gap, but good charge carrier conduction, should also be a part of the following hybrid calculations.

When getting a more correct view of the electronic structure of the candidates, a more accurate map of the different compounds along with their lattice parameters and electronic and optical properties should be made. In this way, predictions for beneficial solid solutions and dopants can produced.

Additionally, focus should be put on the materials stability under the reducing conditions necessary for the CO_2-reduction. Materials with excellent electronic properties are useless if they are unstable and react with the environment they are in. Therefore air reactivity and long-term aquaeous stability needs to be considered. Tellurides have been reported to, in general, have excellent aqueous stability under reducing conditions. The explanation for this can be the larger aqueous stability region for elemental Te, as opposed to the other chalcogenides Se and S [52].

The perhaps most important future step is the synthesizing of the materials and experimental verification of the results. As seen in Table 6.3, a couple of the candidates have not been found synthesized in literature before. Therefore, research revolving around appropriate synthesis routes needs to be evaluated. Additionally, more practical evaluations such as different design-principles for the finished product needs to be applied. One-step excitation systems where a semiconductor takes the role of light harvesting, carrier generation and adsorption centre is something science is moving away from at the moment. More and more research revolves around heterojunctions, z-schemes, co-catalysts and dye-sensitizers. However, the need for a semiconductor with high absorption and large carrier lifetimes is still there, even in these more technological systems [14].

8 Conclusion

In this project 165 computer-generated ternary tellurides have been subject to a systematic screening procedure in order to determine their potential use for photocatalytic CO_2-reduction. The screening process was carried out by ab-initio calculations using DFT together with the semi-local GGA PBEsol functional. The first screening step had already been completed and involved thermodynamic considerations, leaving 28 thermodynamically stable compounds. Out of these, ten made it through the electronic screening process with good band gap values and low charge carrier effective masses. Through a dynamic stability analysis all of the remaining candidates were determined dynamically stable. Significant differences between electronic and optical band gap were observed in three of the remaining candidates, and so they were all screened out. A preferred indirect band gap leaves us with the candidates: $Pna2_1$ $LiGaTe_2$, $I\bar{4}2d$ $LiGaTe_2$ and $C2/c_8$ $CsGaTe_2$. The direct absorbing candidates that are left are: $Pna2_1$ $LiAlTe_2$, $Pna2_1$ $LiInTe_2$, $I\bar{4}2d$ $LiInTe_2$ and $C2/c_{32}$ $CsInTe_2$.

Among the seven remaining candidates, three have not yet been found mentioned in literature. Likewise, 14 screened-out candidates have been predicted to be thermodynamically stable for the first time, with four of them even being dynamically stable. These are materials that is not sufficiently suitable for photocatalytic CO_2-reduction according to the strict screening criteria set in this project, but still may have their uses for other technological applications.

A more in-depth analysis of emerging trends and structural influences of the electronic structure was also completed. The A cation was predicted to mostly influence the spatial structure of the compounds, while the B cation had the most influence on the electronic structure. The preferred B cation was determined to be Al due to its favourable large band gap. The difference between band gap values for Ga and In was remarkably small. The space groups $Pna2_1$ and $I\bar{4}2d$ is preferred due to their well dispersed corner-sharing $[BTe_4]$- tetrahedra leading to overall good orbital overlap between B s orbitals and Te p orbitals. The space group $I4/mcm$ is characterized by edge-sharing $[BTe_4]$ tetrahedra, bringing the B cations close to each other leading to some of the best electron effective masses. However, it is not seen as a favourable space group due to small band gaps as well as forbidden absorption transitions close to the band edges. The small monoclinic cell, $C2/c_8$, is characterized by an anisotropic structure and consistently flat conduction bands. It is therefore not preferred due to large effective masses. The large monoclinic cell, $C2/c_{32}$ is characterized by a layered structure where the interlayer thickness determines the charge carrier conduction. This means that a thin film ordered system is favoured, but the candidate $CsInTe_2$ is still a good candidate based on its bulk properties.

There are still further properties needed to consider before the project can go to the experimental stage. This includes more accurate band gap calculations using a hybrid functional, 2D slab calculations for band edge alignments and aquaeous stability analysis. Additionally, an in-depth analysis of different different design-principles for each of the remaining candidate is necessary.

Bibliography

[1] Ivar Loland Råheim. Computational materials design of materials for CO_2 conversion using sunlight. NTNU - Norges teknisk-naturvitenskapelige universitet, 2020.

[2] Ehsanul Kabir, Pawan Kumar, Sandeep Kumar, Adedeji A. Adelodun, and Ki-Hyun Kim. Solar energy: Potential and future prospects. *Renewable and Sustainable Energy Reviews*, 82:894–900, 2018. ISSN 1364-0321. doi: https://doi.org/10.1016/j.rser.2017.09.094. URL https://www.sciencedirect.com/science/article/pii/S1364032117313485.

[3] Severin N. Habisreutinger, Lukas Schmidt-Mende, and Jacek K. Stolarczyk. Photocatalytic Reduction of CO2 on TiO2 and Other Semiconductors. *Angewandte Chemie International Edition*, 52(29):7372–7408, 2013. doi: https://doi.org/10.1002/anie.201207199. URL https://onlinelibrary.wiley.com/doi/abs/10.1002/anie.201207199.

[4] Maarten de Jong, Wei Chen, Thomas Angsten, Anubhav Jain, Randy Notestine, Anthony Gamst, Marcel Sluiter, Chaitanya Krishna Ande, Sybrand van der Zwaag, Jose J Plata, Cormac Toher, Stefano Curtarolo, Gerbrand Ceder, Kristin A. Persson, and Mark Asta. Charting the complete elastic properties of inorganic crystalline compounds. *Scientific Data*, 2, 2015. doi: 10.1038/sdata.2015.9. URL http://perssongroup.lbl.gov/papers/sdata2015-elasticprops.pdf.

[5] David Sholl and Janice Steckel. *Density Functional Theory*. John Wiley & Sons, Ltd, 2009.

[6] John P. Perdew, Adrienn Ruzsinszky, Gábor I. Csonka, Oleg A. Vydrov, Gustavo E. Scuseria, Lucian A. Constantin, Xiaolan Zhou, and Kieron Burke. Restoring the Density-Gradient Expansion for Exchange in Solids and Surfaces. *Physical Review Letters*, 100(13):136406, April 2008. doi: 10.1103/PhysRevLett.100.136406. URL https://link.aps.org/doi/10.1103/PhysRevLett.100.136406. Publisher: American Physical Society.

[7] Fabien Tran and Peter Blaha. Accurate Band Gaps of Semiconductors and Insulators with a Semilocal Exchange-Correlation Potential. *Physical Review Letters*, 102(22):226401, June 2009. ISSN 0031-9007, 1079-7114. doi: 10.1103/PhysRevLett.102.226401. URL https://link.aps.org/doi/10.1103/PhysRevLett.102.226401.

[8] G. M. Dongho Nguimdo and Daniel P. Joubert. A density functional (PBE, PBEsol, HSE06) study of the structural, electronic and optical properties of the ternary compounds AgAlX2 (X = S, Se, Te). *The European Physical Journal B*, 88(5):113, May 2015. ISSN 1434-6036. doi: 10.1140/epjb/e2015-50478-x. URL https://doi.org/10.1140/epjb/e2015-50478-x.

[9] Edward S. Sachs, Juergen Hinze, and Nora H. Sabelli. Frozen core approximation, a pseudopotential method tested on six states of NaH. *The Journal of Chemical Physics*, 62(9):3393–3398, May 1975. ISSN 0021-9606. doi: 10.1063/1.430993. URL https://aip.scitation.org/doi/abs/10.1063/1.430993. Publisher: American Institute of Physics.

[10] G. Kresse and D. Joubert. From ultrasoft pseudopotentials to the projector augmented-wave method. *Phys. Rev. B*, 59:1758–1775, Jan 1999. doi: 10.1103/PhysRevB.59.1758. URL https://link.aps.org/doi/10.1103/PhysRevB.59.1758.

[11] Charles Kittel. *Introduction to Solid State Physics*. John Wiley & Sons, Inc, 8 edition, 2005.

[12] Peter Würfel. *Physics of Solar Cells: From Basic Principles to Advanced Concepts*. Wiley, 2nd edition edition, 2009.

[13] Otto Laporte and William F. Meggers. Some Rules of Spectral Structure. *J. Opt. Soc. Am.*, 11(5): 459–463, November 1925. doi: 10.1364/JOSA.11.000459. URL http://www.osapublishing.org/abstract.cfm?URI=josa-11-5-459. Publisher: OSA.

[14] Kan Li, Bosi Peng, and Tianyou Peng. Recent Advances in Heterogeneous Photocatalytic CO2 Conversion to Solar Fuels. *ACS Catalysis*, 6(11):7485–7527, November 2016. doi: 10.1021/acscatal.6b02089. URL https://doi.org/10.1021/acscatal.6b02089. Publisher: American Chemical Society.

[15] Jinghua Wu, Yang Huang, Wen Ye, and Yanguang Li. CO2 Reduction: From the Electrochemical to Photochemical Approach. *Advanced Science*, 4(11), September 2017. ISSN 2198-3844. doi: 10.1002/advs.201700194. URL https://www.ncbi.nlm.nih.gov/pmc/articles/PMC5700640/.

[16] Wenguang Tu, Yong Zhou, and Zhigang Zou. Photocatalytic Conversion of CO2 into Renewable Hydrocarbon Fuels: State-of-the-Art Accomplishment, Challenges, and Prospects. *Advanced Materials*, 26(27):4607–4626, July 2014. ISSN 0935-9648. doi: 10.1002/adma.201400087. URL https://doi.org/10.1002/adma.201400087. Publisher: John Wiley & Sons, Ltd.

[17] Shunsuke Sato, Takeo Arai, and Takeshi Morikawa. Toward Solar-Driven Photocatalytic CO2 Reduction Using Water as an Electron Donor. *Inorganic Chemistry*, 54(11):5105–5113, 2015. doi: 10.1021/ic502766g. URL https://doi.org/10.1021/ic502766g.

[18] Siris Laursen and Samiksha Poudyal. Chapter 8 - Photo- and Electro-Catalysis: CO2 Mitigation Technologies. In Fan Shi and Bryan Morreale, editors, *Novel Materials for Carbon Dioxide Mitigation Technology*, pages 233–268. Elsevier, Amsterdam, January 2015. ISBN 978-0-444-63259-3. doi: 10.1016/B978-0-444-63259-3.00008-2. URL http://www.sciencedirect.com/science/article/pii/B9780444632593000082.

[19] Lorenzo Mino, Giuseppe Spoto, and Anna Maria Ferrari. CO2 Capture by TiO2 Anatase Surfaces: A Combined DFT and FTIR Study. *The Journal of Physical Chemistry C*, 118(43):25016–25026, October 2014. ISSN 1932-7447. doi: 10.1021/jp507443k. URL https://doi.org/10.1021/jp507443k. Publisher: American Chemical Society.

[20] Severin N. Habisreutinger, Lukas Schmidt-Mende, and Jacek K. Stolarczyk. Photocatalytic Reduction of CO2 on TiO2 and Other Semiconductors. *Angewandte Chemie International Edition*, 52(29):7372–7408, 2013. ISSN 1521-3773. doi: 10.1002/anie.201207199. URL https://onlinelibrary.wiley.com/doi/abs/10.1002/anie.201207199.

[21] Nelson Belzile and Yu-Wei Chen. Tellurium in the environment: A critical review focused on natural waters, soils, sediments and airborne particles. *Applied Geochemistry*, 63:83–92, 2015. ISSN 0883-2927. doi: https://doi.org/10.1016/j.apgeochem.2015.07.002. URL https://www.sciencedirect.com/science/article/pii/S088329271530007X.

[22] Alessandro Romeo and Elisa Artegiani. CdTe-Based Thin Film Solar Cells: Past, Present and Future. *Energies*, 14(6), 2021. ISSN 1996-1073. doi: 10.3390/en14061684. URL https://www.mdpi.com/1996-1073/14/6/1684.

[23] Liam A. Bullock, Magali Perez, Joseph G. Armstrong, John Parnell, John Still, and Joerg Feldmann. Selenium and tellurium resources in Kisgruva Proterozoic volcanogenic massive sulphide deposit (Norway). *Ore Geology Reviews*, 99:411–424, 2018. ISSN 0169-1368. doi: https://doi.org/10.1016/j.oregeorev.2018.06.023. URL https://www.sciencedirect.com/science/article/pii/S016913681830235X.

[24] Nasrin Sarmadian, Rolando Saniz, Bart Partoens, and Dirk Lamoen. Easily doped p-type, low hole effective mass, transparent oxides. *Scientific Reports*, 6(1):20446, February 2016. ISSN 2045-2322. doi: 10.1038/srep20446. URL https://doi.org/10.1038/srep20446.

[25] Huidong Shen, Tim Peppel, Jennifer Strunk, and Zhenyu Sun. Photocatalytic reduction of co2 by metal-free-based materials: Recent advances and future perspective. *Solar RRL*, 4(8):1900546, 2020. doi: https://doi.org/10.1002/solr.201900546. URL https://onlinelibrary.wiley.com/doi/abs/10.1002/solr.201900546.

[26] O. Malyi and Sopiha K. Energy, phonon, and dynamic stability criteria of 2d materials. *Centre for Materials Science and Nanotechnology, Department of Physics, University of Oslo*, 2019.

[27] Dove, M.T. Introduction to the theory of lattice dynamics. *JDN*, 12:123–159, 2011. doi: 10.1051/sfn/201112007. URL https://doi.org/10.1051/sfn/201112007.

[28] The vasp manual. URL https://www.vasp.at/wiki/index.php/The_VASP_Manual.

[29] Hendrik J. Monkhorst and James D. Pack. Special points for brillouin-zone integrations. *Phys. Rev. B*, 13:5188–5192, Jun 1976. doi: 10.1103/PhysRevB.13.5188. URL https://link.aps.org/doi/10.1103/PhysRevB.13.5188.

[30] A. Jain, S. P. Ong, G. Hautier, W. Chen, W. D. Richards, S. Dacek, S. Cholia, D. Gunter, D. Skinner, G. Ceder, and K. A. Persson. Commentary: The materials project: A materials genome approach to accelerating materials innovation. *APL Mater.*, (1), 2013. doi: 10.1063/1.4812323.

[31] Atsushi Togo and Isao Tanaka. Spglib: a software library for crystal symmetry search. *arXiv:1808.01590 [cond-mat]*, August 2018. URL http://arxiv.org/abs/1808.01590.

[32] Shyue Ping Ong, Shreyas Cholia, Anubhav Jain, Miriam Brafman, Dan Gunter, Gerbrand Ceder, and Kristin A. Persson. The Materials Application Programming Interface (API): A simple, flexible and efficient API for materials data based on REpresentational State Transfer (REST) principles. *Computational Materials Science*, 97:209–215, 2015. ISSN 0927-0256. doi: https://doi.org/10.1016/j.commatsci.2014.10.037. URL https://www.sciencedirect.com/science/article/pii/S0927025614007113.

[33] Shyue Ping Ong, Lei Wang, Byoungwoo Kang, and Gerbrand Ceder. Lifepo2 phase diagram from first principles calculations. *Chemistry of Materials*, 20(5):1798–1807, 2008. doi: 10.1021/cm702327g. URL https://doi.org/10.1021/cm702327g.

[34] Amset python package. URL https://github.com/hackingmaterials/amset.

[35] Alex M. Ganose, Junsoo Park, Alireza Faghaninia, Rachel Woods-Robinson, Kristin A. Persson, and Anubhav Jain. Efficient calculation of carrier scattering rates from first principles. *Nature Communications*, 12(1):2222, April 2021. ISSN 2041-1723. doi: 10.1038/s41467-021-22440-5. URL https://doi.org/10.1038/s41467-021-22440-5.

[36] Alex M. Ganose, Adam J. Jackson, and David O. Scanlon. sumo: Command-line tools for plotting and analysis of periodic *ab initio* calculations. *Journal of Open Source Software*, 3(28):717, 2018. doi: 10.21105/joss.00717. URL https://doi.org/10.21105/joss.00717.

[37] Peter E. Blöchl, O. Jepsen, and O. K. Andersen. Improved tetrahedron method for brillouin-zone integrations. *Phys. Rev. B*, 49:16223–16233, Jun 1994. doi: 10.1103/PhysRevB.49.16223. URL https://link.aps.org/doi/10.1103/PhysRevB.49.16223.

[38] Anubhav Jain, Geoffroy Hautier, Charles J. Moore, Shyue Ping Ong, Christopher C. Fischer, Tim Mueller, Kristin A. Persson, and Gerbrand Ceder. A high-throughput infrastructure for density functional theory calculations. *Computational Materials Science*, 50(8):2295–2310, 2011. ISSN 0927-0256. doi: https://doi.org/10.1016/j.commatsci.2011.02.023. URL https://www.sciencedirect.com/science/article/pii/S0927025611001133.

[39] Koichi Momma and Fujio Izumi. Vesta: A three-dimensional visualization system for electronic and structural analysis. *Journal of Applied Crystallography - J APPL CRYST*, 41:653–658, 06 2008. doi: 10.1107/S0021889808012016.

[40] A Togo and I Tanaka. First principles phonon calculations in materials science. *Scr. Mater.*, 108:1–5, Nov 2015.

[41] R. R. Reddy and Y. Nazeer Ahammed. Relation between energy gap and electronic polarizability of ternary chalcopyrites. *Infrared Physics & Technology*, 37(4):505–507, 1996. ISSN 1350-4495. doi: https://doi.org/10.1016/1350-4495(95)00073-9. URL https://www.sciencedirect.com/science/article/pii/1350449595000739.

[42] Jeyakumar Ramanujam and Udai P. Singh. Copper indium gallium selenide based solar cells – a review. *Energy Environ. Sci.*, 10(6):1306–1319, 2017. doi: 10.1039/C7EE00826K. URL http://dx.doi.org/10.1039/C7EE00826K. Publisher: The Royal Society of Chemistry.

[43] J. Kim and T. Hughbanks. Synthesis and structures of new ternary aluminium chalcogenides: Li al se2, alpha-li al te2, and betali al te2. *Inorganic Chemistry*, 39:3092–3097, 2000.

[44] L. Isaenko, P. Krinitsin, V. Vedenyapin, A. Yelisseyev, A. Merkulov, J.J. Zondy, and V. Petrov. Li ga te2 : a new highly nonlinear chalcopyrite optical crystal for the mid-ir. *Crystal Growth and Design*, 5: 1325–1329, 2005.

[45] G. Kuehn, B. Schumann, D. Oppermann, H. Neumann, and H. Sobotta. Preparation, structure, and infrared lattice vibrations of li in te2. *Zeitschrift fuer Anorganische und Allgemeine Chemie (1950) (DE)*, 531:61–66, 1985.

[46] J. Weis, R. Schaefer, and G. Schoen. Neue ternaere telluride und selenide der alkalimetalle mit elementen der 3. hauptgruppe. *Zeitschrift fuer Naturforschung, Teil B. Anorganische Chemie, Organische Chemie (33,1978-41,1986)*, 31:1336–1340, 1976.

[47] Hua Lin, Jin-Ni Shen, Ling Chen, and Li-Ming Wu. Quaternary supertetrahedra-layered telluride csmninte3. why does this type of chalcogenide tilt? *Inorganic Chemistry*, 52:10726–10728, 2013.

[48] J. Kim and T. Hughbanks. Synthesis and structures of ternary chalcogenides of aluminium and gallium with stacking faults: K m q2 (m= al, ga; q= se, te). *Journal of Solid State Chemistry*, 149:242–251, 2000.

[49] E.R. Franke and H. Schaefer. Zur strukturchemie ternaerer telluride der alkali- und erdalkalimetalle mit den elementen der dritten hauptgruppe. *Zeitschrift fuer Naturforschung, Teil B. Anorganische Chemie, Organische Chemie (2,1947-32,1977)*, 27:1308–1315, 1972.

[50] S.S. Dhingra and R.C. Haushalter. One-dimensional inorganic polymers: synthesis and structural characterization of the main-group metal polymers k2 hg sn te4, (et4 n)2 hg sn te4, (ph p4) ge in te4 and rb in te2. *Chemistry of Materials*, 6:2376–2381, 1994.

[51] E.J. Wu, M.A. Pell, T.M. Fuelberth, and J.A. Ibers. Crystal structure of cesium gallium ditelluride, cs ga te2. *Zeitschrift fuer Kristallographie - New Crystal Structures*, 212:91–91, 1997.

[52] Arunima K. Singh, Joseph H. Montoya, John M. Gregoire, and Kristin A. Persson. Robust and synthesizable photocatalysts for CO 2 reduction: a data-driven materials discovery. *Nature Communications*, 10(1):443, January 2019. ISSN 2041-1723. doi: 10.1038/s41467-019-08356-1. URL https://www.nature.com/articles/s41467-019-08356-1. Number: 1 Publisher: Nature Publishing Group.

[53] Hong Jiang and Yu-Chen Shen. Ionization potentials of semiconductors from first-principles. *The Journal of Chemical Physics*, 139(16):164114, 2013. doi: 10.1063/1.4826321. URL https://doi.org/10.1063/1.4826321.

[54] Benjamin A. D. Williamson, John Buckeridge, Jennilee Brown, Simon Ansbro, Robert G. Palgrave, and David O. Scanlon. Engineering Valence Band Dispersion for High Mobility p-Type Semiconductors. *Chemistry of Materials*, 29(6):2402–2413, March 2017. ISSN 0897-4756, 1520-5002. doi: 10.1021/acs.chemmater.6b03306. URL https://pubs.acs.org/doi/10.1021/acs.chemmater.6b03306.

[55] Ramya Kormath Madam Raghupathy, Hendrik Wiebeler, Thomas D. Kühne, Claudia Felser, and Hossein Mirhosseini. Database Screening of Ternary Chalcogenides for P-type Transparent Conductors. *Chemistry of Materials*, 30(19):6794–6800, October 2018. ISSN 0897-4756. doi: 10.1021/acs.chemmater.8b02719. URL https://doi.org/10.1021/acs.chemmater.8b02719. Publisher: American Chemical Society.

[56] Mois I. Aroyo, Danel Orobengoa, Gemma de la Flor, Emre S. Tasci, J. Manuel Perez-Mato, and Hans Wondratschek. Brillouin-zone database on the ıt Bilbao Crystallographic Server. *Acta Crystallographica Section A*, 70(2):126–137, March 2014. doi: 10.1107/S205327331303091X. URL https://doi.org/10.1107/S205327331303091X.

[57] C. J. Bradley and Arthur P. Cracknell. *The mathematical theory of symmetry in solids: representation theory for point groups and space groups*. Clarendon Press, 2010.

Appendix

A Brillouin Zones in reciprocal space

In the following section all of the standardized Brillouin Zones of the relevant space groups are shown, along with the position of the high-symmetry points. They are all collected from the Bilbao Crystallographic Server [56]. Different sources of material often uses different forms of notation. The sumo python package used for band diagram plotting uses a different form of notation (from Bradley and Cracknell [57]) than the Bilbao Crystallographic Server. The most important difference is that the M point in A.4 is what is referred to as the Z point during the report.

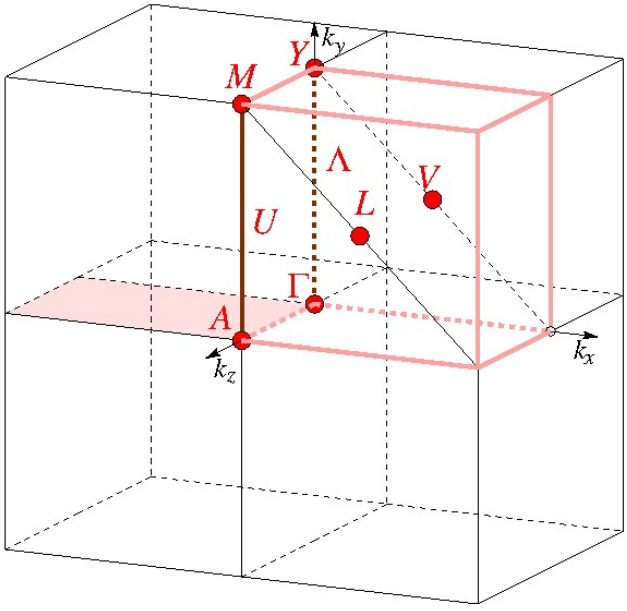

Figure A.1: Illustration of the first BZ for the monoclinic space group $C2/c$.

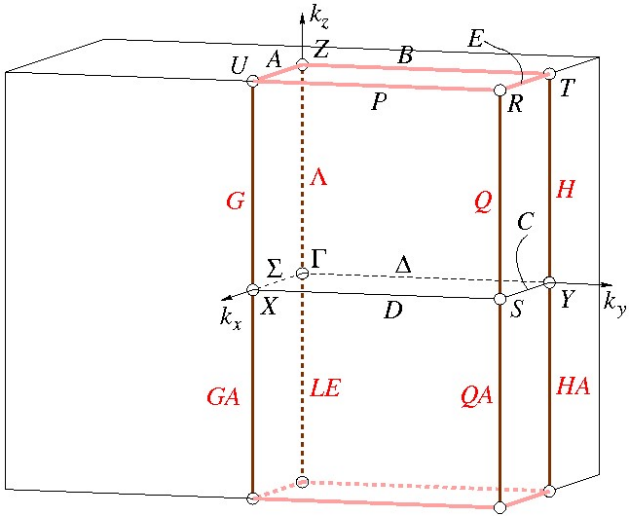

Figure A.2: Illustration of the first BZ for the orthorombic space group $Pna2_1$.

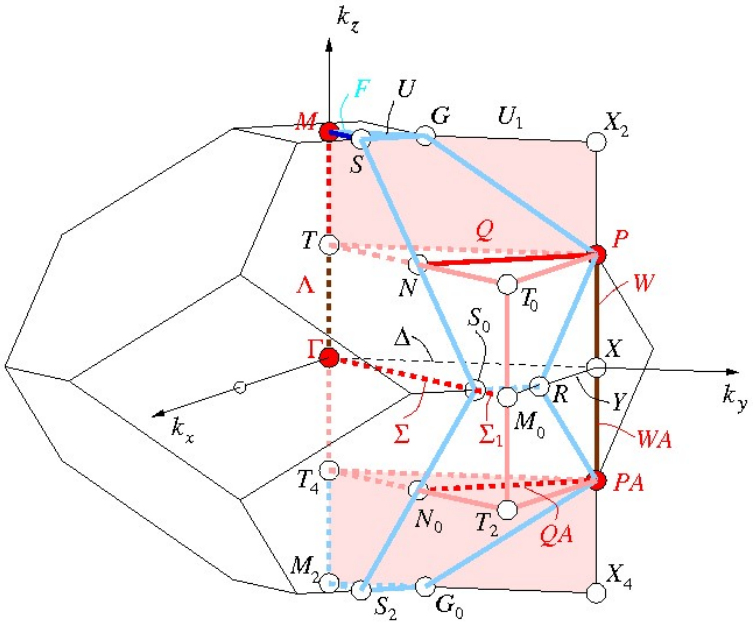

Figure A.3: Illustration of the first BZ for the tetragonal space group $I\bar{4}2d$.

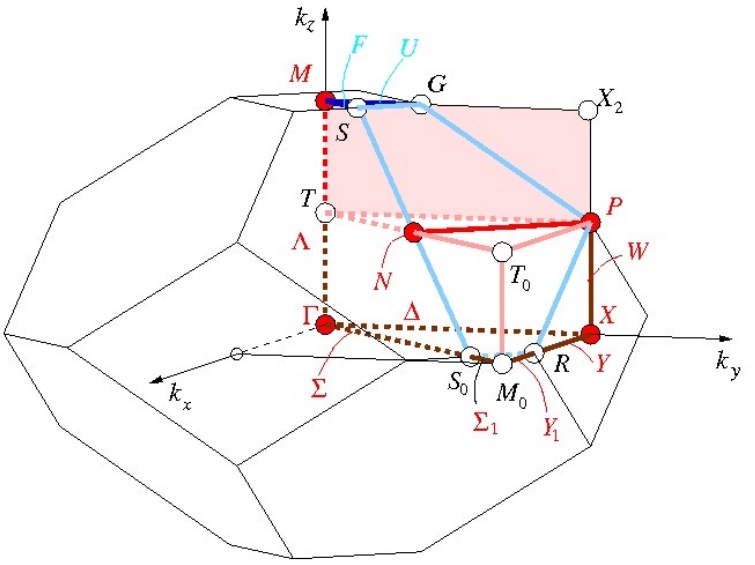

Figure A.4: Illustration of the first BZ for the tetragonal space group $I4/mcm$.

B VASP Input files

In this part essential input-files for running VASP-calculations have been listed. The compound these files have been used for is the tetragonal $I\bar{4}2d$ phase of $LiAlTe_2$.

```
SYSTEM = Generic Input
start Parameters
  NWRITE      = 2       ! Medium-level information output
  ISTART      = 1       ! read existing wavefunction; if there
  INIWAV      = 1       ! Random initial wavefunction; otherwise
  !ICORELEVEL = 1        ! Print core levels
  !ICHARG     = 11      ! Non-selfconsistent: GGA/LDA band structures
  !NBANDS     = 130     ! No. bands
parallelisation
  NCORE  = 16           ! No. cores per orbital
  !LPLANE = .TRUE.      ! Real space distribution; supercells
  !KPAR   = 2           ! K-point parallelisation
electronic relaxation
  PREC     = Normal  ! Precision level
  ALGO     = Normal     ! SCF minimisation algorithm; 38/48 combo
  ENMAX    = 500        ! Plane-wave cutoff
  NELM     = 200        ! Max SCF steps
  NELMIN   = 2          ! Min SCF steps
  EDIFF    = 1E-05      ! SCF energy convergence
  GGA      = PS         ! PBEsol exchange-correlation
  LASPH    = .TRUE.     ! Non-spherical elements; d/f convergence
  LREAL    = .FALSE.      ! Projection operators: automatic
  ADDGRID = .TRUE.     ! Increase grid; helps GGA convergence
  !IVDW = 11            ! Grimme's D3 VDW correction
ionic relaxation
  EDIFFG = -0.01        ! Ionic convergence; eV/AA^3
  NSW    = 0            ! Max ionic steps
  IBRION = 1            ! Algorithm: 0-MD; 1-Quasi-New; 2-CG
  ISIF   = 3            ! Stress/relaxation: 2-Ions, 3-Shape/Ions/V, 7-Vol
  ISYM   = 2            ! Symmetry: 0-none; 2=GGA; 3=hybrids
  NBLOCK = 1            ! Update XDATCAR every X steps
  KBLOCK = 40           ! Update PCDAT and DOSCAR every X*NBLOCK steps
  ISMEAR = 0            ! Gaussian smearing; metals:1
  SIGMA  = 0.02         ! Smearing value in eV; metals:0.2
  IWAVPR = 1            ! charge density extrapolation: 0-non 1-charg 2-wave 3-comb
  POTIM  = 0.1        ! Timestep in fs
misc
  LORBIT  = 11          ! PAW radii for projected DOS
  NEDOS   = 2000        ! DOSCAR points
  !LVHAR   = .TRUE.     ! Ionic and Hartree potential
  !RWIGS   = 1.5 1.5    ! Radii for each atomic species
  !LOPTICS = .TRUE.     ! Output OPTIC file
  LVTOT   = .TRUE.     ! Electrostatic potential
  !LELF    = .TRUE.     ! Localisation function
hybrid-dft
  !LHFCALC  = .TRUE.    ! Activate HF
  !PRECFOCK = F         ! HF FFT grid
  !NKRED    = 2         ! Reduce k-grid-even only
  !ALGO     = DAMPED    ! Dampened MD SCF; IALGO=53
  !ALGO     = All       ! SCF Combo; ALGO=58
  !TIME     = 0.30      ! Timestep for IALGO5X
  !HFLMAX   = 4         ! HF cut-off: 4d,6f
  !HFSCREEN = 0.207     ! Switch to screened exchange; e.g. HSE06
  !AEXX     = 0.25      ! 25% HF exchange; e.g. PBE0
magnetic
  !ISPIN    = 2         ! Enable spin polarisation
  !MAGMOM   = 5 0       ! Initial magnetic moment on each ion
  !NUPDOWN = -1         ! Enforce spin multiplet
  !LSORBIT = .TRUE.     ! Spin-orbit coupling
dft+u
  !LDAU     = .TRUE.    ! Activate DFT+U
  !LDATYPE  = 2         ! Dudarev; only U-J matters
  !LDAUL    = 2 -1      ! Orbitals for each species
  !LDAUU    = 2  0      ! U for each species
  !LDAUJ    = 0  0      ! J for each species
  !LMAXMIX  = 4         ! Mixing cut-off; 4-d, 6-f
decomposed charge density
  !LPARD = .TRUE.       ! Generate PARCHG
  !EINT  = -10 0        ! Energy range
  !NBMOD = -3           ! With reference to Ef
  !KPUSE = 1            ! Over k-points
  !IBAND = 20           ! Over bands
```

Listing 1: INCAR-file for the first step of calculations for thermodynamic relaxation of $I\bar{4}2d$ tetragonal of LiAlTe2
An explanation for all the parameters can be found in the VASP-wiki INCAR site.

```
Li2 Al2 Te4
1.0
-3.772217 3.772217 4.868791
3.772217 -3.772217 4.868791
3.772217 3.772217 -4.868791
Li Al Te
2 2 4
direct
0.000000 0.000000 0.000000 Li
0.750000 0.250000 0.500000 Li
0.500000 0.500000 0.000000 Al
0.250000 0.750000 0.500000 Al
0.375000 0.444427 0.569427 Te
0.875000 0.805573 0.430573 Te
0.555573 0.125000 0.930573 Te
0.194427 0.625000 0.069427 Te
```

Listing 2: POSCAR-file for the unrelaxed structure downloaded from materials project [4].

```
PAW_PBE Li_sv 10Sep2004
   3.00000000000000
 parameters from PSCTR are:
   VRHFIN =Li: 1s2s2p
   LEXCH  = PE
   EATOM  =   202.7858 eV,   14.9043 Ry

   TITEL  = PAW_PBE Li_sv 10Sep2004
   LULTRA =        F    use ultrasoft PP ?
   IUNSCR =        0    unscreen: 0-lin 1-nonlin 2-no
   RPACOR =    0.000    partial core radius
   POMASS =    7.010; ZVAL   =    3.000    mass and valenz
   RCORE  =    1.700    outmost cutoff radius
   RWIGS  =    2.050; RWIGS  =    1.085    wigner-seitz radius (au A)
   ENMAX  =  499.034; ENMIN  =  374.276 eV
   ICORE  =        2    local potential
   LCOR   =        T    correct aug charges
   LPAW   =        T    paw PP
   EAUG   =  628.945
   RMAX   =    1.732    core radius for proj-oper
   RAUG   =    1.300    factor for augmentation sphere
   RDEP   =    1.728    radius for radial grids
   RDEPT  =    1.329    core radius for aug-charge

   Atomic configuration
    4 entries
      n   l    j            E        occ.
      1   0   0.50       -51.8549    2.0000
      2   0   0.50        -2.8742    1.0000
      2   1   0.50        -1.3606    0.0000
      3   2   1.50        -1.3606    0.0000
   Description
      l       E           TYP  RCUT    TYP  RCUT
      0     -51.8548813     23  1.400
      0      -2.8742052     23  1.700
      1      -1.3605826     23  1.400
      2      -1.3605826     23  1.400
   Error from kinetic energy argument (eV)
   NDATA  =      100
   STEP   =   20.000   1.050
  58.3      57.8      57.5      56.8      56.5      55.8      55.0      54.6
  53.8      53.0      52.6      51.7      50.7      49.8      48.8      47.8
  46.8      45.8      44.7      43.1      42.0      40.9      39.3      38.2
  37.1      35.4      33.8      32.7      31.1      29.5      27.9      26.4
  24.9      23.4      22.0      20.6      18.9      17.6      16.0      14.8
  13.4      12.0      10.8      9.59      8.50      7.50      6.59      5.56
  4.82      4.00      3.29      2.79      2.25      1.80      1.35      1.05
 0.799     0.567     0.392     0.265     0.174     0.111    0.700E-01 0.407E-01
 0.266E-01 0.180E-01 0.142E-01 0.127E-01 0.118E-01 0.110E-01 0.958E-02 0.784E-02
 0.601E-02 0.434E-02 0.287E-02 0.199E-02 0.143E-02 0.121E-02 0.115E-02 0.114E-02
 0.108E-02 0.940E-03 0.751E-03 0.538E-03 0.367E-03 0.261E-03 0.214E-03 0.202E-03
 0.200E-03 0.186E-03 0.155E-03 0.119E-03 0.824E-04 0.610E-04 0.510E-04 0.480E-04
 0.448E-04 0.386E-04 0.294E-04 0.218E-04
END of PSCTR-controll parameters
 local part
   109.604107337578
  0.76732912E+01  0.76711766E+01  0.76671017E+01  0.76603243E+01  0.76508652E+01
  0.76387532E+01  0.76240248E+01  0.76067238E+01  0.75869009E+01  0.75646133E+01
```

Listing 3: Beginning of POTCAR file.The POTCAR file contains the pseudopotential for each atomic species used in the calculation. It is generated through VASP-implented code for each stochiometry.

```
Automatic mesh
0
Gamma
   5    5    7
   0.   0.   0.
```

Listing 4: KPOINTS-file using a Γ-centered Monkhorst-Pack scheme [29]-

```
$\Gamma$ -> X -> P -> N -> \Gamma -> Z
158
Reciprocal
0.0 0.0 0.0 1 \Gamma
0.0 0.0 0.011627906976744186 1
0.0 0.0 0.023255813953488372 1
0.0 0.0 0.03488372093023256 1
0.0 0.0 0.046511627906976744 1
0.0 0.0 0.05813953488372093 1
0.0 0.0 0.06976744186046512 1
0.0 0.0 0.08139534883720931 1
0.0 0.0 0.09302325581395349 1
0.0 0.0 0.10465116279069768 1
0.0 0.0 0.11627906976744186 1
0.0 0.0 0.12790697674418605 1
0.0 0.0 0.13953488372093023 1
0.0 0.0 0.1511627906976744 1
0.0 0.0 0.16279069767441862 1
0.0 0.0 0.1744186046511628 1
0.0 0.0 0.18604651162790697 1
0.0 0.0 0.19767441860465115 1
0.0 0.0 0.20930232558139536 1
0.0 0.0 0.22093023255813954 1
0.0 0.0 0.23255813953488372 1
0.0 0.0 0.2441860465116279 1
0.0 0.0 0.2558139534883721 1
0.0 0.0 0.26744186046511625 1
0.0 0.0 0.27906976744186046 1
0.0 0.0 0.29069767441860467 1
0.0 0.0 0.3023255813953488 1
0.0 0.0 0.313953488372093 1
0.0 0.0 0.32558139534883723 1
0.0 0.0 0.3372093023255814 1
0.0 0.0 0.3488372093023256 1
0.0 0.0 0.36046511627906974 1
0.0 0.0 0.37209302325581395 1
0.0 0.0 0.38372093023255816 1
0.0 0.0 0.3953488372093023 1
0.0 0.0 0.4069767441860465 1
0.0 0.0 0.4186046511627907 1
0.0 0.0 0.43023255813953487 1
0.0 0.0 0.4418604651162791 1
0.0 0.0 0.45348837209302323 1
0.0 0.0 0.46511627906976744 1
0.0 0.0 0.47674418604651164 1
0.0 0.0 0.4883720930232558 1
0.0 0.0 0.5 1 X
```

Listing 5: Beginning of the sumo-generated [36] KPOINTS-file oriented in the high-symmetry directions. This part only displays the kpoint sampling between Γ and X.

```
#!/bin/bash -l
#SBATCH --job-name=LAT122
#SBATCH --account=nn9264k
#SBATCH --nodes=4
#SBATCH --ntasks-per-node=16
#SBATCH --time=24:00:00
#SBATCH --exclusive
#SBATCH --partition=normal
SCRATCH_DIRECTORY=${PWD}
module load VASPModules VASP/5.4.4-intel-2017a
mpirun vasp_ncl > vasp_out
echo $PWD >> ~/fin_dir
```

Listing 6: job-file for calculation run on FRAM. The calculation in question is a soc-calculation and is therefore run using vasp_ncl rather than the standard vasp_std.

C Effective masses

The numerical value for all of the effective masses is tabulated here. It includes results both with and without spin-orbit contributions. The "new direction" column is only filled in if the CBM or VBM is located at a different space in the BZ for the soc and non-soc calculations. The negative values correspond to hole effective masses and are separated from the positve electron effective masses. The total refers to the harmonic mean of the values in the different directions.

Table C.1: $I4/mcm$

Structure	Direction	SOC	New direction	Non-SOC	Total	SOC	Non-SOC
$KAlTe_2$	Γ → X	-0.596	(0,0,0.27) → X	-1.772	m_h^*	0.62	1.55
	Γ → N	-0.899	(0,0,0.27) → Γ	-1.381	m_e^*	0.35	0.35
	Γ → Z	-0.479					
	Z → Γ	0.35		0.347			
$KGaTe_2$	Γ → X	-0.711	(0,0,0.27) → X	-1.154	m_h^*	0.66	1.16
	Γ → N	-0.893	(0,0,0.27) → Γ	-1.1708	m_e^*	0.27	0.26
	Γ → Z	-0.498					
	Z → Γ	0.265		0.261			
$KInTe_2$	(0,0,0.17) → X	-1.372	(0,0,0.22) → X	-0.848	m_h^*	1.21	0.90
	(0,0,0.17) → Γ	-1.09	(0,0,0.22) → Γ	-0.952	m_e^*	0.28	0.28
	Z → Γ	0.284		0.278			
$NaAlTe_2$	(0,0,0.22)→ X	-0.675	(0,0,0.25) → X	-0.497	m_h^*	0.70	0.60
	(0,0,0.22) → Γ	-0.721	(0,0,0.25) → Γ	-0.748	m_e^*	0.28	0.30
	Z → Γ	0.284		0.296			
$RbAlTe_2$	Γ → X	-0.411	(0,0,0.21) → X	-3.132	m_h^*	0.47	3.19
	Γ → N	-0.656	(0,0,0.21) → Γ	-3.25	m_e^*	0.35	0.35
	Γ → Z	-0.413					
	Z → Γ	0.354		0.351			
$RbGaTe_2$	Γ → X	-0.397	(0,0,0.21) → X	-2.609	m_h^*	0.43	2.99
	Γ → N	-0.597	(0,0,0.21) → Γ	-3.514	m_e^*	0.29	0.28
	Γ → Z	-0.36					
	Z → Γ	0.287		0.284			
$RbInTe_2$	Γ → X	-0.47	(0,0,0.19) → X	-2.068	m_h^*	0.49	1.74
	Γ → N	-0.703	(0,0,0.19) → Γ	-1.505	m_e^*	0.30	0.30
	Γ → Z	-0.394					
	Z → Γ	0.304		0.299			
$CsInTe_2$	Γ → X	-0.35		-0.203	m_h^*	0.38	0.26
	Γ → N	-0.525		-0.439	m_e^*	0.33	0.32
	Γ → Z	-0.324		-0.232			
	Z → Γ	0.327		0.322			

Table C.2: $C2/c_8$

Structure	Direction	SOC	New direction	Non-SOC		SOC	Non-SOC
$KAlTe_2$	Γ → Y	-0.471		-0.367	m_h^*	0.58	0.88
	Γ → V	-0.5		-0.802	m_e^*	2.57	2.48
	Γ → A	-0.939		-0.965			
	Y → Γ	5.141		5.141			
	Y → V	1.711		1.631			
$KGaTe_2$	Γ → Y	-0.452		-0.342	m_h^*	0.51	0.68
	Γ → V	-0.455		-0.545	m_e^*	1.00	0.97
	Γ → A	-0.657		-0.894			
	Y → Γ	1.083		1.075			
	Y → V	0.924		0.877			
$KInTe_2$	(0.22,0,0) → Γ	-1.027		-0.991	m_h^*	0.90	0.89
	(0.22,0,0) → V	-0.808		-0.803	m_e^*	0.28	0.28
	Y → Γ	0.284		0.278			
	Y → V	0.284		0.278			
$RbAlTe_2$	(0.05,0,0) → Γ	-0.851	Γ → Y	-0.744	m_h^*	0.84	1.59
	(0.05,0,0) → V	-0.831	Γ → V	-2.082	m_e^*	0.41	0.40
			Γ → A	-1.29			
	(0.5,0,0.27) → V	0.35		0.339			
	(0.5,0,0.27) → L	0.484		0.496			
$RbGaTe_2$	Γ → Y	-0.363		-0.26	m_h^*	0.51	0.77
	Γ → V	-0.422		-0.594	m_e^*	2.22	2.15
	Γ → A	-1.259		-1.111			
	Y → Γ	2.304		2.268			
	Y → V	2.149		2.049			
$CsGaTe_2$	Γ → Y	-0.362		-0.291	m_h^*	0.54	0.58
	Γ → V	-0.422		-1.028	m_e^*	0.58	0.57
	Γ → A	-2.307		-1.315			
	(0.36,0.36,0.5) → M	0.572		0.583			
	(0.36,0.36,0.5) → A	0.585		0.566			
$CsInTe_2$	Γ → Y	-0.362	(0,0,0.18) → A	-1.441	m_h^*	0.55	1.64
	Γ → V	-0.451	(0,0,0.18) → Γ	-1.906	m_e^*	1.54	1.49
	Γ → A	-1.95					
	Y → Γ	1.396		1.374			
	Y → V	1.714		1.637			

Table C.3: $C2/c_{32}$

Structure	Direction	SOC	New direction	Non-SOC		SOC	Non-SOC
$CsGaTe_2$	Γ → Y	-0.267		-0.486	m_h^*	0.40	0.78
	Γ → V	-0.3		-0.565	m_e^*	1.12	1.12
	Γ → A	-2.118		-83.89			
	(0,0,0.18) → A	0.999		0.966			
	(0,0,0.18) → Γ	1.267		1.344			
$CsInTe_2$	Γ → Y	-0.278		-0.534	m_h^*	0.40	0.90
	Γ → V	-0.307		-0.699	m_e^*	0.20	0.20
	Γ → A	-1.43		-41.046			
	Γ → Y	0.168		0.17			
	Γ → V	0.172		0.173			
	Γ → A	0.303		0.308			
$KAlTe_2$	Γ → Y	-2.276		-0.584	m_h^*	2.42	0.89
	Γ → V	-1.718		-0.609	m_e^*	0.51	0.49
	Γ → A	-4.571		-59.42			
	Γ → Y	0.366		0.345			
	Γ → V	0.38		0.372			
	Γ → A	2.155		2.101			
$KGaTe_2$	Γ → Y	-0.281		-0.54	m_h^*	0.39	0.84
	Γ → V	-0.3		-0.584	m_e^*	0.42	0.41
	Γ → A	-1.298		-92.033			
	Γ → Y	0.317		0.29			
	Γ → V	0.313		0.293			
	Γ → A	1.298		2.125			
$RbAlTe_2$	(0.02,0,0) → V	-0.772	Γ → Y	-0.573	m_h^*	0.77	0.87
			Γ → V	-0.589	m_e^*	0.26	0.26
			Γ → A	- 1.00E+99			
	Γ → Y	0.211		0.204			
	Γ → V	0.216		0.215			
	Γ → A	0.483		0.491			
$RbGaTe_2$	Γ → Y	-0.263		-0.52	m_h^*	0.38	0.81
	Γ → V	-0.29		-0.567	m_e^*	1.50	2.94
	Γ → A	-1.489		- 1.00E+99			
	(0,0,0.08)→A	1.5	(0,0,0.04) → A	2.943			
$RbInTe_2$	Γ → Y	-0.271		-0.606	m_h^*	0.38	1.05
	Γ → V	-0.292		-0.864	m_e^*	0.19	0.19
	Γ → A	-1.25		-24.922			
	Γ → Y	0.158		0.16			
	Γ → V	0.163		0.163			
	Γ → A	0.286		0.291			

Table C.4: $I\bar{4}2d$

Structure	Direction	SOC	New direction	Non-SOC		SOC	Non-SOC
$LiAlTe_2$	(0,0,0.01) → X	-0.436	Γ → X	-0.616	m_h^*	0.44	0.38
			Γ → N	-0.516	m_e^*	0.40	0.40
			Γ → Z	-0.227			
	Γ → X	0.341		0.344			
	Γ → N	0.365		0.365			
	Γ → Z	0.523		0.518			
$LiGaTe_2$	Γ → X	-0.653		-0.525	m_h^*	0.35	0.31
	Γ → N	-0.583		-0.433	m_e^*	0.48	0.43
	Γ → Z	-0.184		-0.183			
	Z → Γ	0.476	(0.48,0.48,0.48) → Γ	0.426			
$LiInTe_2$	Γ → X	-0.193		-0.185	m_h^*	0.29	0.34
	Γ → N	-0.341		-0.61	m_e^*	0.20	0.20
	Γ → Z	-0.43		-0.577			
	Γ → X	0.205		0.219			
	Γ → N	0.198		0.19			
	Γ → Z	0.202		0.197			

Table C.5: $I\bar{4}2d$

Structure	Direction	SOC	Non-SOC	Total	SOC	Non-SOC
$LiAlTe_2$	Γ → Z	-0.947	-1.466	m_h^*	0.38	0.49
	Γ → X	-0.205	-0.205	m_e^*	0.24	0.23
	Γ → Y	-0.514	-1.84			
	(-0.37,0,0) → Y	0.189	0.189			
	(-0.37,0,0) → Γ	0.324	0.302			
$LiGaTe_2$	Γ → Z	-0.728	-1.192	m_h^*	0.31	0.41
	Γ → X	-0.166	-0.171	m_e^*	0.27	0.23
	Γ → Y	-0.46	-1.478			
	(-0.37,0,0) → Y	0.226	0.222			
	(-0.37,0,0) → Γ	0.342	0.234			
$LiInTe_2$	Γ → Z	-0.717	-1.506	m_h^*	0.42	0.45
	Γ → X	-0.22	-0.187	m_e^*	0.21	0.21
	Γ → Y	-0.806	-1.509			
	Γ → Z	0.2	0.207			
	Γ → X	0.259	0.264			
	Γ → Y	0.184	0.182			

D Orbital contributions of DOS at VBM and CBM

Here, the orbital contributions for the DOS at the VBM and CBM for each compound are listed in Table D

Table D.1: Numerical values of orbital contributions at band extrema

Structure	Space group	Orbital	VBM			CBM		
			A	B	Te	A	B	Te
$LiAlTe_2$	$I\bar{4}2d$	s	0	0	0	0	0	21
		p	1	2	97	10	32	6
		d	0	0	1	0	0	32
	$Pna2_1$	s	0	0	0	1	35	17
		p	1	2	97	2	7	25
		d	0	0	0	0	0	13
$LiGaTe_2$	$I\bar{4}2d$	s	0	0	0	1	42	11
		p	1	5	88	2	3	36
		d	6	0	0	0	1	4
	$Pna2_1$	s	0	0	0	0	43	7
		p	1	5	88	1	5	36
		d	0	5	0	0	2	6
$LiInTe_2$	$I\bar{4}2d$	s	0	0	0	2	37	26
		p	1	5	86	0	0	34
		d	0	8	0	0	0	0
	$Pna2_1$	s	0	0	0	2	37	26
		p	1	5	87	0	0	34
		d	0	8	0	0	0	0
$NaAlTe_2$	$I4/mcm$	s	0	0	1	2	61	0
		p	0	2	96	0	0	25
		d	0	0	0	0	0	12
$KAlTe_2$	$I4/mcm$	s	0	0	0	3	54	0
		p	2	2	94	0	0	30
		d	0	0	0	2	0	11
	$C2/c_{32}$	s	0	1	0	5	44	11
		p	0	1	96	1	1	26
		d	1	0	0	1	0	12
	$C2/c_8$	s	0	1	1	3	43	0
		p	0	4	94	0	0	39
		d	0	0	1	4	0	10
$KGaTe_2$	$I4/mcm$	s	0	0	0	2	56	0
		p	3	6	87	0	1	33
		d	0	4	0	1	0	6
	$C2/c_{32}$	s	0	0	0	3	47	7
		p	1	6	87	1	0	32
		d	0	6	0	0	2	7
	$C2/c_8$	s	0	2	1	2	47	0
		p	1	10	81	0	1	42
		d	0	4	1	0	2	6

Continued on next page

Structure	Space group	Orbital	VBM			CBM		
			A	B	Te	A	B	Te
$KInTe_2$	$I4/mcm$	s	0	0	0	2	63	0
		p	1	8	85	0	1	30
		d	0	5	0	1	0	4
	$C2/c_8$	s	0	0	0	2	63	0
		p	1	8	85	0	1	29
		d	0	5	0	1	0	4
$RbAlTe_2$	$I4/mcm$	s	0	0	0	4	52	0
		p	3	2	94	0	0	31
		d	0	0	0	2	0	11
	$C2/c_{32}$	s	0	0	0	5	33	40
		p	0	1	97	1	6	10
		d	1	0	0	0	0	5
	$C2/c_8$	s	0	0	1	5	40	3
		p	1	1	96	1	5	32
		d	0	0	0	2	0	11
$RbGaTe_2$	$I4/mcm$	s	0	0	0	3	55	0
		p	3	5	87	0	1	35
		d	0	4	0	1	0	6
	$C2/c_{32}$	s	0	0	0	3	47	7
		p	1	7	86	1	1	33
		d	0	6	0	0	2	6
	$C2/c_8$	s	0	2	1	2	46	0
		p	1	8	83	0	1	44
		d	0	5	0	2	0	5
$RbInTe_2$	$I4/mcm$	s	0	0	0	2	61	0
		p	3	5	86	0	1	31
		d	0	5	0	0	1	5
	$C2/c_{32}$	s	0	0	0	4	40	26
		p	1	5	85	0	1	27
		d	0	9	0	1	1	1
$CsGaTe_2$	$C2/c_{32}$	s	0	0	0	2	46	10
		p	2	7	85	1	1	31
		d	1	5	0	1	2	5
	$C2/c_8$	s	0	0	0	2	58	0
		p	2	5	84	1	8	31
		d	0	6	0	1	0	5
$CsInTe_2$	$I4/mcm$	s	0	0	0	2	58	0
		p	5	3	85	0	1	33
		d	0	6	0	1	0	5
	$C2/c_{32}$	s	0	0	0	3	41	24
		p	1	6	83	1	1	28
		d	0	8	0	1	1	1
	$C2/c_8$	s	0	2	1	1	49	0
		p	2	6	81	1	1	41
		d	0	8	0	3	1	4

E Band diagrams

In the following section all of the calculated band diagrams are provided. They are grouped together in terms of space groups for an easy comparison. For each compound both the diagrams with and without spin-orbit coupling are provided. They are provided in order: $I\bar{4}2d$, $Pna2_1$, $I4/mcm$, $C2/c_8$, $C2/c_{32}$.

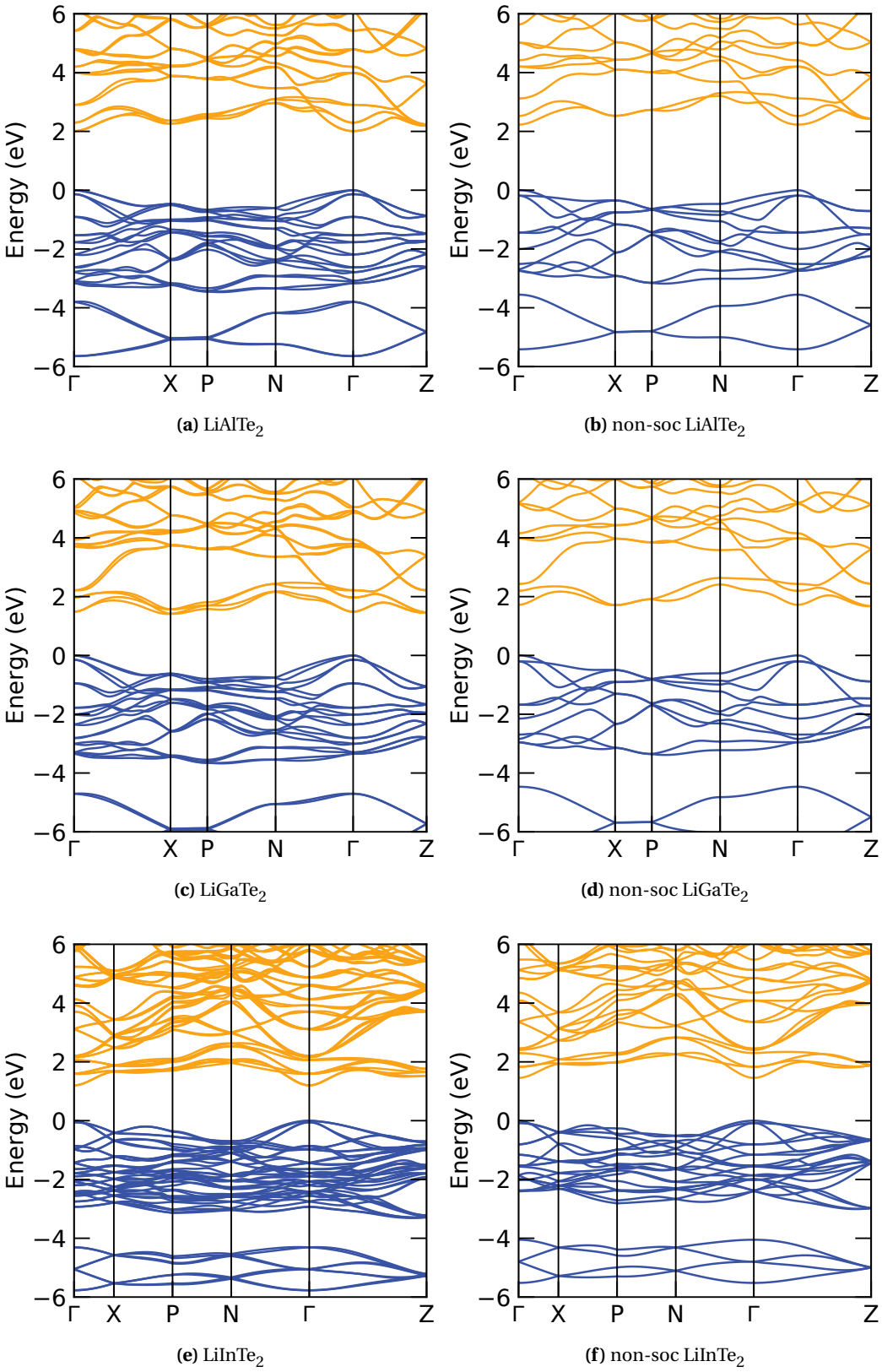

(a) $LiAlTe_2$ **(b)** non-soc $LiAlTe_2$

(c) $LiGaTe_2$ **(d)** non-soc $LiGaTe_2$

(e) $LiInTe_2$ **(f)** non-soc $LiInTe_2$

Figure E.1: Band diagrams for all the tetragonal $I\bar{4}2d$ structures.

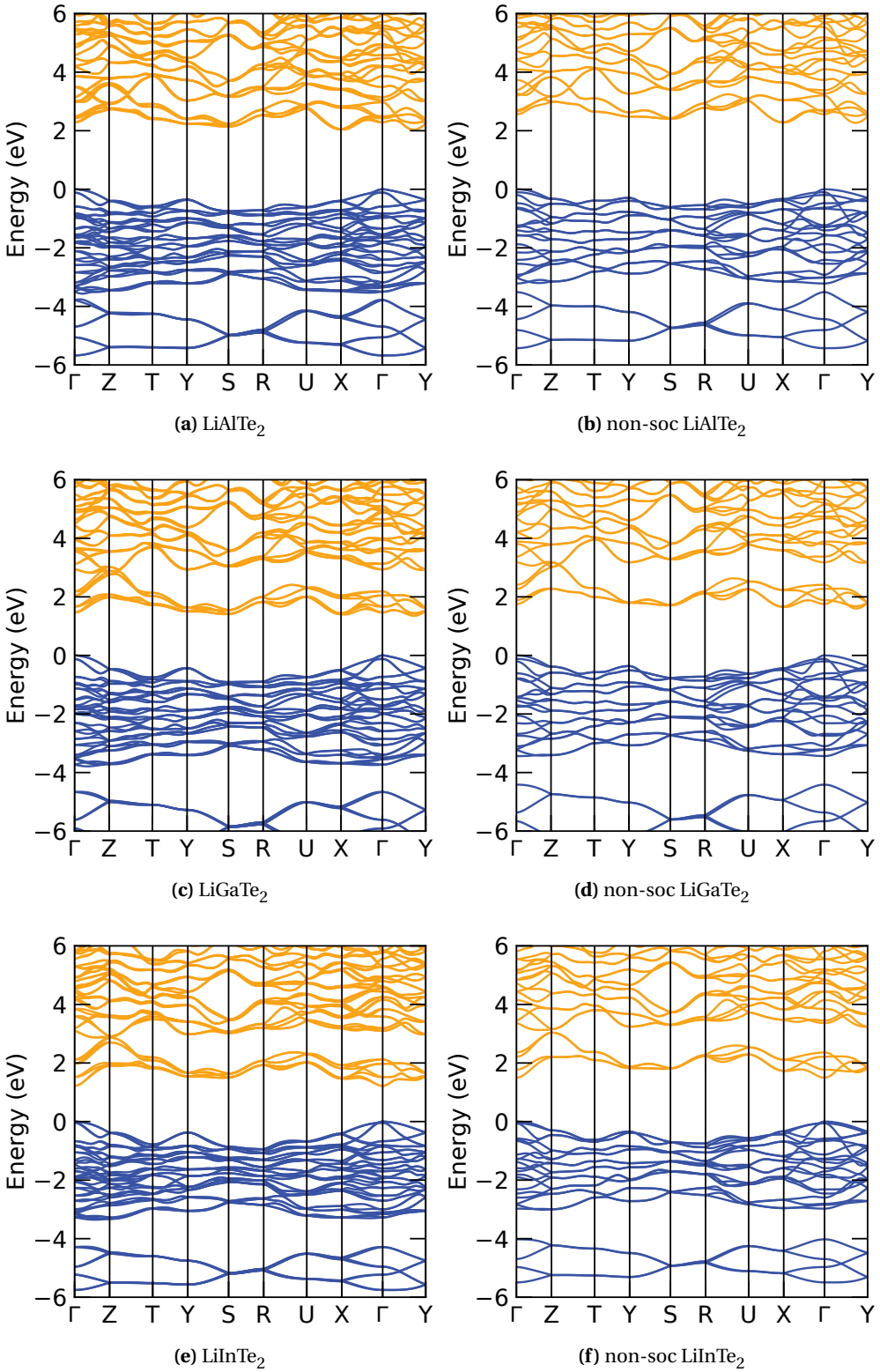

(a) $LiAlTe_2$ **(b)** non-soc $LiAlTe_2$

(c) $LiGaTe_2$ **(d)** non-soc $LiGaTe_2$

(e) $LiInTe_2$ **(f)** non-soc $LiInTe_2$

Figure E.2: Band diagrams for all the orthorombic $Pna2_1$ structures.

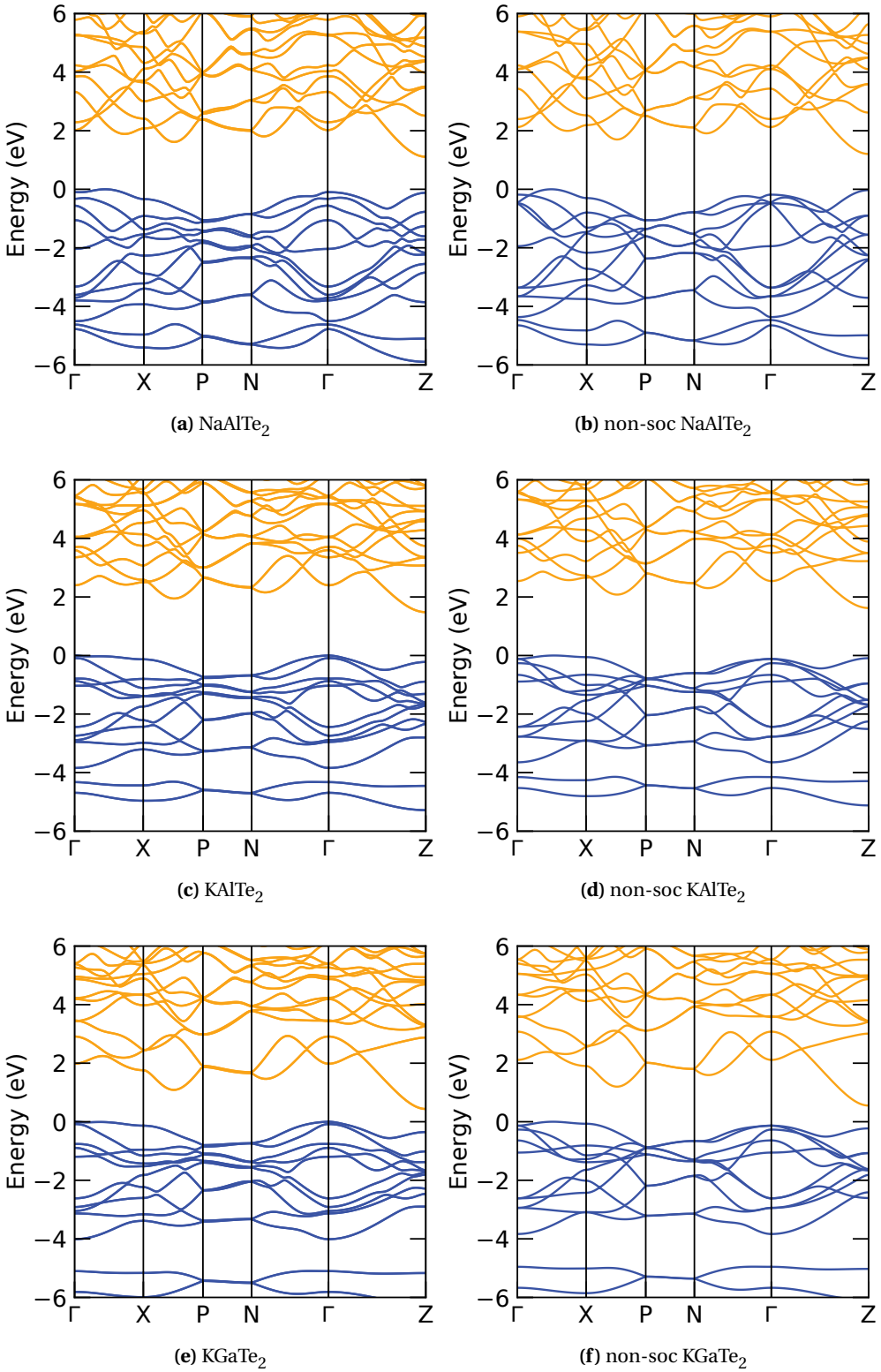

(a) $NaAlTe_2$ **(b)** non-soc $NaAlTe_2$

(c) $KAlTe_2$ **(d)** non-soc $KAlTe_2$

(e) $KGaTe_2$ **(f)** non-soc $KGaTe_2$

Figure E.3: Band diagrams for the first of the $I4/mcm$ structures.

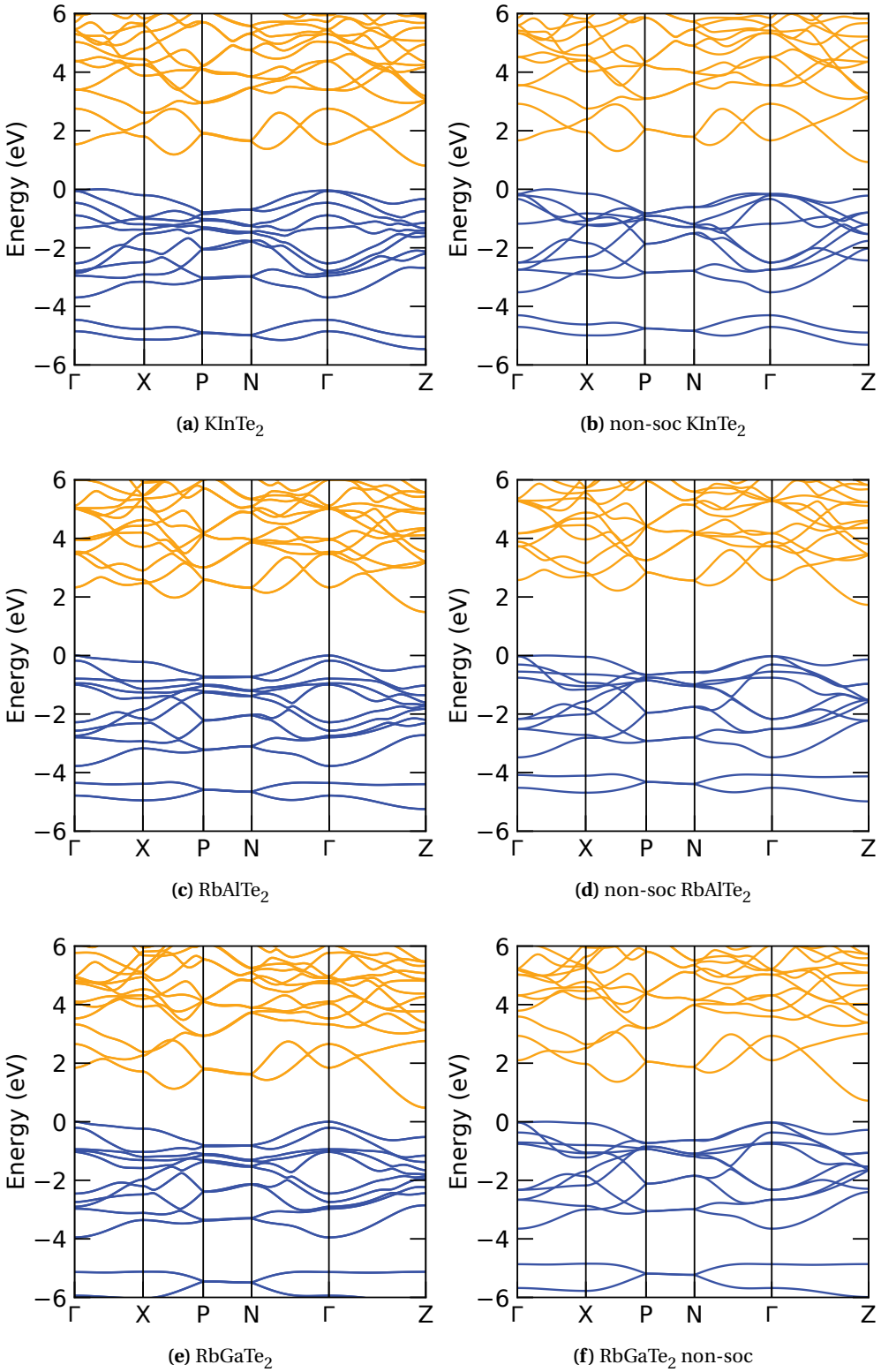

(a) $KInTe_2$ **(b)** non-soc $KInTe_2$

(c) $RbAlTe_2$ **(d)** non-soc $RbAlTe_2$

(e) $RbGaTe_2$ **(f)** $RbGaTe_2$ non-soc

Figure E.4: Band diagrams for the second part of the tetragonal $I4/mcm$ structures

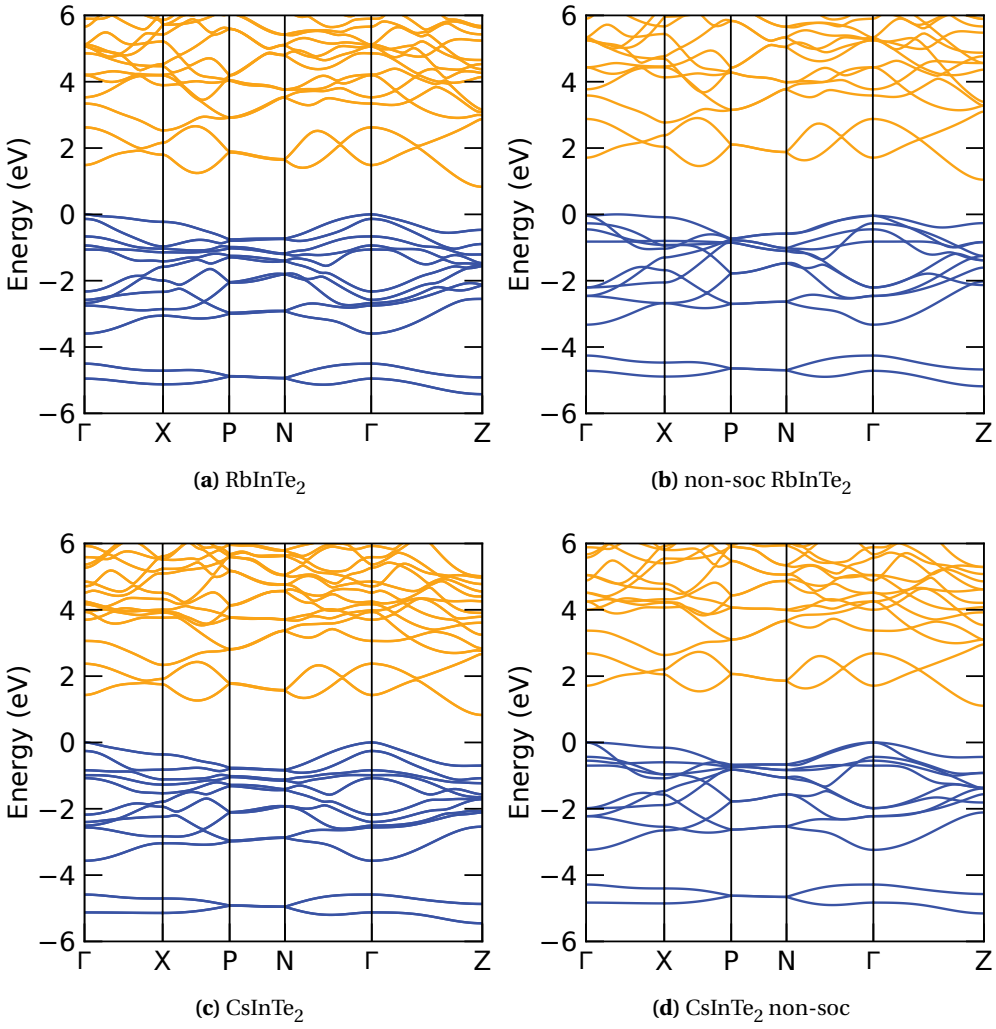

(a) $RbInTe_2$ **(b)** non-soc $RbInTe_2$

(c) $CsInTe_2$ **(d)** $CsInTe_2$ non-soc

Figure E.5: Band diagrams for the last part of the tetragonal $I4/mcm$ structures

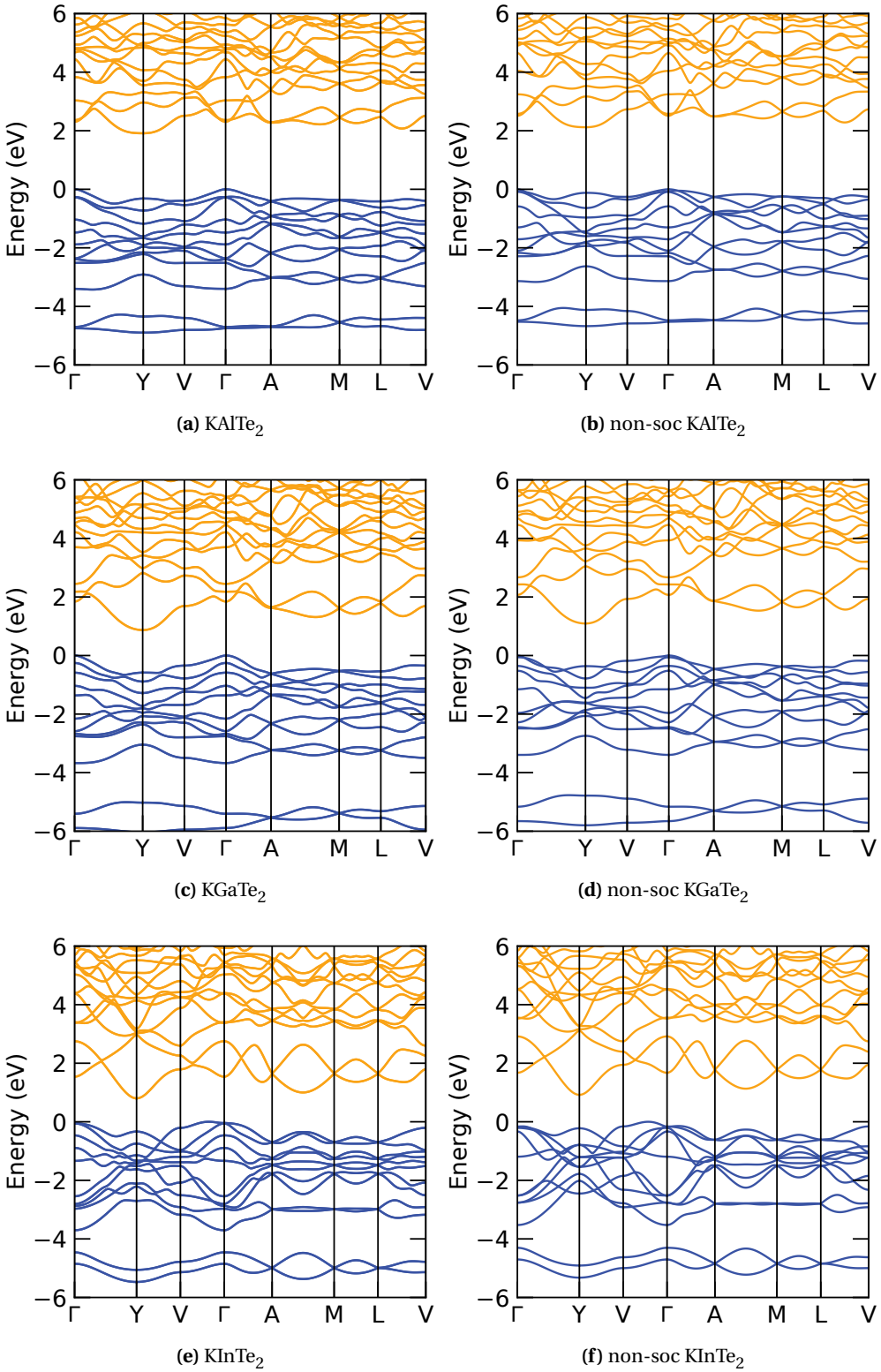

(a) $KAlTe_2$ **(b)** non-soc $KAlTe_2$

(c) $KGaTe_2$ **(d)** non-soc $KGaTe_2$

(e) $KInTe_2$ **(f)** non-soc $KInTe_2$

Figure E.6: Band diagrams for the first of the monoclinic $C2/c_8$ structures.

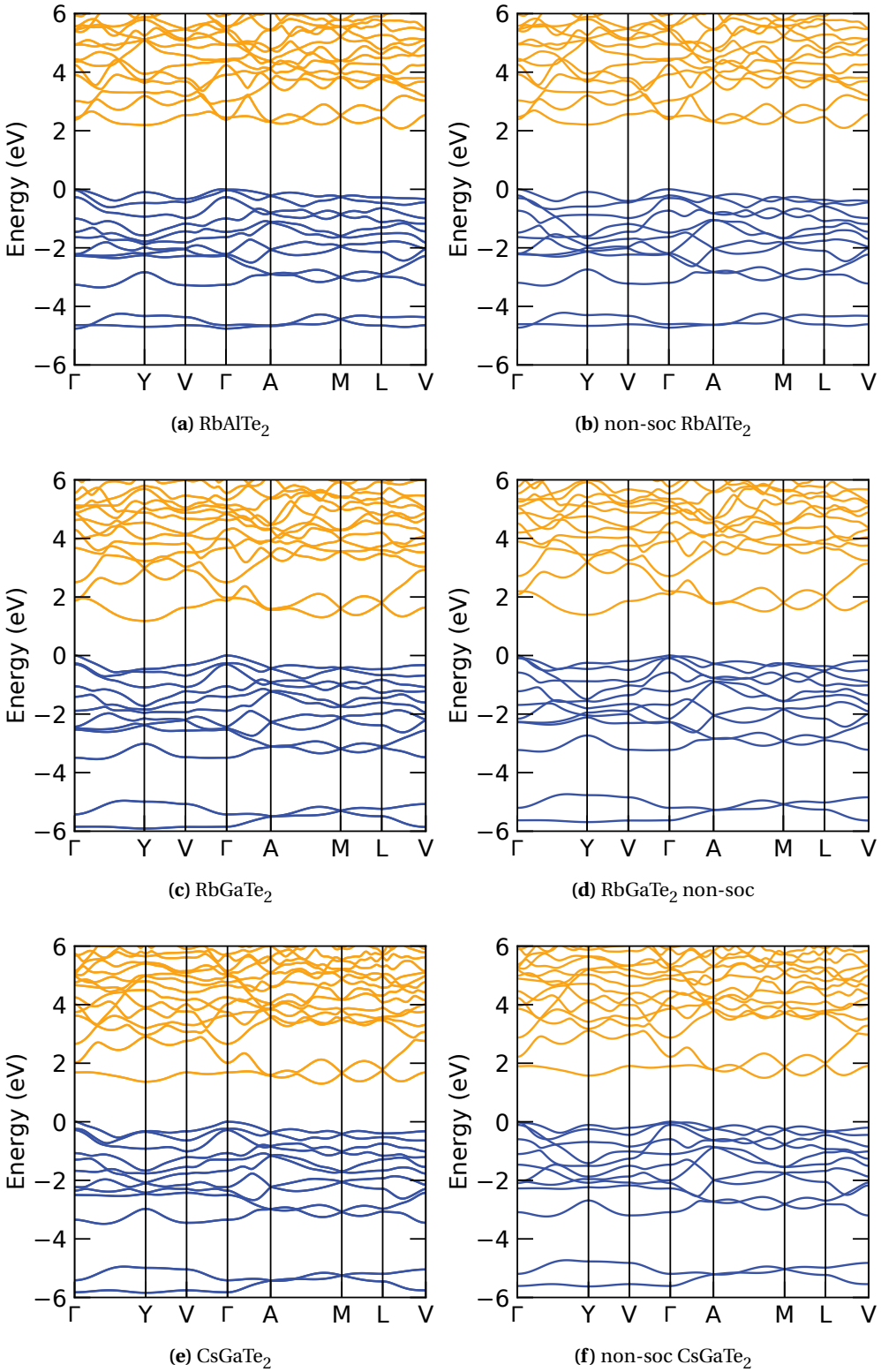

(a) $RbAlTe_2$ **(b)** non-soc $RbAlTe_2$

(c) $RbGaTe_2$ **(d)** $RbGaTe_2$ non-soc

(e) $CsGaTe_2$ **(f)** non-soc $CsGaTe_2$

Figure E.7: Band diagrams for the second part of the monoclinic $C2/c_8$ structures

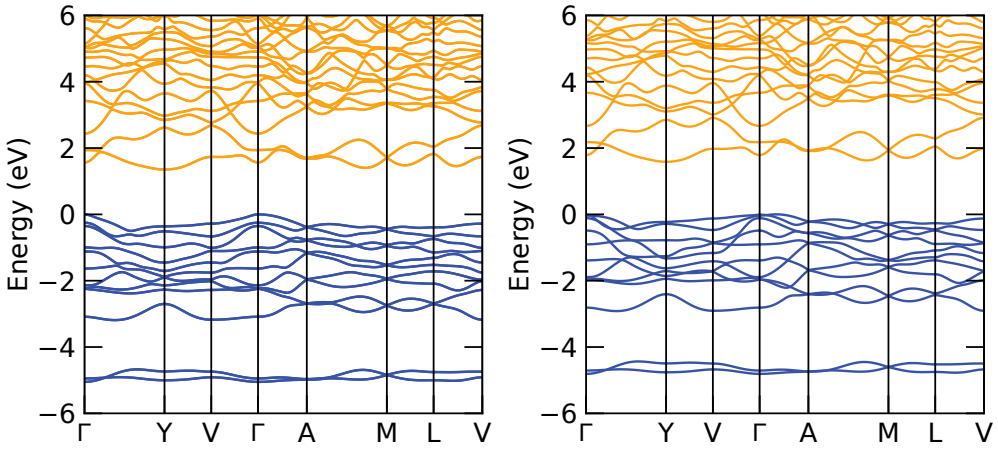

(a) $CsGaTe_2$ **(b)** non-soc $CsInTe_2$

Figure E.8: Band diagrams for the last part of the monoclinic $C2/c_8$ structures

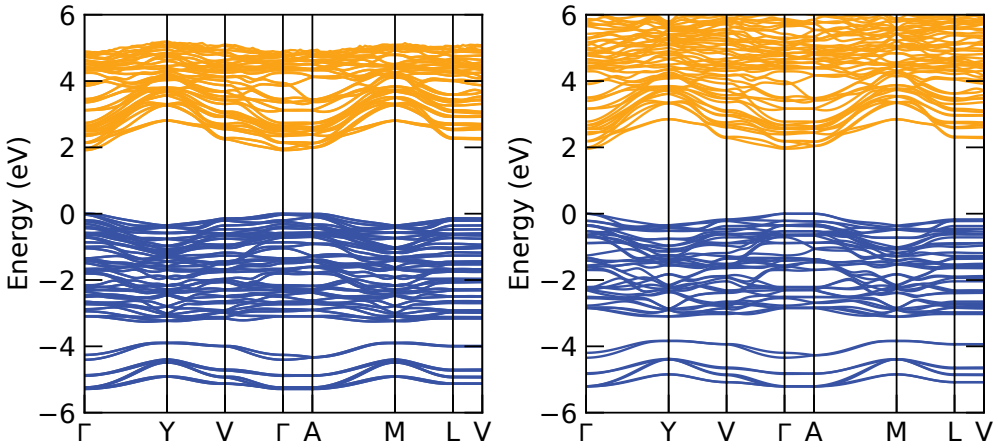

(a) $KAlTe_2$ **(b)** non-soc $KAlTe_2$

Figure E.9: Band diagrams for the first of the monoclinic $C2/c_{32}$ structures.

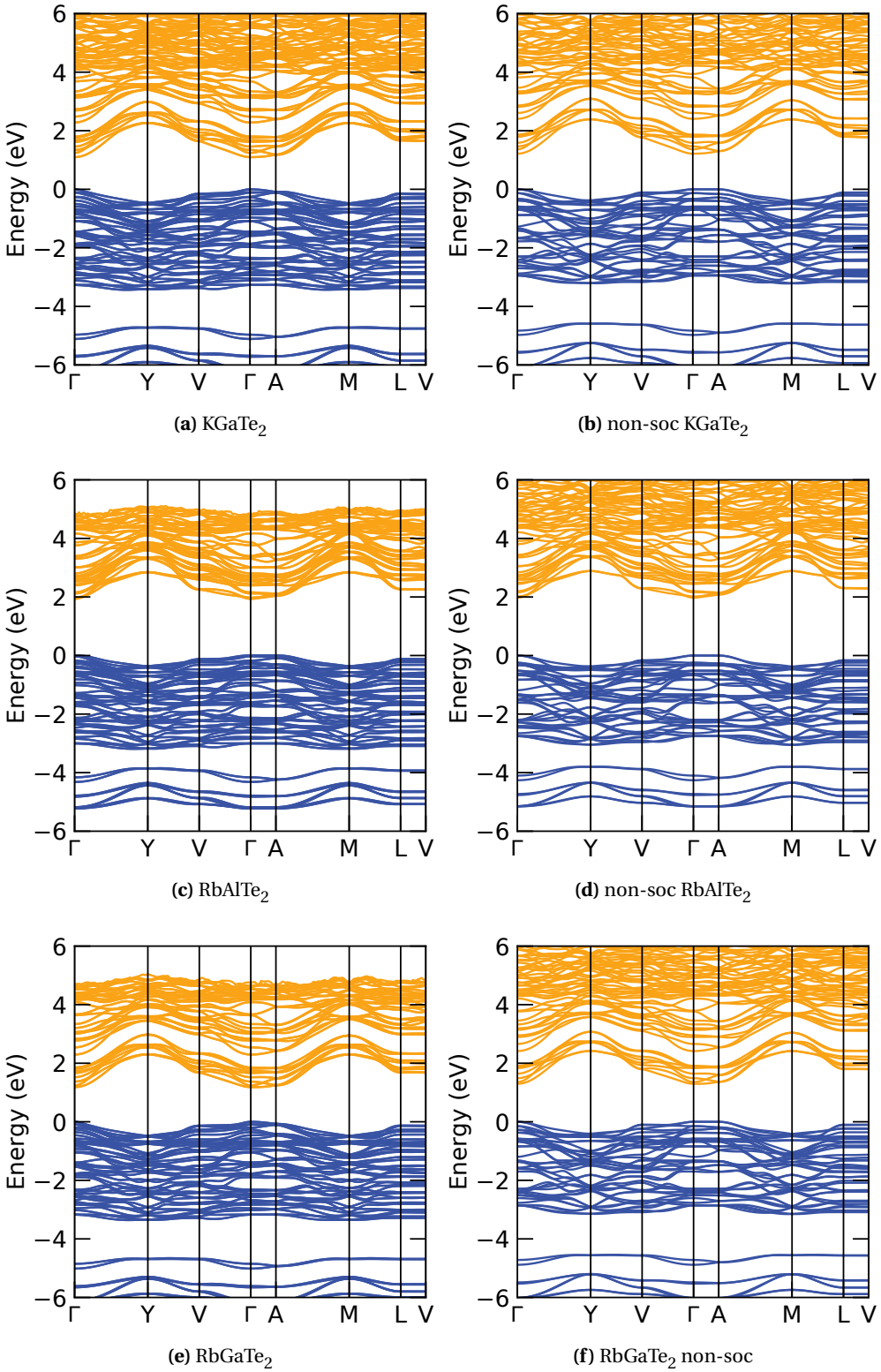

(a) $KGaTe_2$ **(b)** non-soc $KGaTe_2$

(c) $RbAlTe_2$ **(d)** non-soc $RbAlTe_2$

(e) $RbGaTe_2$ **(f)** $RbGaTe_2$ non-soc

Figure E.10: Band diagrams for the second part of the monoclinic $C2/c_{32}$ structures

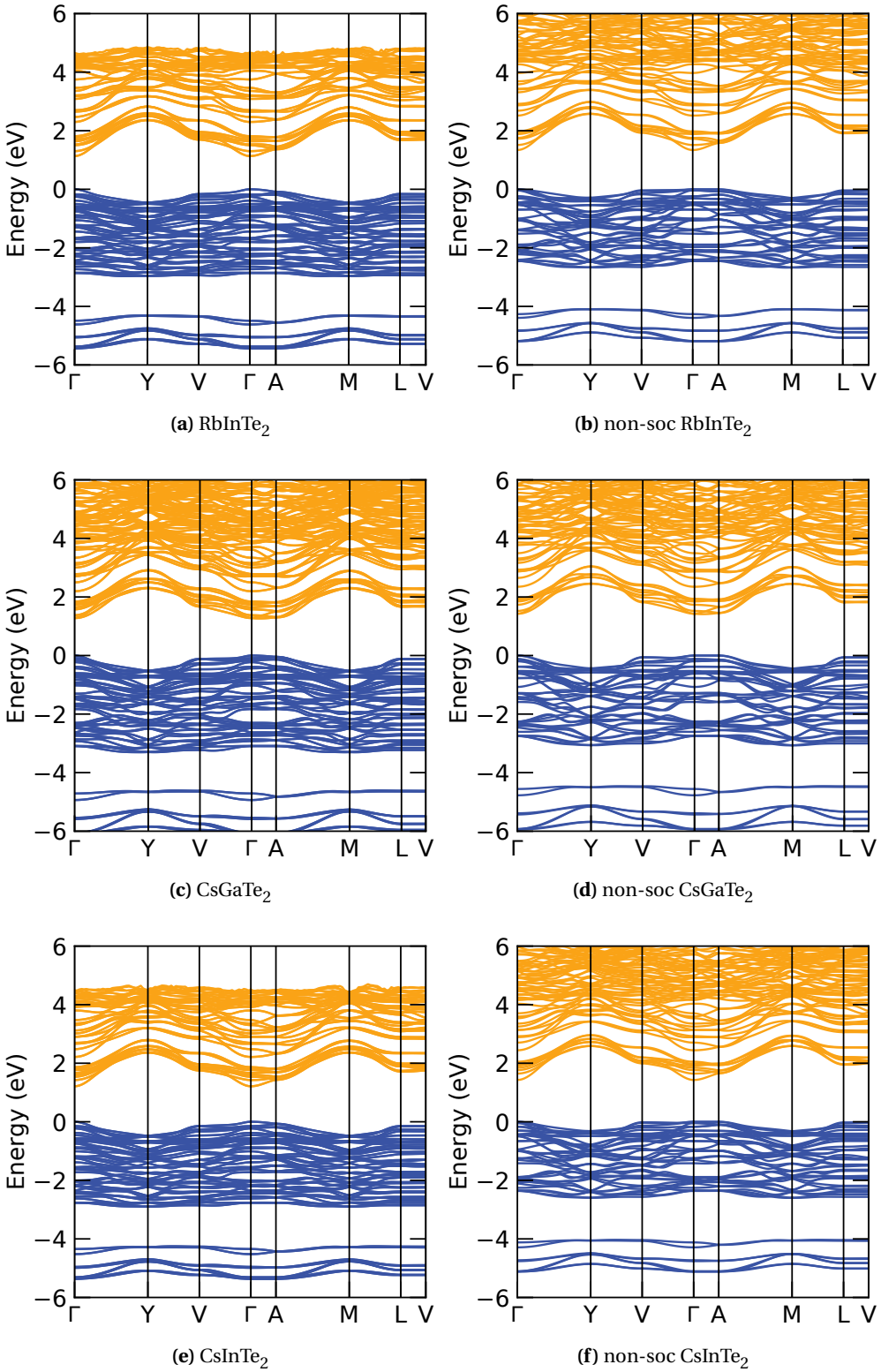

(a) $RbInTe_2$ **(b)** non-soc $RbInTe_2$

(c) $CsGaTe_2$ **(d)** non-soc $CsGaTe_2$

(e) $CsInTe_2$ **(f)** non-soc $CsInTe_2$

Figure E.11: Band diagrams for the last part of the monoclinic $C2/c_{32}$ structures

F Absorption plots

In the following appendix anisotropic absorption plots for all compounds involved in the calculations will be provided. They are all plotted with a vertical dotted line corresponding to the fundamental band gap.

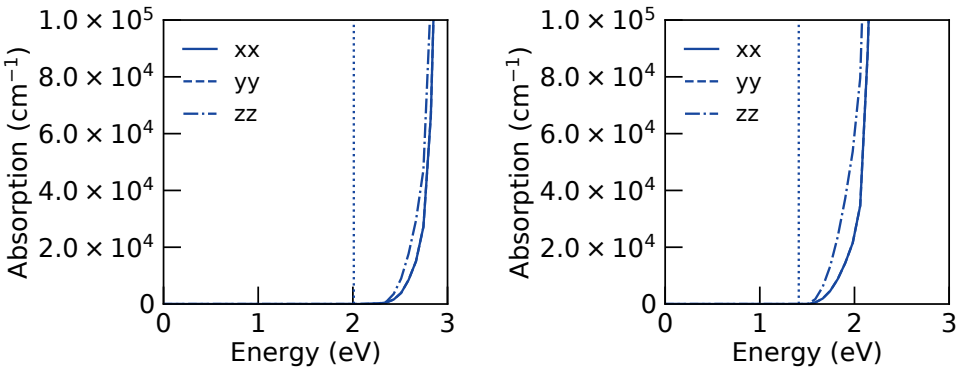

(a) $LiAlTe_2$

(b) $LiGaTe_2$

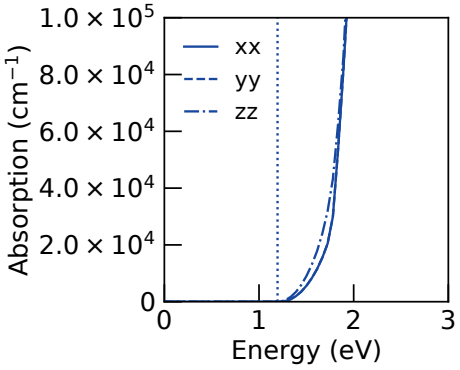

(c) $LiInTe_2$

Figure F.1: Absorption plots for all the tetragonal $I\bar{4}2d$ structures. The diagram for (**c**) differs from the other two because $LiInTe_2$ has more atoms in the cell.

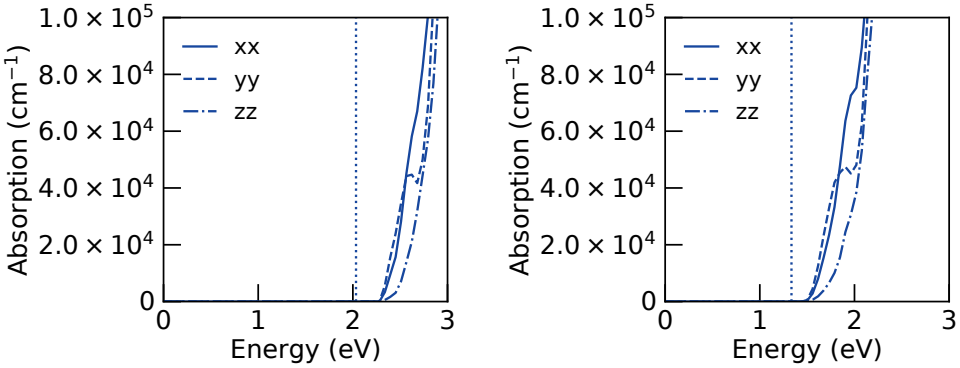

(a) $LiAlTe_2$

(b) $LiGaTe_2$

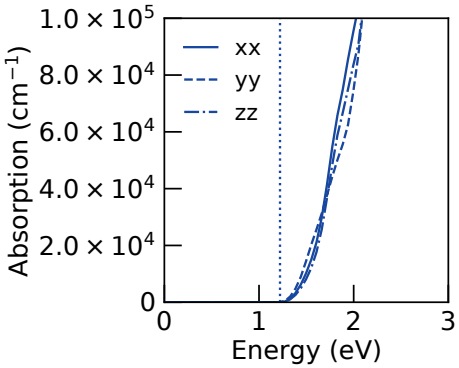

(c) $LiInTe_2$

Figure F.2: Absorption plots for all the orthorombic $Pna2_1$ structures.

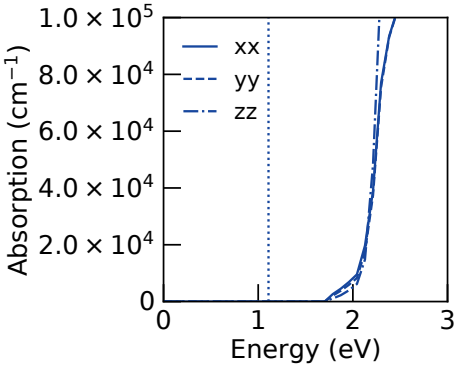

(a) $NaAlTe_2$

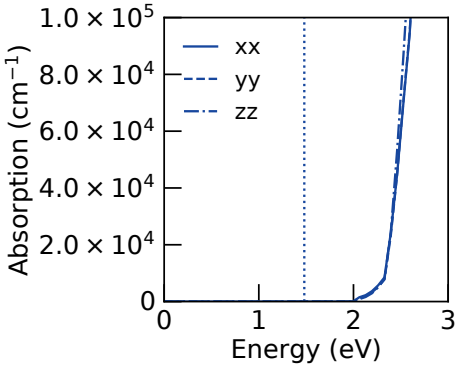

(b) $KAlTe_2$

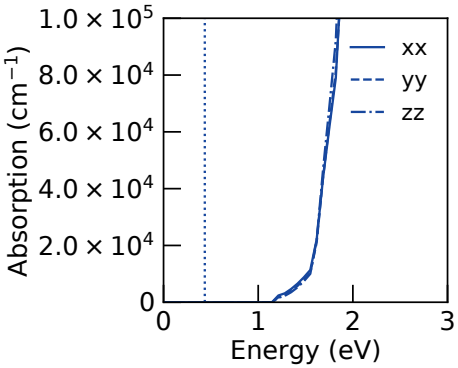

(c) $KGaTe_2$

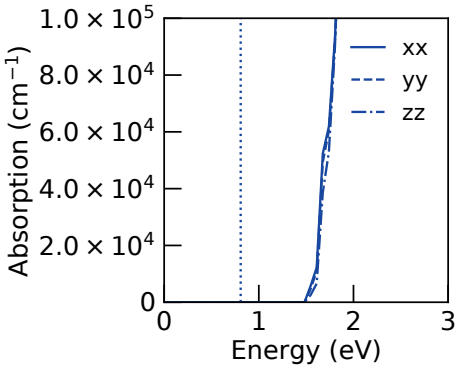

(d) $KInTe_2$

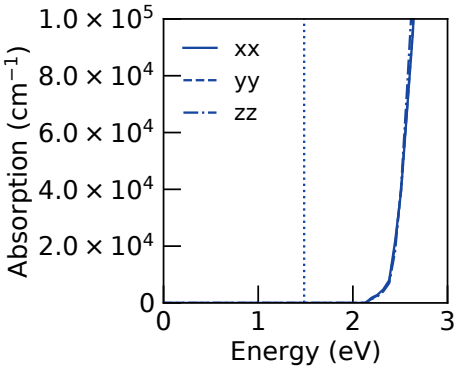

(e) $RbAlTe_2$

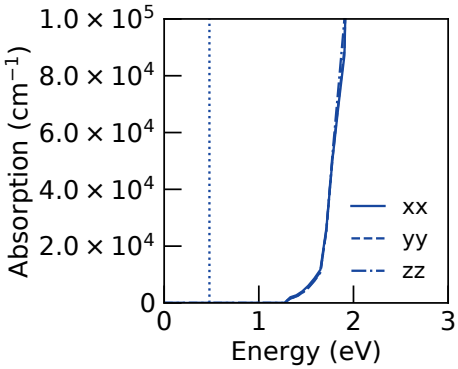

(f) $RbGaTe_2$

Figure F.3: Absorption plots for the first part of the tetragonal $I4/mcm$ structures

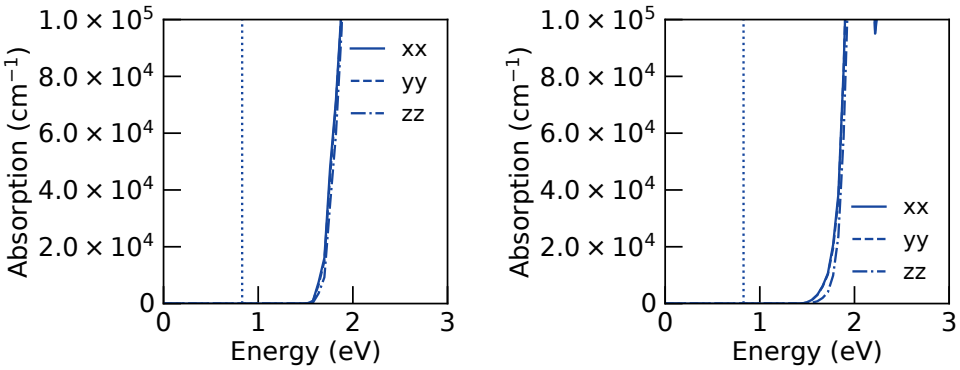

(a) $RbInTe_2$ **(b)** $CsInTe_2$

Figure F.4: Absorption plots for the last part of the tetragonal $I4/mcm$ structures

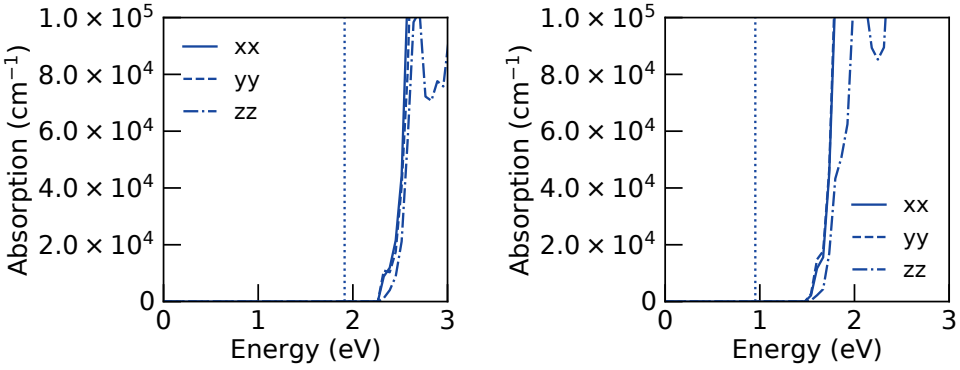

(a) $KAlTe_2$ **(b)** $KGaTe_2$

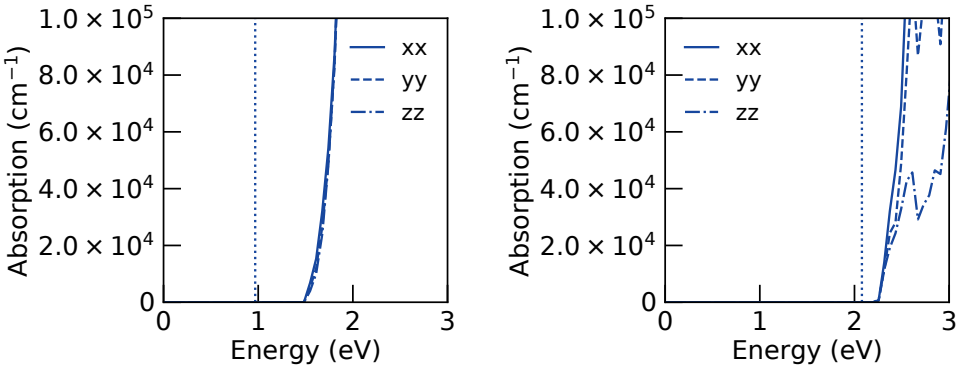

(c) $KInTe_2$ **(d)** $RbAlTe_2$

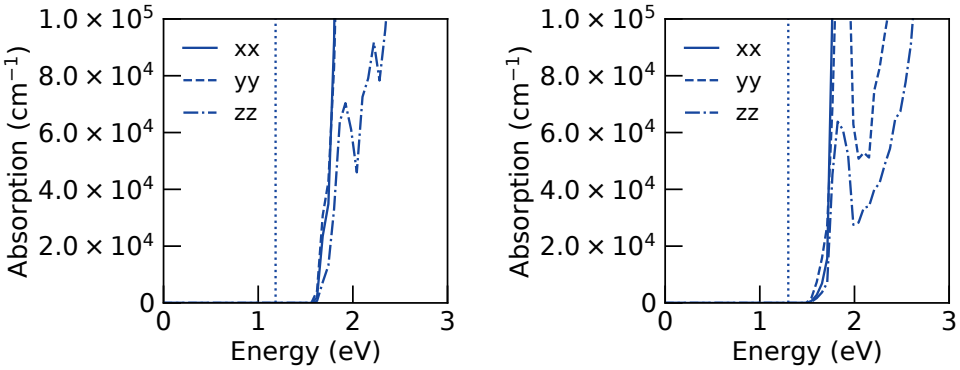

(e) $RbGaTe_2$ **(f)** $CsGaTe_2$

Figure F.5: Absorption plots for the first of the monoclinic $C2/c_8$ structures.

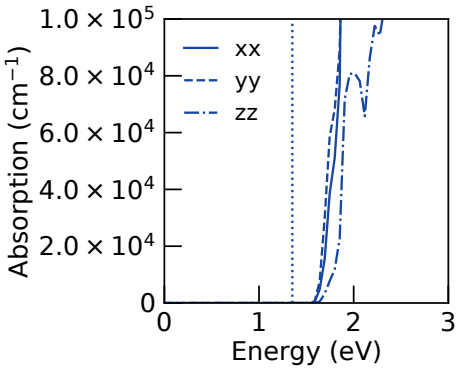

(a) $CsInTe_2$

Figure F.6: Absorption plots for the last part of the monoclinic $C2/c_8$ structures

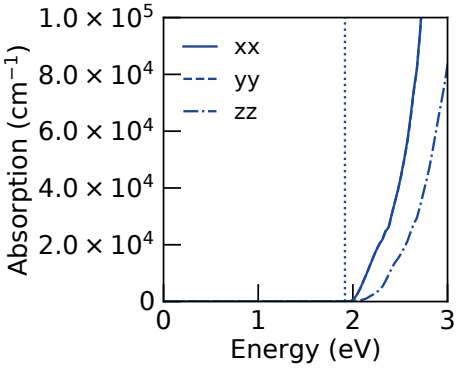

(a) $KAlTe_2$

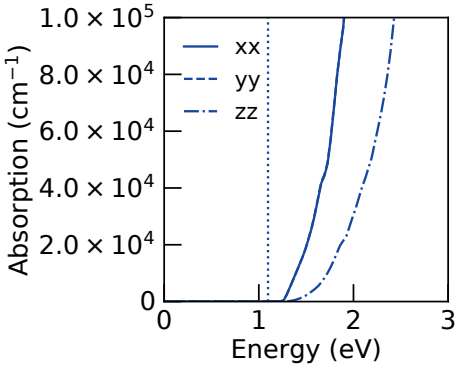

(b) $KGaTe_2$

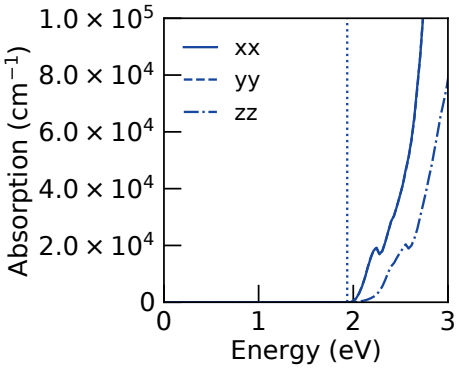

(c) $RbAlTe_2$

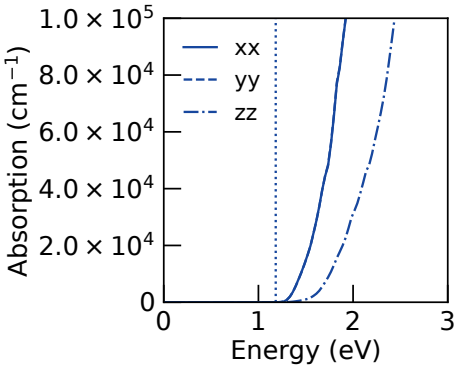

(d) $RbGaTe_2$

Figure F.7: Absorption plots for the first of the monoclinic $C2/c_{32}$ structures.

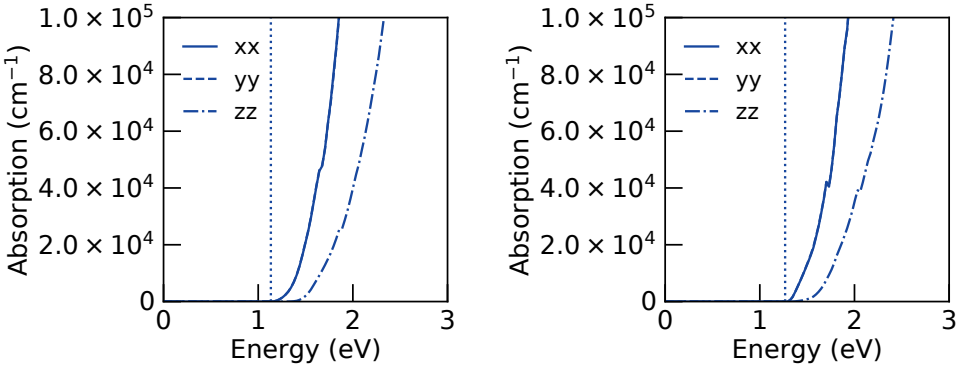

(a) $RbInTe_2$

(b) $CsGaTe_2$

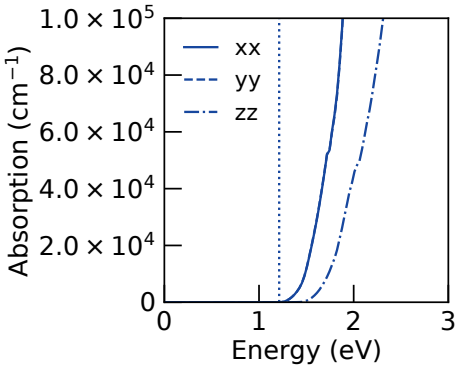

(c) $CsInTe_2$

Figure F.8: Absorption plots for the last part of the monoclinic $C2/c_{32}$ structures

G Phonon dispersion relations

In the following appendix all of the calculated phonon dispersion diagrams will be provided. The calculations were mainly run for the compounds surviving the electronic screening, but also for some additional compounds.

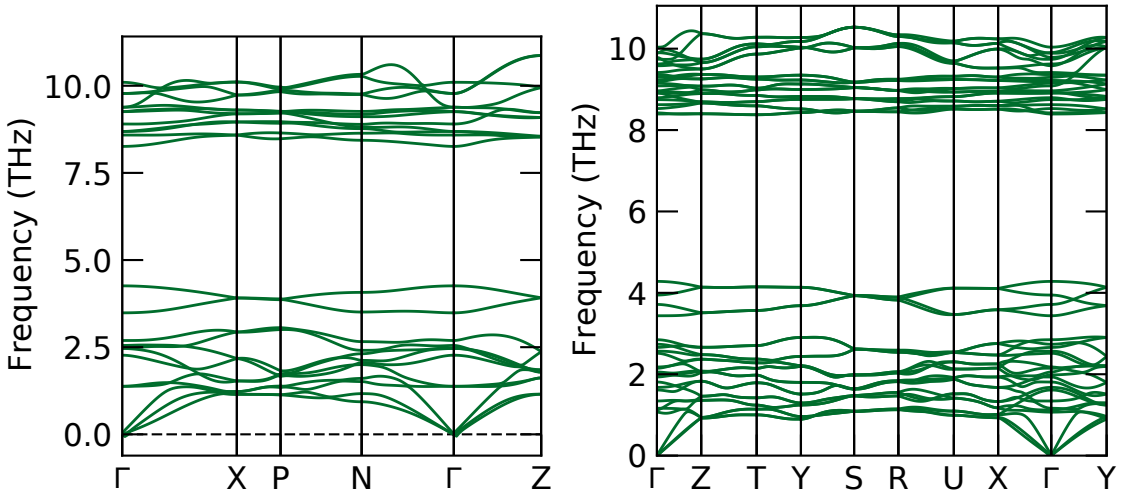

(a) $I\bar{4}2d$ $LiAlTe_2$ **(b)** $Pna2_1$ $LiAlTe_2$

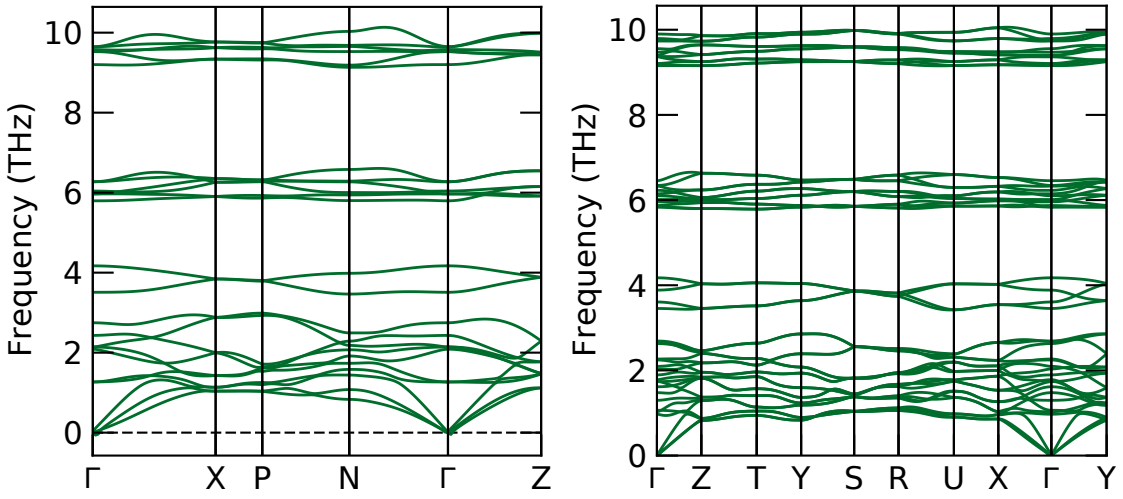

(c) $I\bar{4}2d$ $LiGaTe_2$ **(d)** $Pna2_1$ $LiGaTe_2$

Figure G.1

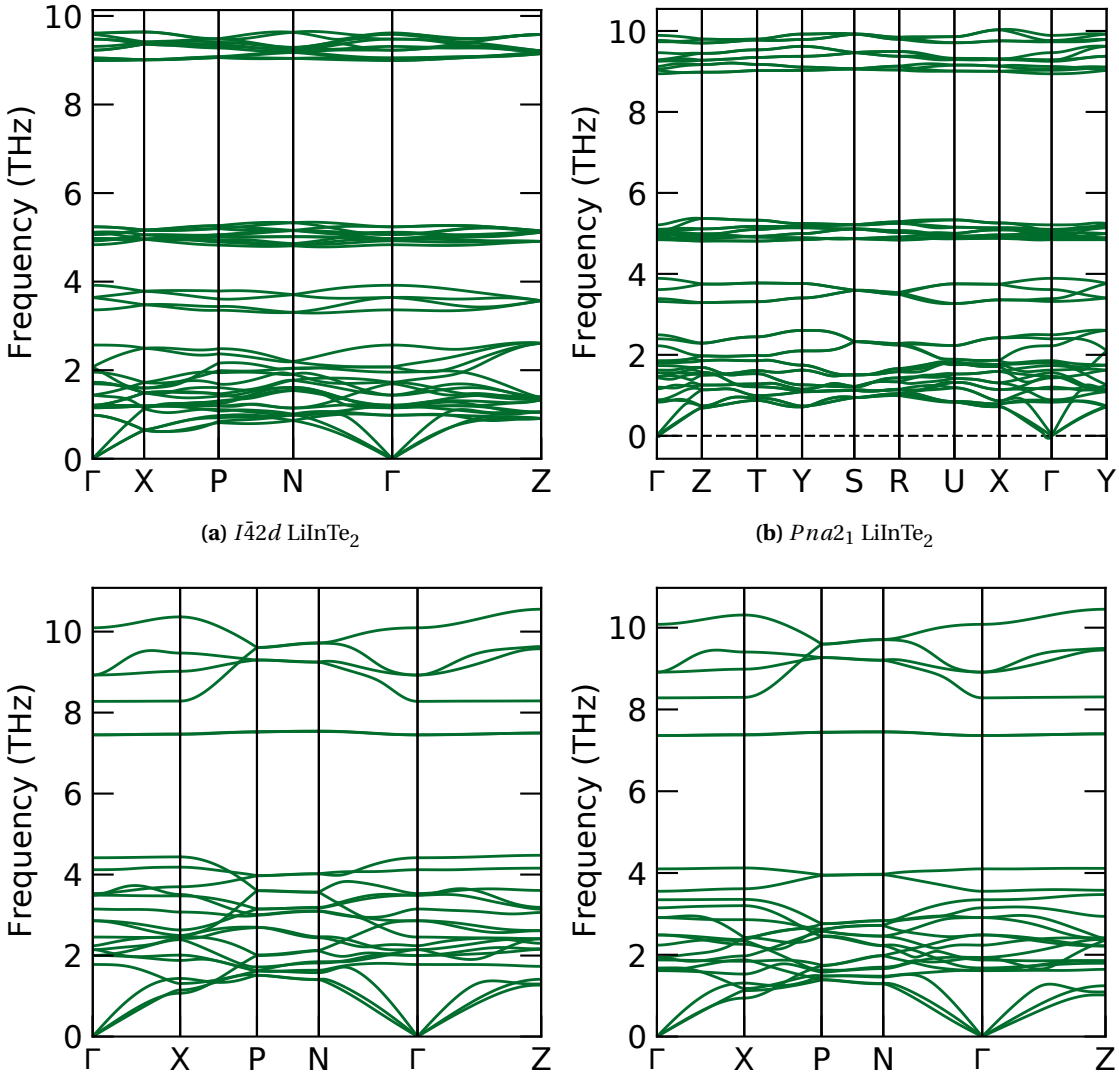

(a) $I\bar{4}2d$ $LiInTe_2$

(b) $Pna2_1$ $LiInTe_2$

(c) $I4/mcm$ $KAlTe_2$

(d) $I4/mcm$ $RbAlTe_2$

Figure G.2

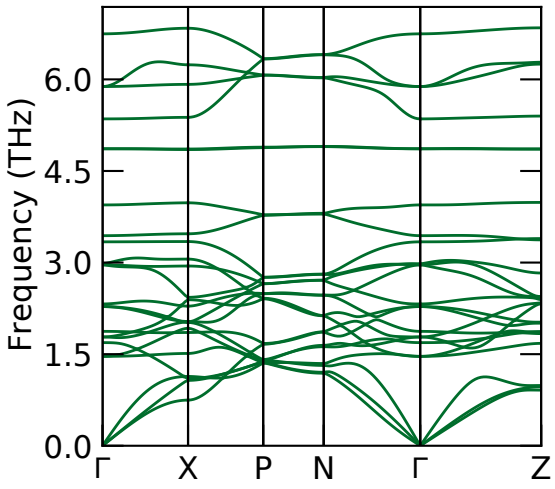

(a) $I4/mcm$ $RbGaTe_2$

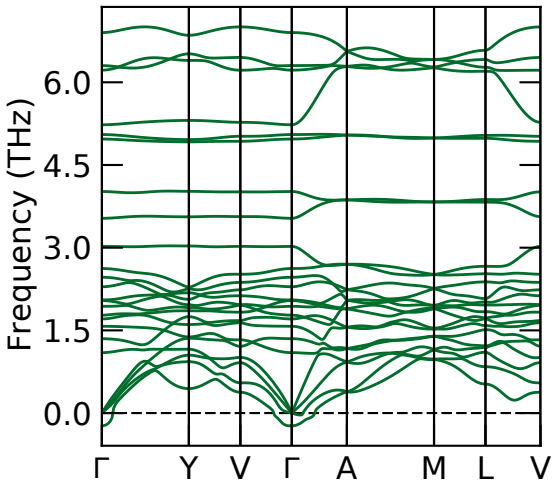

(b) $C2/c_8$ $RbGaTe_2$

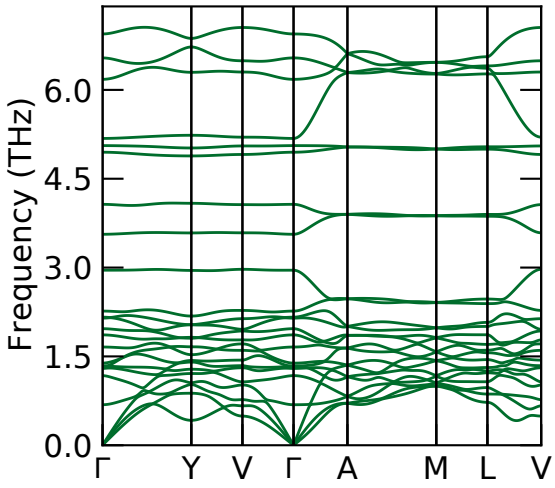

(c) $C2/c_8$ $CsGaTe_2$

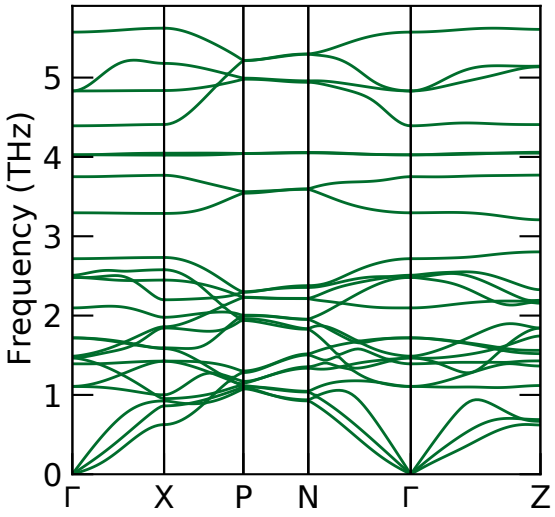

(d) $I4/mcm$ $CsInTe_2$

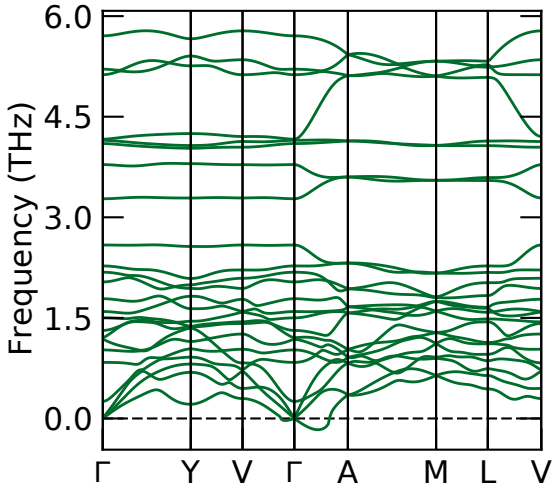

(e) $C2/c_8$ $CsInTe_2$

H DOS-plots

In the following appendix DOS-plots for all of the compounds involved in calculations will be provided. Only the contributions from the B cation and Te is taken into considerations.

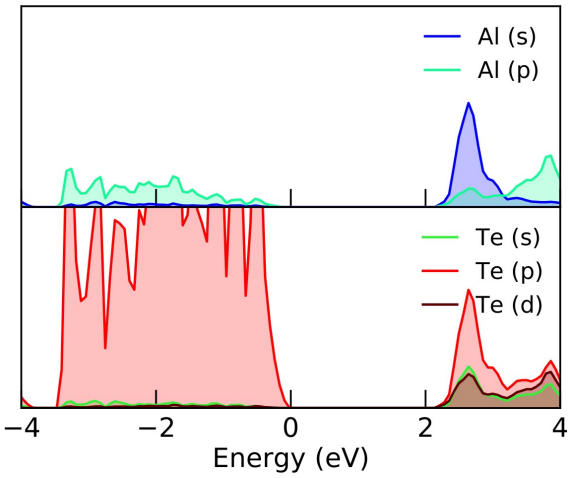

(a) $LiAlTe_2$

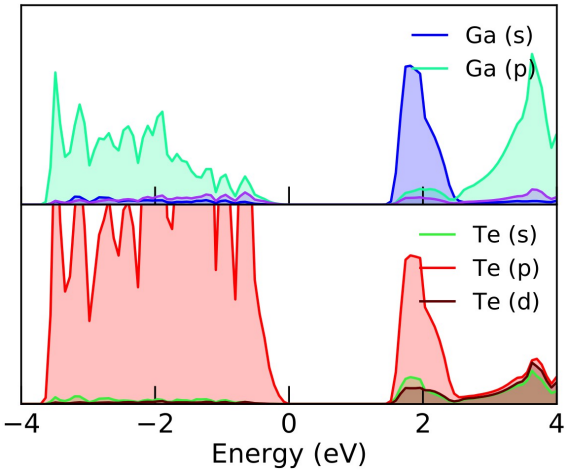

(b) $LiGaTe_2$

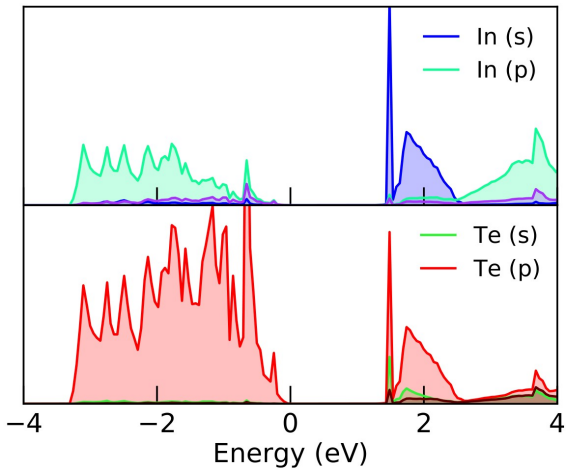

(c) $LiInTe_2$

Figure H.1: DOS plots for all the $I\bar{4}2d$ structures. The diagram for (**c**) differs from the other two because $LiInTe_2$ has more atoms in the cell.

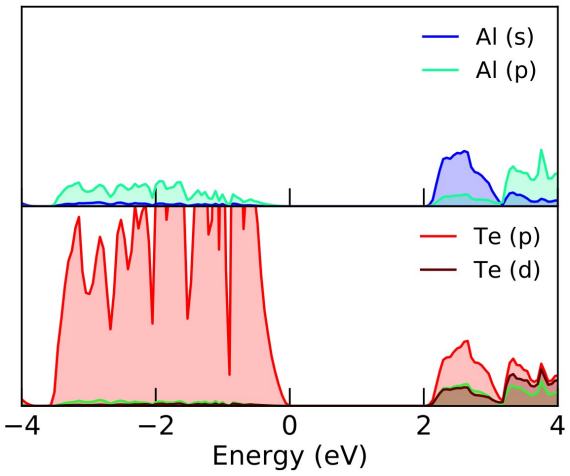

(a) $LiAlTe_2$

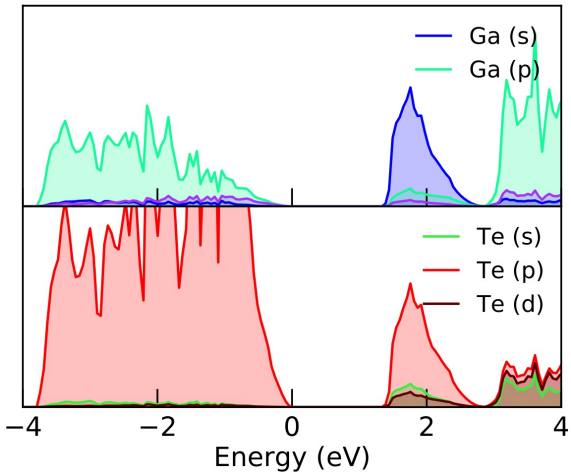

(b) $LiGaTe_2$

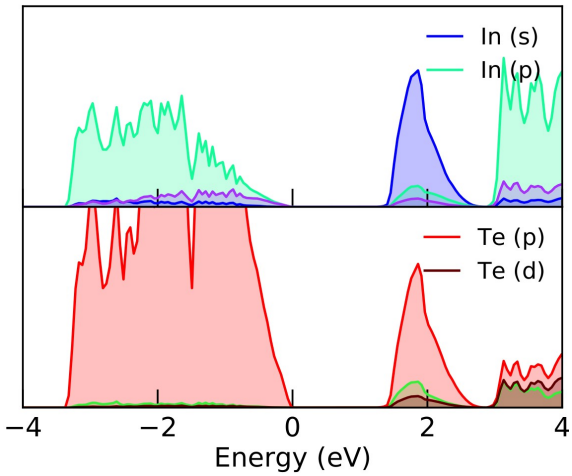

(c) $LiInTe_2$

Figure H.2: DOS plots for all the $Pna2_1$ structures.

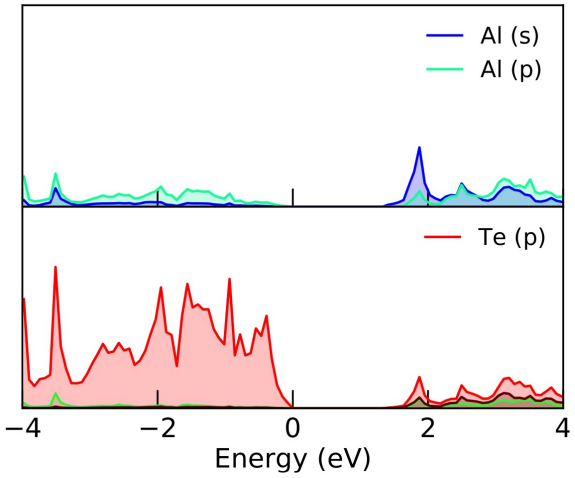

(a) $NaAlTe_2$

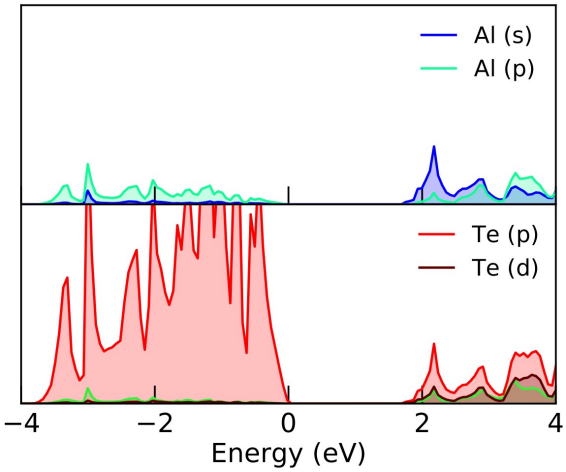

(b) $KAlTe_2$

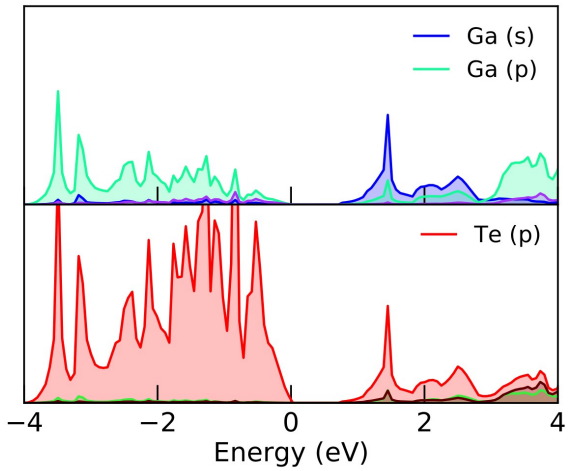

(c) $KGaTe_2$

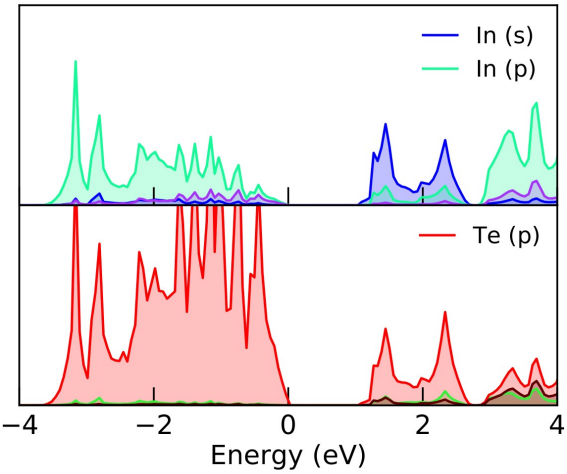

(d) $KInTe_2$

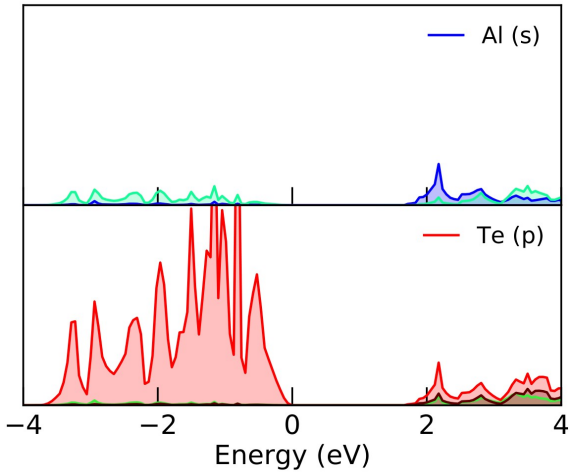

(e) $RbAlTe_2$

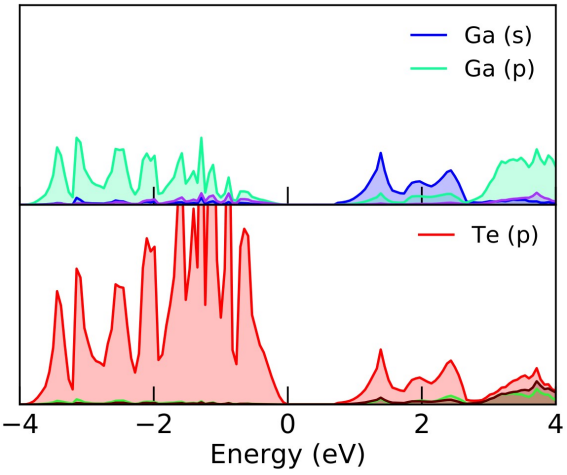

(f) $RbGaTe_2$

Figure H.3: DOS plots for the first part of the $I4/mcm$ structures

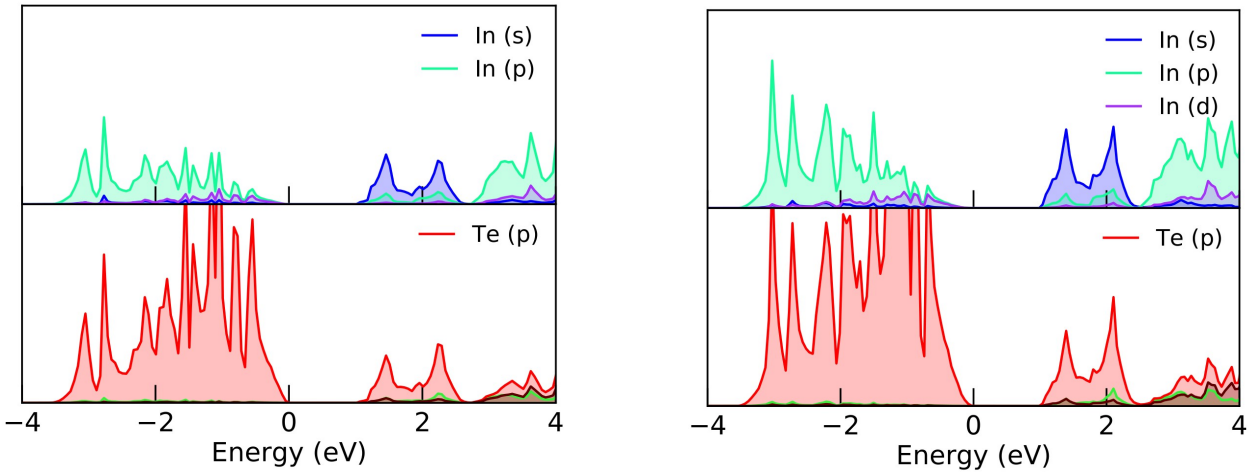

(a) $RbInTe_2$

(b) $CsInTe_2$

Figure H.4: DOS plots for the last part of the $I4/mcm$ structures

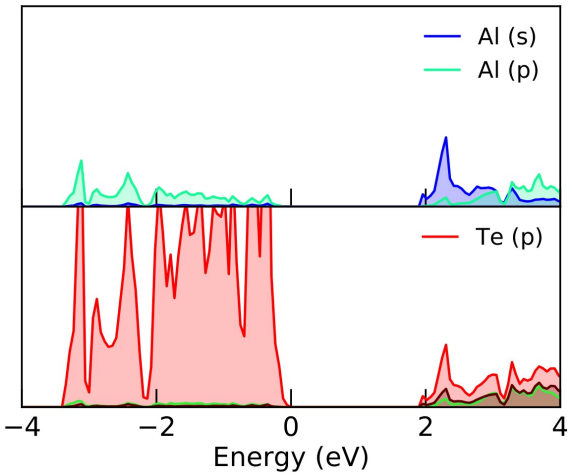

(a) $KAlTe_2$

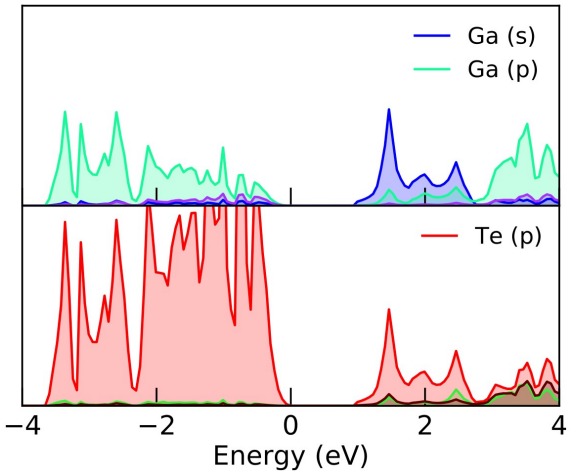

(b) $KGaTe_2$

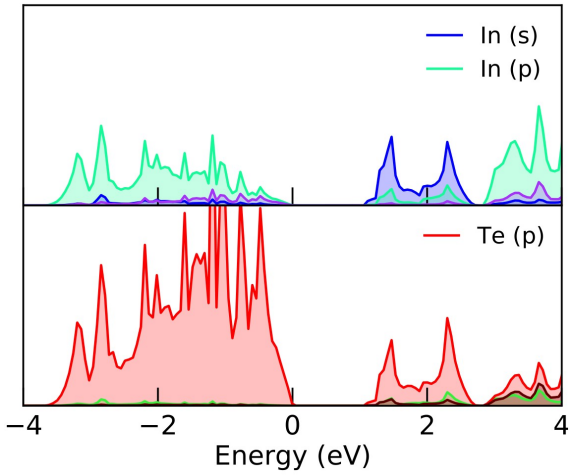

(c) $KInTe_2$

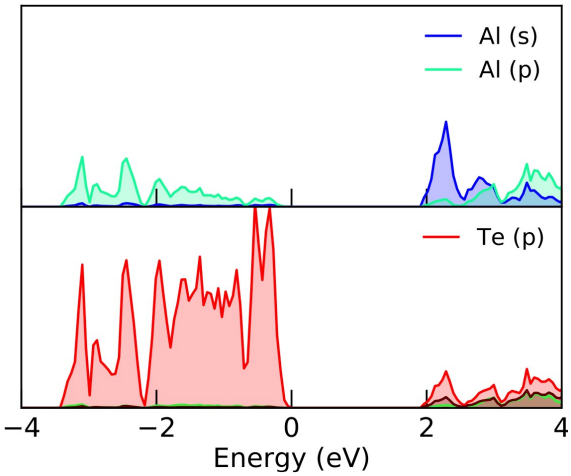

(d) $RbAlTe_2$

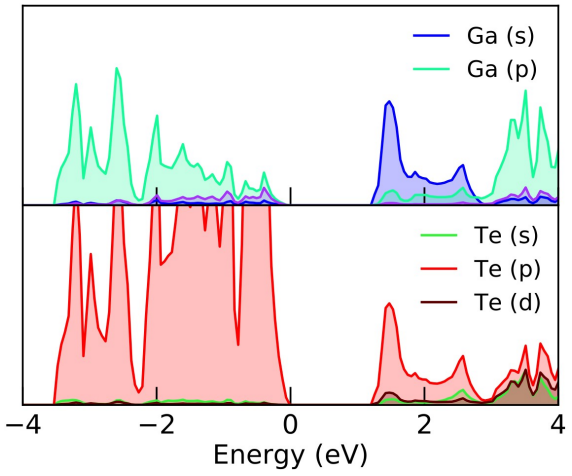

(e) $RbGaTe_2$

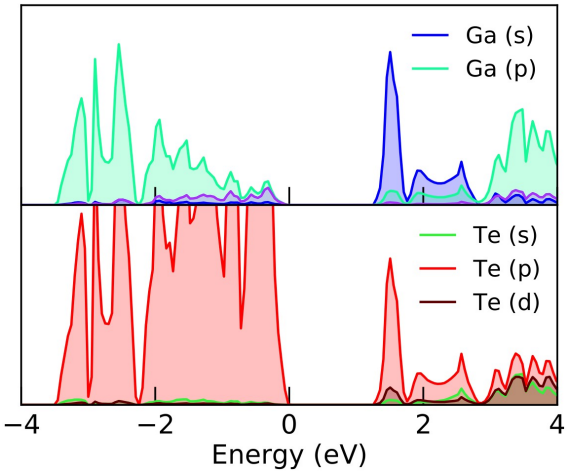

(f) $CsGaTe_2$

Figure H.5: DOS plots for the first of the $C2/c_8$ structures.

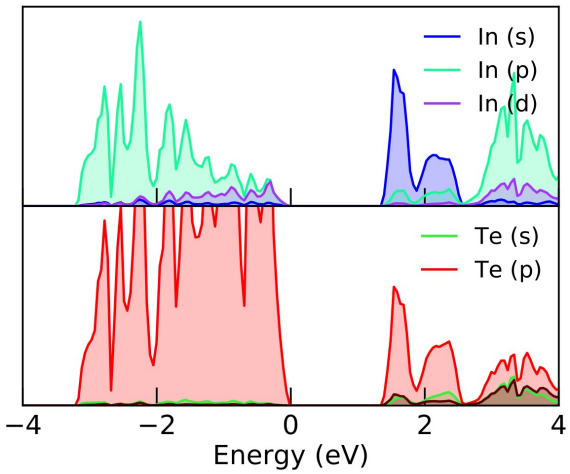

(a) $CsInTe_2$

Figure H.6: DOS plots for the last part of the $C2/c_8$ structures

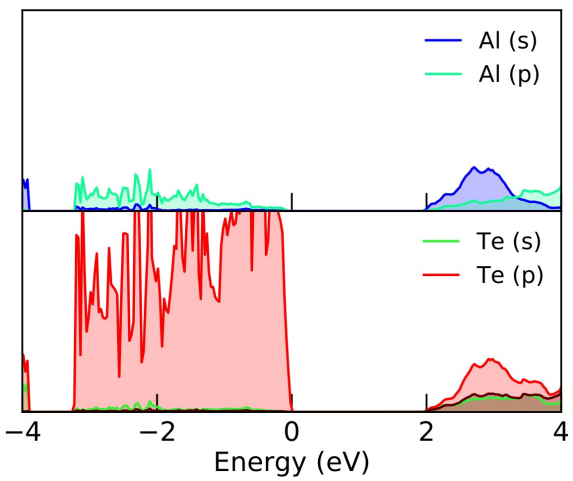

(a) $KAlTe_2$

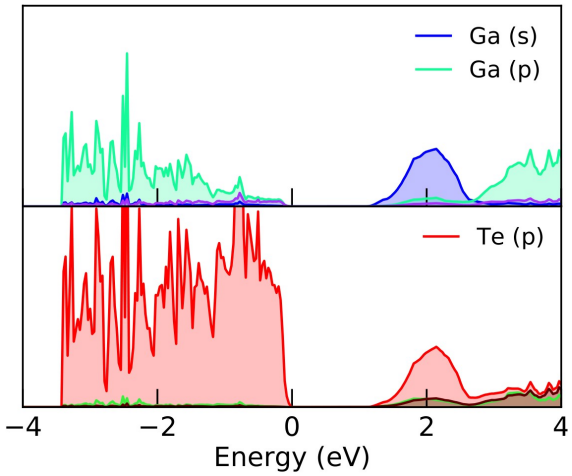

(b) $KGaTe_2$

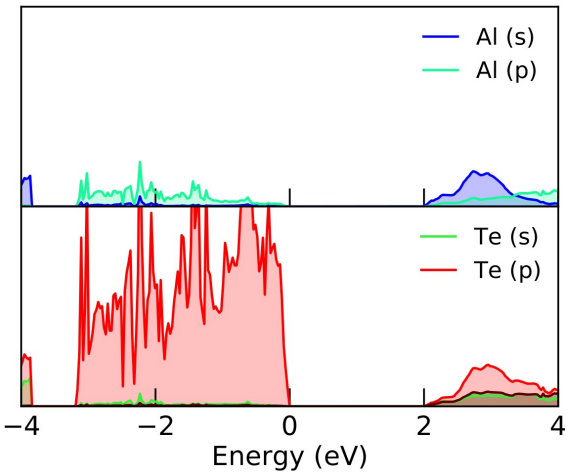

(c) $RbAlTe_2$

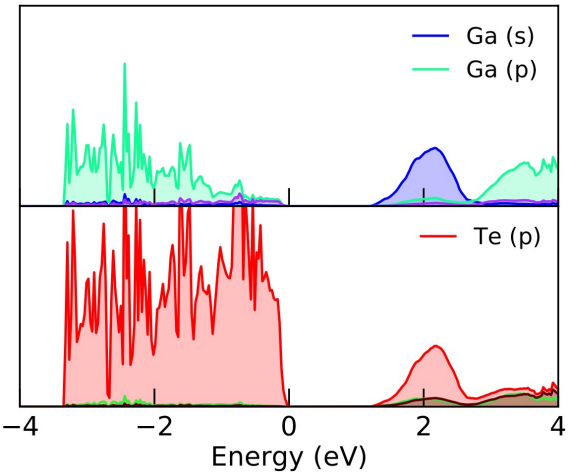

(d) $RbGaTe_2$

Figure H.7: DOS plots for the first of the $C2/c_{32}$ structures.

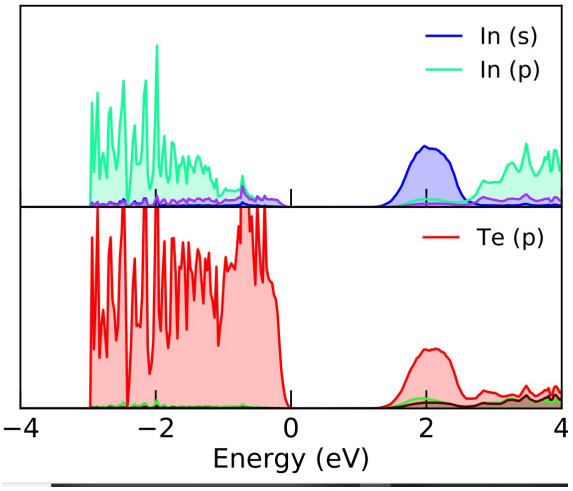

(a) $RbInTe_2$

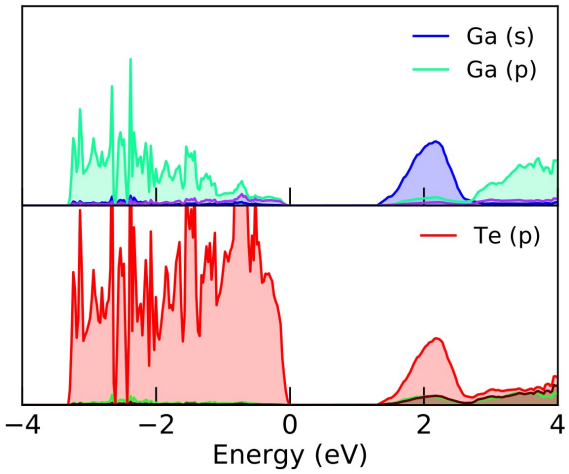

(b) $CsGaTe_2$

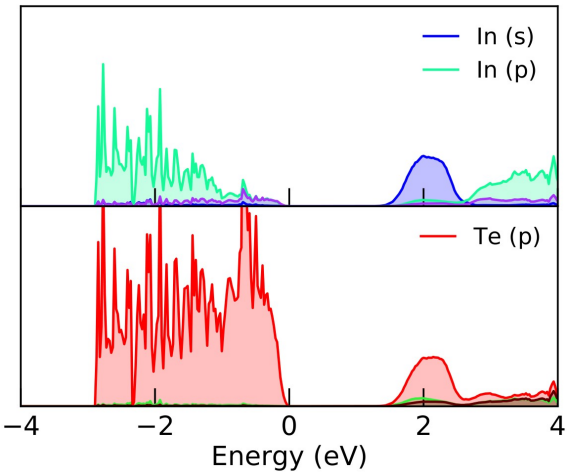

(c) $CsInTe_2$

Figure H.8: DOS plots for the last part of the $C2/c_{32}$ structures

I Additional numerical values

Numerical values, such as lattice parameters and band gap values for all compounds are presented in Table I.1

Table I.1: Numerical values for the lattice parameters a, b and c and band gaps.The lattice parameters are in the unit [Å] and band gaps in [eV]. The direct band gaps are only given for the soc-calculations and if the fundamental band gap is indirect.

System	Structure	a	b	c	Non-soc band gap	Soc band gap	Direct band gap
$LiAlTe_2$	$Pna2_1$	7.12	7.44	8.93	2.27	2.033	2.256
$LiAlTe_2$	$I\bar{4}2d$	7.40	7.40	7.40	2.23	2.01	
$LiGaTe_2$	$I\bar{4}2d$	7.39	7.39	7.39	1.673	1.411	1.485
$LiGaTe_2$	$Pna2_1$	7.12	7.44	8.91	1.601	1.354	1.467
$LiInTe_2$	$Pna2_1$	7.39	7.80	9.07	1.496	1.219	
$LiInTe_2$	$I\bar{4}2d$	6.44	6.44	12.60	1.456	1.201	
$NaAlTe_2$	$I4/mcm$	6.56	6.56	6.56	1.204	1.109	1.229
$KAlTe_2$	$C2/c_{32}$	8.32	8.32	16.50	1.958	1.916	
$KAlTe_2$	$C2/c_8$	7.18	7.18	6.67	2.119	1.913	2.229
$KAlTe_2$	$I4/mcm$	6.94	6.94	6.94	1.621	1.48	1.701
$KGaTe_2$	$C2/c_8$	7.02	7.02	6.83	1.094	0.87	1.454
$KGaTe_2$	$I4/mcm$	6.91	6.91	6.91	0.552	0.436	0.787
$KGaTe_2$	$C2/c_{32}$	8.31	8.31	16.61	1.216	1.097	
$KInTe_2$	$C2/c_8$	7.07	7.07	7.29	0.92	0.968	1.134
$KInTe_2$	$I4/mcm$	7.07	7.07	7.07	0.93	0.808	1.139
$RbAlTe_2$	$C2/c_{32}$	8.36	8.36	17.13	1.976	1.936	
$RbAlTe_2$	$C2/c_8$	7.45	7.45	6.52	2.096	2.079	2.292
$RbAlTe_2$	$I4/mcm$	7.08	7.08	7.08	1.73	1.485	1.854
$RbGaTe_2$	$C2/c_{32}$	8.34	8.34	17.19	1.296	1.183	
$RbGaTe_2$	$C2/c_8$	7.31	7.31	6.74	1.395	1.183	1.645
$RbGaTe_2$	$I4/mcm$	7.07	7.07	7.07	0.72	0.478	1.001
$RbInTe_2$	$C2/c_{32}$	8.72	8.72	17.40	1.34	1.134	
$RbInTe_2$	$I4/mcm$	7.22	7.22	7.22	1.044	0.83	1.297
$CsGaTe_2$	$C2/c_8$	7.61	7.61	6.67	1.501	1.301	1.629
$CsGaTe_2$	$C2/c_{32}$	8.37	8.37	17.89	1.413	1.267	
$CsInTe_2$	$C2/c_{32}$	8.75	8.75	18.10	1.427	1.213	
$CsInTe_2$	$C2/c_8$	7.63	7.63	7.04	1.585	1.352	1.565
$CsInTe_2$	$I4/mcm$	7.40	7.40	7.40	1.106	0.828	1.430

Ivar Loland Råheim

Computational Materials Design of Materials for CO_2 Conversion using Sunlight

NTNU
Norwegian University of
Science and Technology